Structural, optical and electrical properties of copper and silver-copper iodide thin films

Osama Madkhali

THÈSE

Présentée et soutenue publiquement le 8 décembre 2021
pour l'obtention du titre de

DOCTEUR de L'UNIVERSITÉ DE LORRAINE
Spécialité : Sciences des matériaux

Par

Osama Abdullah MADKHALI

Structural, optical and electrical properties of copper and silver-copper iodide thin films

Composition du jury :

Antoine BARNABÉ	Rapporteur	Professeur, CIRIMAT, Toulouse
Sandrine PERRUCHAS	Rapporteur	Chargée de Recherche HDR, IMN, Nantes
Sidi OULD SAAD HAMADY	Examinateur	Professeur, LMOPS, Metz
Aline ROUGIER	Présidente de jury	Directrice de Recherche, ICMCB, Bordeaux
Jean-François PIERSON	Directeur de thèse	Professeur, IJL, Nancy
Maud JULLIEN	Co-directrice de thèse	Ingénieure de Recherche, IJL, Nancy

Institut Jean Lamour, UMR 7198, ARTEM - CS 50840-54011 Nancy Cedex

Université de Lorraine – Ecole doctorale : Chimie, Mécanique, Matériaux, Physique (C2MP)

Acknowledgments

My first recognition, genuine admiration, and gratitude go to my supervisor Jean-François Pierson. Your full implication in my work, including the patience, patience, and patience you showed in providing guidance, in addition to your trust in the last couple of years, has been amazing. My appreciation also includes the confidence that you allowed growing in me during my research and writing, as well as the liberty you allowed me in moving forwards with my thesis was instrumental in improving my confidence and self-esteem. I was also impressed by the genuine care you have for all your students, with you taking the time to enquire after my family, my daughters. Most important was your decision to work with me during my confidence and, in the process, spend some time with my family. The support was extraordinary.

My gratitude and appreciation also go to my co-supervisor Maud Jullien, whose help with the thesis made me realize the objectives and outcomes I had set forth at the beginning of the thesis.

Also, in my appreciation is the members of the jury for their agreement to participate in the thesis. The truth is that without the participation of this group of the jury, I may not have realized the expected outcomes for the thesis.

I would like to greatly thank Prof. Herve Rinnert, the leader of nanomaterials for optics team at IJL, for his agreement to use his lab facilities for the photoluminescence measurements. Also, special thanks to Alaaeldin Giba, for his great help during the thesis and in particular with the optical measurements and discussion.

Also, special thanks are for Abdelkrim Redjaimia, who provided me with a brainstorming session in discussions about microstructure results. The session was critical in my research as it provides

an in-depth understanding of the results and the eventual presentation of the outcomes in my article.

I wish to thank the members of the CC-Microscopies, especially Jaafar Ghanbaja, for your permanent desire to help, Sandrine Mathieu for the training in SEM, Sylvie Migot and Hiba Kabbara for their TEM lamella preparation; the contribution was vital for my work.

I would like to thanks the PVD team, and I hope that I will not forget any one of them in my appreciation. The first, is, Fahad Alnjiman, David Pilloud, Silvère, Fabien Capon, David, Benjamin, Claudia De Melo Sanchez, Alejandro Borroto, Alexis Garcia Wong, Agathe Virfeu, Zil, Christophe Celindano, Joseph Antoine, Nicole, Daria, Christy Fadel, Aurelien Didelot. Thanks also to the lab for giving me the access to use so much equipment

A very special thanks to Fahad, Hiba, Turki, Mahmoud, Soufiane, Ziad, Dorra, Omar, Firas, Mohsen, Hamad and all my friends from Saudi Arabia, Gulf countries and here in Nancy.

Appreciation also goes to the Saudi Arabia Embassy in France and Jazan University for offering me the PhD grant.

My gratitude also to my father, for a lot for support and help, also my brother Omar and all of my family members.

My final appreciation goes to my wife for sharing and supporting all the moments of study. The part of my heart Dalia and Dareen these years you have been my partner, my force, and one of the reasons that I want to be a better person.

I dedicated this achievement to my deceased mother.

Contents

General introduction **1**
Chapter 1 Introduction to copper halides properties and their applications **5**
1.1 Introduction 8
1.1.1 The challenges of p-type transparent conductive materials 8
1.1.2 Applications in solar cells and light emitting diodes. 10
1.2 Wide bandgap semiconductor (WBG) 13
1.3 Copper halide compounds 14
1.4 Copper iodide 16
1.4.1 Survey on CuI 16
1.4.2 Crystal structure and phase transition 17
1.4.3 Band structure and optical properties 19
1.4.4 On the electrical properties of CuI and their alloys 23
1.4.5 CuI applications in thermo/optoelectronic devices 26
1.5 Silver iodide 29
1.5.1 Crystal structure and phase transition 29
1.5.2 Band structure and optical properties 31
1.6 Ternary silver copper iodide (Ag,Cu)I 33
1.7 Deposition techniques 35
1.7.1 Spin-coating 35
1.7.2 Spray coating, and inkjet printing methods 36
1.7.3 PLD method 36
1.7.4 Vapor iodination method 37
1.7.5 Solid iodination method 37
1.7.6 Vacuum thermal evaporation method 37
1.7.7 Reactive sputtering method 38
1.8 Conclusion 38
References 40
Chapter 2 Synthesis of copper iodide thin films and characterizing techniques **49**
2.1 Introduction 52
2.2 Metallic thin film growth and elaboration setup 52
2.3 Vapor iodination 54
2.4 Characterization methods 56
2.4.1 X-ray diffraction (XRD) 56
2.4.2 Scanning electron microscopy (SEM) 58
2.4.3 Electron probe microanalysis (EPMA) 60

2.4.4 Transmission electron microscopy (TEM) 61
2.5 Four-point probe method 65
2.6 Hall Effect Measurements 66
2.7 UV-visible spectroscopy 68
2.8 Photoluminescence 71
2.9 Conclusion 72
References 73
Chapter 3 Blue emission and twins structure of p-type copper iodide thin films 75
3.1 Introduction 79
3.2 About the growth conditions 80
3.3 Influence of the amount of iodine on the structure and the properties of CuI thin films 81
3.3.1 Structure and composition of CuI films 81
3.3.2 Microstructure of γ-CuI thin films 83
3.3.3 Optical transmission and absorption 89
3.3.4 Electrical properties 91
3.3.5 Photoluminescence 94
3.4 Conclusion 97
References 98
Chapter 4 Tuning the photoluminescence response and control of the electrical carrier type of (Ag, Cu)I thin films 102
4.1 Introduction 106
4.2 Composition and (micro)structural characterizations 108
4.2.1 Film composition and structure 108
4.2.2 Film morphology 114
4.2.3 Photoluminescence (PL) 117
4.2.4 Optical properties of (Ag,Cu)I films 121
4.2.5 Electrical properties of (Ag,Cu)I thin films 123
4.3 Conclusion 129
References 131
General conclusion 135
Perspective 137
Appendix A 139
Appendix B 144
Appendix C 147
Appendix D 148

General introduction

Transparent conductive materials (TCM) attract great interest thanks to their excellent optoelectronic properties, which adapt for several daily life applications. Development of light emitting devices and solar cells is the most remarkable progress using TCM. Thus, many studies have been devoted either to improve the existing well-known TCM's performance or to discover new alternatives.

Most studies in the development of the TCM have been mainly focused on metal oxide thin films, such as Al-doped ZnO (AZO) and ln_2O_3:Sn, that show efficient n-type characteristic at room temperature. On the other side, the research on TCM with p-type property is still under progress. In this direction, copper iodide (CuI) is one of the most promising candidates thanks to its high transparency and intrinsic p-type conductivity. This allows the use of CuI in different fields, such as photovoltaic and UV optoelectronic applications. In particular, it shows great interest as p-type transparent electrode in organic solar cells and micro-scale transparent flexible thermogenerators, [1,2].

Among the same family of metal halide, silver iodide (AgI) exhibits similar electronic and band structures with CuI but with intrinsic n-type conductivity. This encourages the approaches of the construction of transparent p–n heterojunction diodes from both compounds [3].

In addition, based on the above information, a ternary compound of (Ag,Cu)I is deserved to be explored. Thus, Annadi et al recently reported on the optical and electronic properties of the (Ag,Cu)I system [4]. They have shown that the type of the charge carrier conductivity in the ternary compound can be manipulated between p-type and n-type based on the Ag/Cu ratio. Nevertheless, the correlation between the optical, in particular the photoluminescence, and the electrical results

has not been established. Hence, this work is dedicated to deep study the microstructure of the binary and the ternary above systems. In addition, we focus on link between the PL and electrical responses from the grown thin films. A clear correlation between the obtained electrical behaviour and photoluminescence response has been established. The role of the point defects, Cu-vacancies and I-vacancies, in both the electrical and PL responses is discussed in details. In addition, the crossover of the carrier type from p to n is interpreted in the light of the role of defect chemistry.

This manuscript is organized as follows:

Chapter 1 *is mainly dedicated to a brief introduction on the physical and structural properties of the copper and silver halides and their applications. Their crystal structure, phase transition, band structure, optical and electrical properties are described. In addition, the reported synthesis methods have also been highlighted.*

Chapter 2 *is concerned with describing in details the main experimental methods used to characterize the prepared samples. The technical and fundamental aspects of magnetron sputtering and the related characterization techniques of the thin films are presented. The main principles of operation of the scanning and transmission electron microscopes are stated. The Hall Effect and photoluminescence experiments used for the electrical and optical characterizations, respectively, are also discussed in details.*

Chapter 3 *is devoted to present the result and discussion of the prepared CuI thin films. Such films have been prepared by iodination of sputtered copper thin films. The effect of the stoichiometric ratio between Cu and I on the crystal phase and film structure has been studied. Details about the local microstructure via high-resolution transmission electron microscopy (HR-TEM) are investigated. In addition, the electrical and optical properties of the prepared thin films at different iodine amount are discussed in details.*

Chapter 4 *is focused on the first results of (Ag,Cu)I thin films prepared by iodination of co-sputtered Ag-Cu layers. The crystalline structure of the prepared films was investigated by X-ray diffraction (XRD). The electrical properties of (Ag,Cu)I films were characterized by Hall effect measurements and revealed a p-type and n-type carrier behaviour for films. A correlation between the optical and electrical results was established and evidenced the origin of the electrical behaviour.*

The main findings of the thesis are presented with general conclusions and perspective. It worth to mention that the results chapters 3rd and 4th have been presented in an article format.

References

[1] C. Yang, M. Kneiβ, M. Lorenz, M. Grundmann, Room-temperature synthesized copper iodide thin film as degenerate p-type transparent conductor with a boosted figure of merit, Proc. Natl. Acad. Sci. U. S. A. 113 (2016) 12929–12933. https://doi.org/10.1073/pnas.1613643113.

[2] C. Yang, D. Souchay, M. Kneiß, M. Bogner, H.M. Wei, M. Lorenz, O. Oeckler, G. Benstetter, Y.Q. Fu, M. Grundmann, Transparent flexible thermoelectric material based on non-toxic earth-abundant p-type copper iodide thin film, Nat. Commun. 8 (2017). https://doi.org/10.1038/ncomms16076.

[3] J.-H. Cha, D.-Y. Jung, Air-Stable Transparent Silver Iodide–Copper Iodide Heterojunction Diode, ACS Appl. Mater. Interfaces. 9 (2017) 43807–43813. https://doi.org/10.1021/acsami.7b14378.

[4] A. Annadi, H. Gong, Success in both p-type and n-type of a novel transparent AgCuI alloy semiconductor system for homojunction devices, Appl. Mater. Today. 20 (2020) 100703. https://doi.org/10.1016/j.apmt.2020.100703.

Chapter 1
Introduction to copper halides properties and their applications

Graphical Abstract

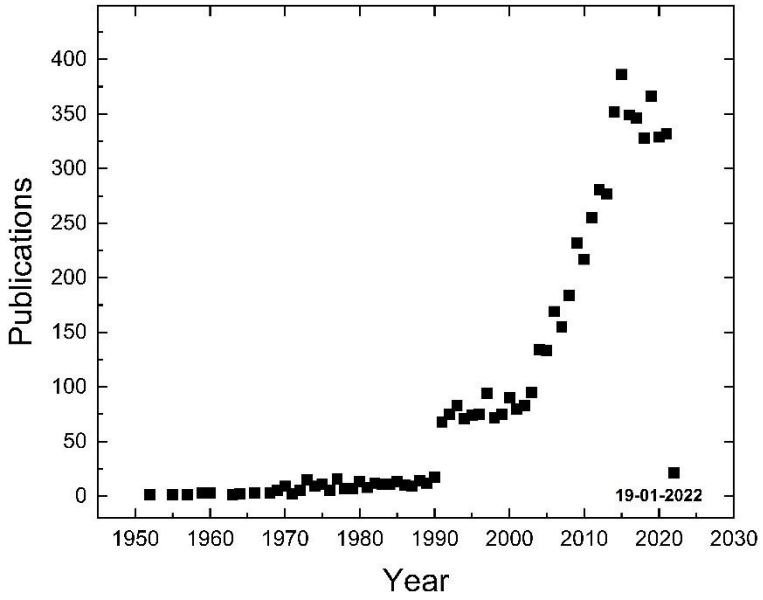

The number of physics and material science publications with the written words "copper iodide," in the title.

Contents

1.1 Introduction .....
1.2 Wide bandgap semiconductor (WBG) .....
1.3 Copper halide compounds .....
1.4 Copper iodide .....
1.4.1 Survey on CuI .....
1.4.2 Crystal structure and phase transition .....
1.4.3 Band structure and optical properties .....
1.4.4 On the electrical properties of CuI and their alloys .....
1.4.5 CuI applications in thermo/optoelectronic devices .....
1.5 Silver iodide .....
1.5.1 Crystal structure and phase transition .....
1.5.2 Band structure and optical properties .....
1.6 Ternary silver copper iodide (Ag,Cu)I .....
1.7 Deposition techniques .....
1.7.1 Spin-coating .....
1.7.2 Spray coating, and inkjet printing methods .....
1.7.3 PLD method .....
1.7.4 Vapor iodination method .....
1.7.5 Solid iodination method .....
1.7.6 Vacuum thermal evaporation method .....
1.7.7 Reactive sputtering method .....
1.8 Conclusion .....

1.1 Introduction

Most of the metal oxides-based materials display efficient n-type conductivity at room temperature. This is the reason behind the intensive research and development on transparent p-type semiconductors and conductors in academic and industry sectors. Copper iodide (CuI) is among the most intriguing p-type material candidates due to the wide conductivity range allowing his use in optoelectronics devices as transparent electrodes and semiconducting layers [1]. In addition, CuI thin films, with high optical transparency in the visible light range, can be obtained by using different low-temperature (ranging between RT and 75 °C) deposition processes [2–4]. This is an additional advantage from elaboration point of view. Thus, in this chapter, we give an overview on structural and physical properties of copper halides, with focusing on CuI, and compare it to the commercially used wide bandgap semiconductors. We discuss the electronic structure, point defects, and doping character in CuI crystals. Moreover, we highlight a summary on the recent developments in CuI-based devices with examples of some applications. Finally, we report current challenges and potential prospects.

This chapter will also give information about the synthesis, the structure and the properties of silver iodide. Although this material is depicted as a n-type material, it is useful to describe its properties. Indeed, heterojunctions based on CuI / AgI bilayers have been described in the literature [5]. Finally, the last section of this chapter is devoted to the elaboration and characterization of ternary materials ((Ag,Cu)I).

1.1.1 The challenges of p-type transparent conductive materials

Over the last several decades, inorganic metal oxide transparent semiconductors and conductors showed very rapid and significant progress in optoelectronic research. They have been employed

for countless applications using charge transport layers in semiconductors for transparent electrodes in various optoelectronic devices [6–9]. Even if it is used as a backplane transistor in organic light emitting diode displays (OLED), such inorganic transparent semiconductors exhibit ionic bonding properties with high optical band gaps (e.g. > 3.1 eV) and good electronic transport. In addition, the intrinsic donor defects (i.e. oxygen vacancies) have low formation energy and shallow doping characteristics, providing solid and sustainable n-type conductivity while preserving optical transparency in visible light [1]. On the other hand, in the p-type of such metal oxides, the valence band maximum (VBM) for hole transport is mainly composed by anisotropic oxygen 2p orbitals. This makes the introduction of shallow acceptors problematic task owing to the high electronegativity of the small size of oxygen atoms [1]. Therefore, the VBM is intensely confined, leading to reduced hole concentrations, large hole effective mass, and limited hole mobility. This is the reason behind the lake of high-performance p-type metal oxides. Nevertheless, there is some attempt to find promising candidates for p-type semiconductors such as NiO, SnO, Cu_2O despite their insufficient limited mobility (1.07, 18 and 100 cm^2/Vs, respectively [10,11]), hole transport, and poor optical transparency [12–14]. Alternatively, multi-layered oxychalcogenides materials have been recently identified as potential new p-type semiconductors. But, the low stability of oxychalcogenides compared to metal oxides is also a challenge [15].

On the other hand, transparent copper(I) halides, for instance CuI, show large band gap of 3.1 eV and high hole mobility (up to 44 $cm^2\ V^{-1}\ s^{-1}$) with p-type conductivity reaches 280 S cm^{-1}thanks to its broad range of hole concentrations (10^{16} to 10^{20} cm^3) [2,16]. These high electrical performances of CuI, compared to its oxide counterpart (Cu_2O), can be attributed to two reasons:

1. The lower electronegativity of iodine than oxygen (2.66 vs. 3.44 on the Pauling scale), allowing more delocalized holes just above VBM [3].
2. The large radius of iodine ions of 220 pm significantly overlaps with the three outermost p-orbitals that may cause the rapid hole transport [1].

Thanks to the abovementioned properties, copper iodide is often used in heterojunction diodes, thermoelectric devices, photodetectors, and as transparent conductive electrode and hole-transport layers in photovoltaic devices and transistors [2,17–25].

1.1.2 Applications in solar cells and light emitting diodes.

As the world's population is growing, the consumption of the energy increases. Most of this energy comes from the fossil fuels (petroleum, coal or natural gas) that have a dramatic impact on the global warming due to the emission of CO_2. Thus, there is a continuous and growing interest to find other different and environment-friendly energy resources. The solar energy is one of the most cleanly and renewable alternative. Every year, the National Renewable Energy Laboratory (NREL) releases the top research cell efficiencies charts, which indicate the evolution of the five main categories Figure1.1. Solar cells are photovoltaic devices able to convert sunlight into electricity. The principle of a photovoltaic apparatus is to capture the sunlight, to generate electron-hole pairs, and inject them into two electrodes. Negative electrode is to transfer the electrons and the positive one to transfer the holes and therefore generating the electric power. The typical used and adapted stack for useful solar cell is p-n junction of semiconductors.

The combination of a p-type semiconductor (containing mainly holes as carriers) with a n-type one (containing mainly electrons as carriers) in a closed-circuit, results in a gradient generated electric field and a depletion region at the interface layer. Hence, the absorbed sunlight excites the

electrons to the conduction band and the separation between the electrons and holes occurs owing an electric field.

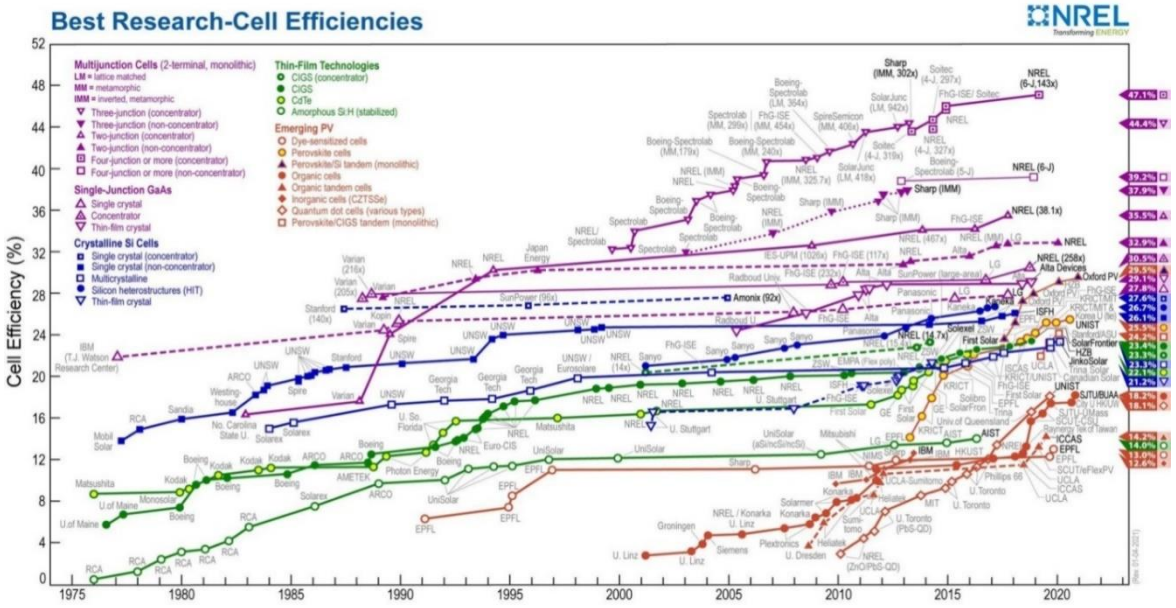

Figure 1.1: National Renewable Energy Laboratory graph of solar cell efficiency over the years [26] .

Si-based solar cells are still the most popular choice thanks to a strong Si-technology academic research and industrial development. However, the small and indirect bandgap (around 1.1 eV) of silicon limits the absorption from the sunlight spectrum to a narrow range of wavelengths in IR (wavelength lower than approx. 1100 nm) [27]. In addition, its indirect bandgap property is a real obstacle for achieving high efficient Si-based solar cells. A significant part of the solar spectrum in UV-visible is not efficiently used and is thermally dissipated as shown in Figure1.2. This raises worldwide interest to exploit the intense part of the sunlight spectrum in the UV-visible range. In this respect, the use of wide bandgap (WBG) semiconductor materials for photovoltaic purposes attracts the attention [28]. The direct WBG semiconductors can absorb the UV-visible photons

with high efficiency. Since there is no material able to absorb the whole sunlight spectrum, high efficiency solar cells are made of 2 or 3 devices (multijunctions).

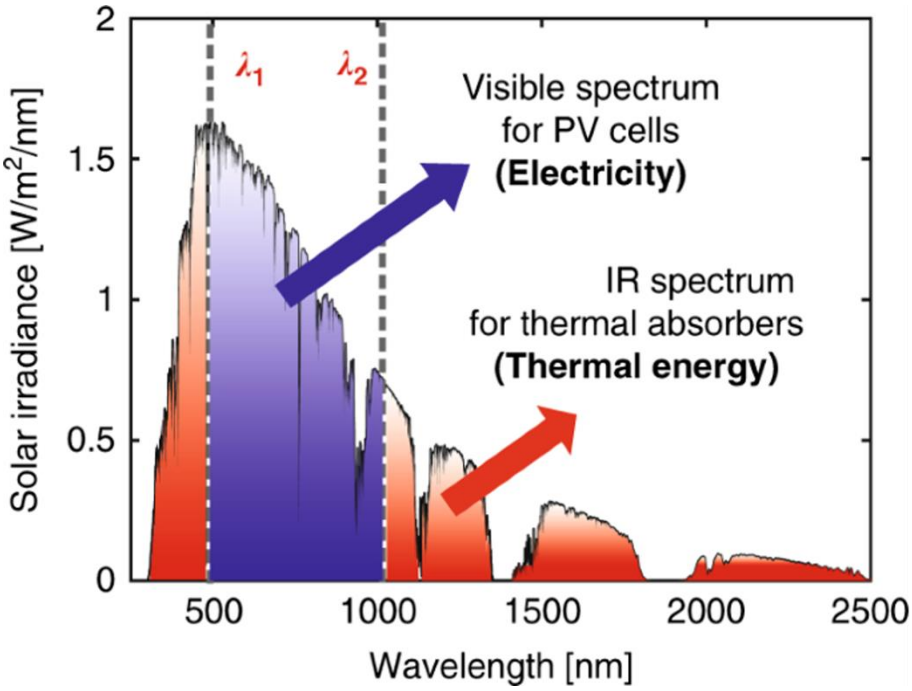

Figure 1.2: Most of the solar radiation reaches Earth is visible light (400-700nm) and infrared spectra(700-2500nm). Only a small amount of ultraviolet (300-400nm) radiation reaches the surface. respectively 44%, 52%, and 4% of solar energy adapted from [29] .

Reducing the consumption of the electricity, used in lighting and displaying systems, is also an additional method to maximize the benefit from the gained energy originated either from the fossil fuel or solar sources. Thus, light-emitting diodes (LEDs) have driven the progress in this area due to their low-cost, low-energy required to operate and their increasingly ubiquitous presence throughout modern society. Most of home lighting now incorporates LED technology. For these purposes, white emission colour is needed, knowing that blue is the main colour in the composition of white emission. , the WBG semiconductor, as UV and blue emitter, books its place in lightening

technology. Hence, the research on optical properties of WBG semiconductors is of great importance in multidiscipline purposes from lightening to harvest energy applications.

1.2 Wide bandgap semiconductor (WBG)

From the abovementioned information, one can realize how the WBG semiconductor development is decisive in current technology like LEDs and solar cells [30]. Therefore, it seems crucial to run accurate studies on electronic and optical properties of these materials. Most of the current researches are focus on III-nitride and II-VI materials due to their interesting properties for several applications. Among them, GaN and ZnO based systems are the most intensively studied due to their direct and wide bandgap with high exciton binding energy, see Table1.1. Optical properties can be controlled by different doping regimes [31]. These characterizations make them ideal candidates for optoelectronic applications.

Table 1.1: Comparison of some basic properties of ZnO, GaN [16,32–34]

Properties	ZnO	GaN
Optical band gap (eV)	3.44	3.50
Exciton binding energy (meV)	63.1	26
Lattice constant (nm)	0.3249	0.319
Mismatch to Si (%)	15	17
Structure types	Hexagonal wurtzite	Hexagonal wurtzite
Melting point (°C)	1975	>2500
Boiling point (°C)	2360	N/A

However, the most critical difficulty in such materials is their large lattice mismatch with the available and commercial substrates. Large lattice mismatch induces a significant number of structural defects challenging the epitaxial growth approaches and affecting optoelectronic performances of final devices. This brings to search other alternatives systems to overcome such issues. The properties of copper halide compounds make them excellent candidates. In the following section, we discuss the properties of copper halide compounds with a focus on copper iodide system.

1.3 Copper halide compounds

Copper halides compounds, particularly CuCl, CuBr, and CuI, exhibit particular interest thanks to their competitive properties compared to III-nitrides and II-VI compounds [35]. The main notable characteristic are large direct bandgaps(3.3 eV for CuCl, 2.91 eV for CuBr and 2.95 eV-3.1 eV for CuI), large temperature dependence, high ionicity [36], and large exciton binding energies (190 meV for CuCl, 108 meV for CuBr and 63meV for CuI) [16,36–50] with their lattice constants closely matched with Si one (Table1.2). Atoms forms tetrahedral coordinated isomorphic structure with the diamond-type lattice. At room temperature, cuprous halides have a zinc blende structure composed of two interpenetrating fcc lattices displaced along a body diagonal. Cu atoms form one of the fcc lattice, while halogen atoms form the other one. It is worth to mention that, this structure shows good lattice mismatch with Si substrate, Figure1.3.

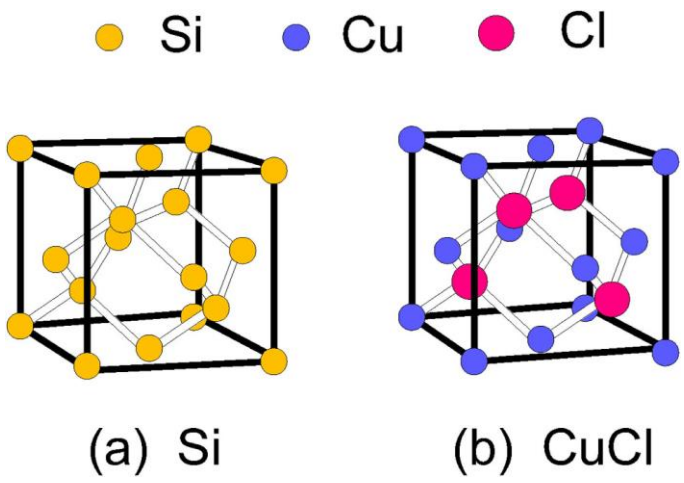

Figure 1.3:(a) Four covalently bonded Si atoms define the diamond-crystal fcc lattice. (b) Zincblende fcc lattice of cuprous halides crystal (CuCl, CuBr, and CuI) are made of two interpenetrating fcc lattices segregated by a body diagonal. [51].

Table 1.2: Comparison of some basic properties of CuCl, CuBr and CuI [16,37,51,52]

Properties	CuCl	CuBr	CuI
Optical band gap (eV)	3.3	2.91	2.95-3.1
Exciton binding energy (meV)	190	108	63
Lattice constant (nm)	0.542	0.569	0.6054
Mismatch to Si (%)	< 0.5	4.7	11.4
Structure	cubic F-43m ZB	cubic F-43m ZB	cubic F-43m ZB
Melting point (°C)	426	492	606
Boiling point (°C)	1490	1345	1290

The lattice constant of Si is 0.5431 nm while that of CuCl, CuBr and CuI is 0.5424, 0.5695 and 0.6054 nm, respectively. These close lattice constants with Si substrate is of great importance for crystal growth. It makes copper chloride and bromide well adapted for Si based technology. Although the lattice mismatch of CuI with Si is approx. 11.4 %, this value is still lower than that reported for GaN and ZnO. For instant, the large lattice mismatch between commercial III-V semiconductors and substrates, typically, sapphire or SiC, leads to the generation of high density of misfit dislocations. In addition, zinc blende structure (ZB) reveals low value of piezoelectric stress coefficient, compared to the wurtzite crystal structure, needed to reduce the built-in electrostatic field inside the crystal. The large built-in electrostatic field could have a bad impact on the optical performances of the devices. Moreover, copper halides show high exciton binding energy of 63 meV, which is promising for high quantum efficiency devices [51].Moreover, it is intrinsically p-type materials owing to the domination of Cu-vacancies at excess of halogen conditions.

As an example, for copper halides compounds, we give particular interest to CuI, the subject of this thesis, in the following sections.

1.4 Copper iodide

1.4.1 Survey on CuI

Solid cuprous iodide (copper(I) iodide) has been studied continuously over the last three decades, with steadily increasing and recently significantly increased interest, Figure 1.4.

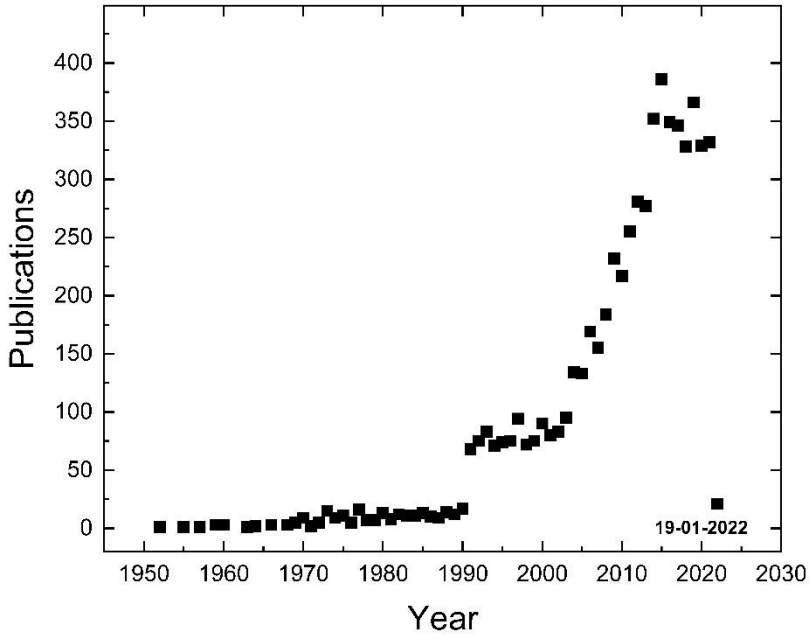

Figure 1.4: Number of publications in physics and material science media containing "copper iodide" in the title. Data from Web of Science

1.4.2 Crystal structure and phase transition

At atmospheric pressure, the crystal structure of CuI is characterized by three well-defined phases (α, β and γ) that can be obtained depending on the growth temperature [16,53,54]. These different CuI phases are shown in the corresponding phase diagram, Figure1.5. These three α, β and γ phases crystallize in rocksalt, wurtzite, and zinc blende-like structures at temperatures higher than 400 °C, between 370 and 400 °C and lower than 370 °C, respectively, Figure1.6. The low-temperature γ-phase has a zinc blende-type structure with space group ($F\bar{4}3m$). In the high-temperature rocksalt-type α-phase (space group $Fm\bar{3}m$) [55], the copper ions are randomly distributed over all octahedral sites. An intermediate β-phase (space group $P\bar{3}m1$) [56], exists between the γ-phase and α-phase [55].

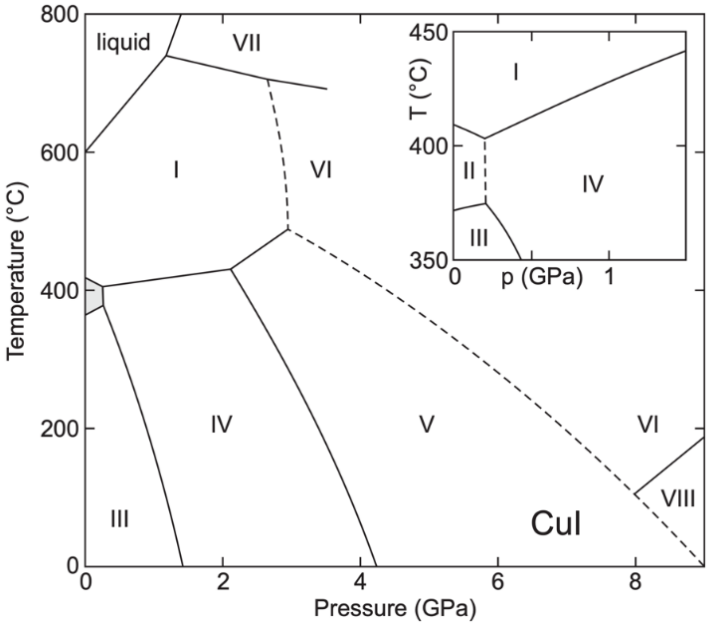

Figure 1.5: Phase diagram of CuI.I, VIII: rocksalt (cubic, Fm3m), grayed area represents phase II: wurtzite (hexagonal, $P6_3mc$), III: zincblende (cubic,F43m), IV: rhombohedral, V: tetragonal (P4/mmm), VI: cubic, adapted from [16].

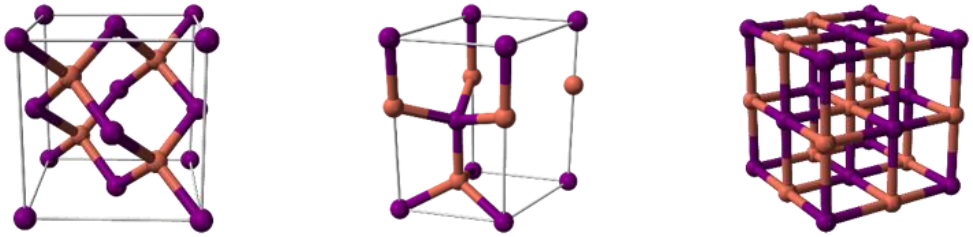

Figure 1.6: Copper-iodide crystal structures [57].

CuI crystalizes in a zincblende structure at both ambient temperature and pressure. At ambient temperature, with increasing the pressure (higher than 1.4 GPa), the zincblende phase transitions to an intermediate rhombohedral structure, and at 4 GPa, it changes its structure to a tetragonal

one (space group P4/mmm). CuI crystallographic parameters have been investigated in details and can be summarized in Table 1.3.

Table 1.3: The different structures of CuI at different temperatures; space group of γ-phase is F-43m, β-phase is P-3m1 and α-phase is Fm-3m

Phase	Temperature (°C)	Structure type	Lattice constant *a*, *c* (Å)
γ-phase	< 370	zinc blende	*a*=6.05377-6.10866
β-phase	370 – 400	wurtzite	*a*=4.29863-4.30571 *c*=7.168-7.186
α-phase	> 400 °C	rocksalt	*a*=6.13489-6.14506

1.4.3 Band structure and optical properties

The outer-shell electronic configuration of Cu atom is $3d^{10}\ 4s^{1}$and iodine atom is $5s^{2}\ 5p^{5}$. In compound form, the electron from the orbital s of the Cu atom is transferred to the halogen atom (higher electronegativity of iodine atoms). As a result, Cu atoms exhibit completely filled outer *d* shell, while the halogen atom behave like rare-gas configuration. Several authors using photoelectron spectroscopy have examined the band structure of CuI. They revealed that VBM is made from Cu 3d and I 5p hybridization orbitals while, the conduction band is derived from Cu 4s level. The fundamental bandgap is corresponding to the direct transition at Γ point, Figure 1.7a. In this specific case, the bandgap value is around 2.95-3.118 eV [16]. In addition, due to the spin-orbit interaction in CuI, the uppermost of valence band is splitted to heavy hole (hh) and light hole (lh) bands with spin-orbit splitting equal to 0.64 eV [16,58]. As a consequence, a doublet-term

Z1,2 can be observed at low temperature absorption measurement. This Z1,2 is referring to the band–band transitions of the two top valence bands, namely hh and lh bands [16,58].

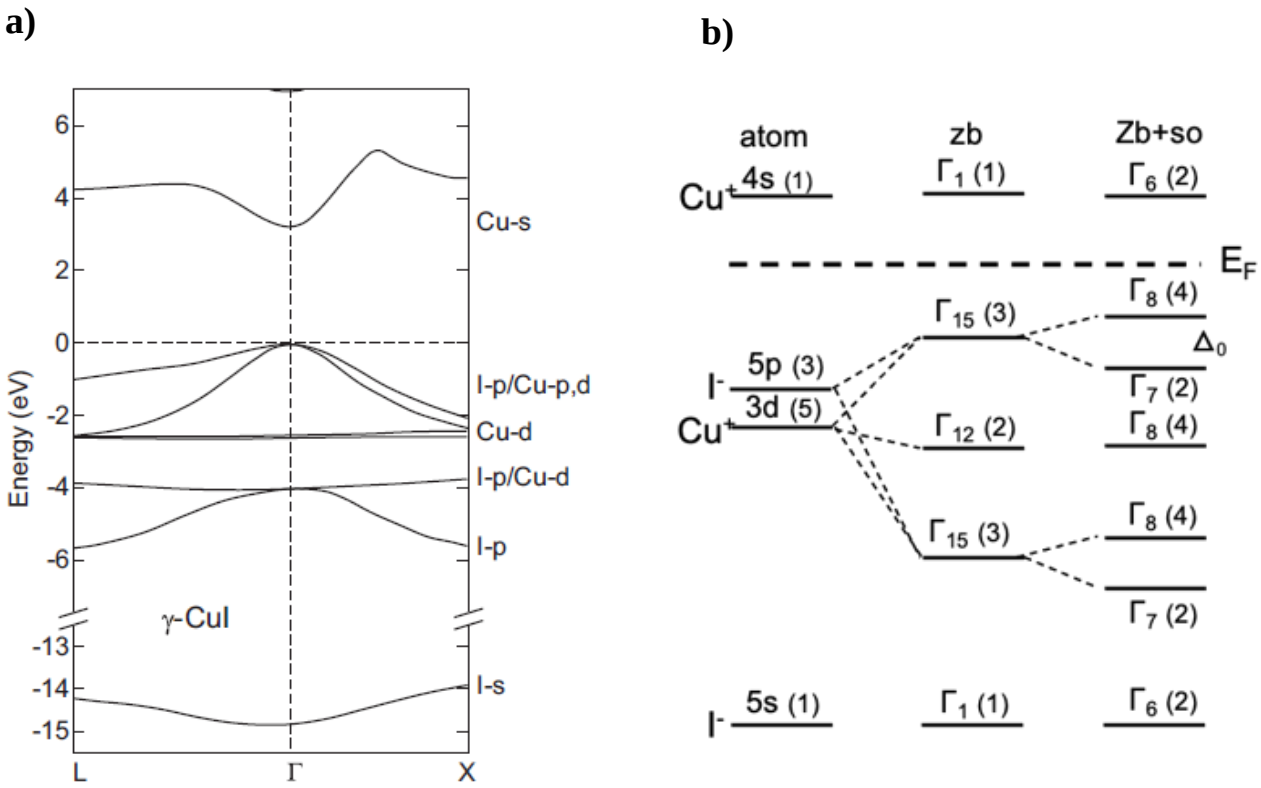

Figure 1.7: a) The electronic band structure of -CuI (calculated with GGA-PBE level) adapted from [59] b) Representation of the conduction and valence state in CuI due to s, p, and d electrons at the Γ-point in the cubic crystal field of the zinc blende structure "so" is referring to spin-orbit interaction. Numbers in brackets indicate the degeneracy state [60].

Schematic energy diagram of γ-CuI zinc blende structure and energy level splitting, due to the crystal field and split-orbit interactions, are depicted in Figure1.7b. A. Goldman explained that, in the valence band, Cu and I ions contribute with a filled $3d^{10}$ shell and a configuration of $(ns)^2(np)^6$ respectively [60]. Thanks to the very close energy values of the p and d levels, these atomic orbitals could strongly be hybridized. Under the effect of the crystal field in zinc blende structure, the 5 fold degenerate of the d level is splitted into Γ_{15} (3) and Γ_{12} (2), whereas the s and p levels

are converted to Γ_{15} (3) and Γ_1(1). Inclusion of the spin-orbit interaction would split the Γ_{15} (3) to Γ_7 (2) and Γ_8 (4) with split-orbit (0.64 eV), whereas the Γ_{12} (2) is becoming Γ_8 (4). The author also reported on the band structure of CuBr and CuCl and obtained the spin-orbit split values around 0.15 and 0.067 eV, which are much smaller than the value of CuI. In addition, the coupling between the lowest conduction band state Γ_6 with the uppermost valence band states Γ_8 and Γ_7 originates the edge excitons called $Z_{1,2}$ and Z_3. Hence, the excitonic transitions in CuI are dominated by a strong absorption at the band edge. The optical absorption of CuI measured at low temperature shows the fine structure of excitonic transitions Figure 1.9. The theoretical ratio of the doublet is 3:1 with respect to the oscillator strength of the heavy hole to light hole components. The third absorption peak Z_3 is attributed to the spin-orbit splitting occurring in the valence band.

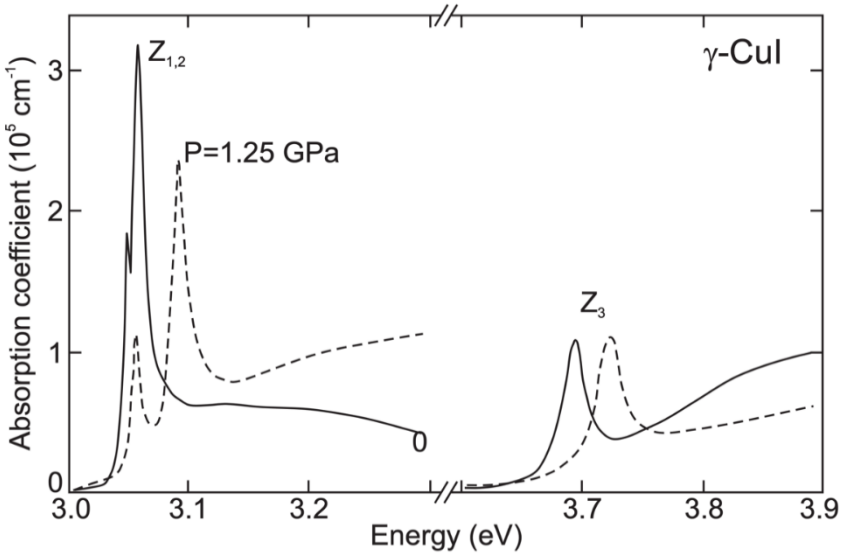

Figure 1.9: Absorption spectra of zinc blende CuI thin film at T=100K. The solid line denotes a sample with no external strain and dashed lines a sample stressed by an uniaxial strain along <111> of 1.25 GPa. [16].

In addition, the optical transitions related to defects play a major role in the electronic properties of CuI material [61]. It is well known that CuI behave intrinsically as p-type semiconductor and

its carriers properties is controlled via the intrinsic defect chemistry [37]. Jing Wang *et al.* [59] calculated the enthalpy of formation of CuI zincblende structure for two cases: a sample rich in copper and another one rich in iodine Figure1.10. They explained that CuI under equilibrium conditions has dominant acceptor defect close to the VBM in p-type material due to presence of many Cu vacancies [59]. The formation and ionization energies of Cu-vacancy are very low when the Fermi level is close to the VBM. In addition, the formation energy of the other native donor defects, that can compensate the Cu-vacancy defect, is significantly high. This is valid for both Cu and I rich samples. Hence, the origin of the p-type semiconductor is mainly driven by Cu vacancies, which form an acceptor level close to the valence band.

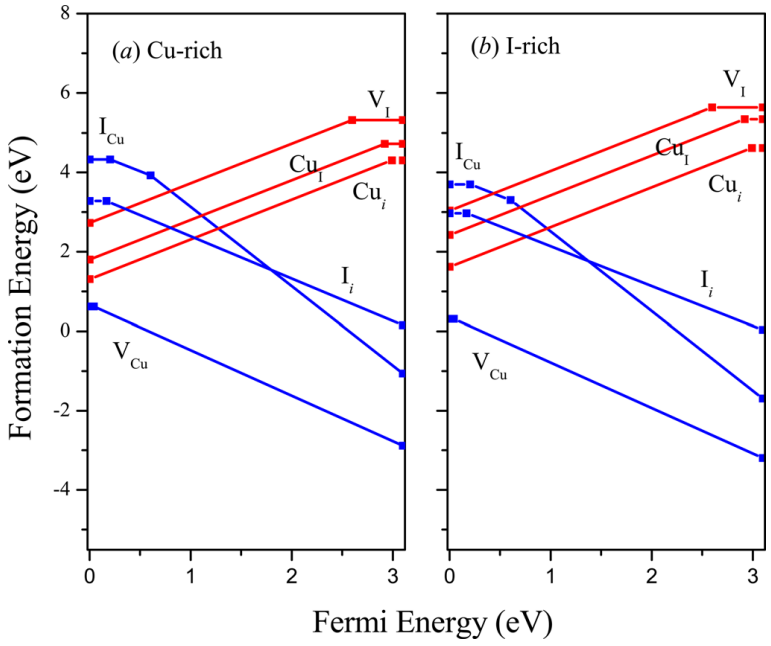

Figure 1.10: Native defect formation energies calculated for Cu/I-rich conditions [59].

On the other side, some of these intrinsic defects contribute to luminescent behavior of CuI. The radiative recombination in CuI crystals has been reported in different works [62–64]. The luminescence spectra of CuI at room temperature show two main photoluminescence (PL) bands

at approx. 410 nm and 700 nm, attributed to excitonic recombination and radiative point defects, respectively. However, at low temperature, the PL spectra is made up of several radiative transitions attributed to the impurities [65]. For instance, some phonon replica, close to the center Longitudinal Optical (LO) phonon, and some other lines belong to zero phonon were observed. In addition, electron–acceptor and donor–acceptor pairs (DAP) recombination have been identified. It is worth to note that luminescence properties of CuI can be tuned by controlling defects inside the prepared material. For instance, Guochen Lin *et al.* [66] investigated photoluminescence variations depending on the defect types by changing annealing conditions. PL measurements under different annealing conditions (in air, vacuum, and iodine vapor) enable the identification of the PL peaks position. They have observed three luminescence peaks, one attributed to the intrinsic exciton transitions and other two transitions originated from CBM to Cu-vacancy and from I-vacancy to the VBM Figure 1.11.

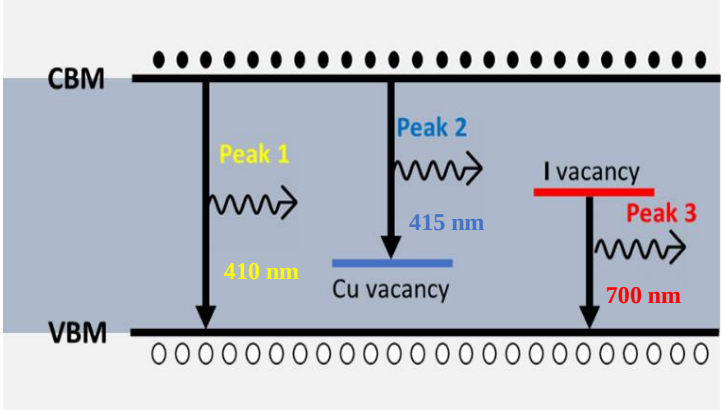

Figure 1.11:Origin of PL peaks in CuI thin films [66].

1.4.4 On the electrical properties of CuI and their alloys

It is well established that the optoelectronic properties of CuI thin films can be modified by the deposition technique used (Table 1.4). Sputtering and evaporation methods are favoured for

intensive manufacturing and scalability points of view. It also makes the increase of hole concentration and conductivity possible. In addition, CuI films conductivity increases between 156 to 283 S cm^{-1} when an I-rich environment was created during reactive sputtering [2]. Similar phenomena have been observed with solution-based technique and resulted in a conductivity increase of more than two orders of magnitude by directly adding iodine solution to the Cu precursor [67]. In the same way, several trails were reported to improve opto-electronic properties of CuI by doping or alloying the compounds. Yamada *et al.* [68] underlined a Br–alloying technique that involved thermally evaporating CuI and CuBr powders by varying Br ratios. They found that, CuBr films showed poor p-type semiconducting characteristics with low hole mobility of $0.15.10^{-3}$ cm^2 V^{-1} s^{-1} and the resistance was three orders of magnitude greater than CuI [69,70]. In addition, the CuBr V_{Cu} acceptor level is deeper in CuBr than CuI Figure 1.12.

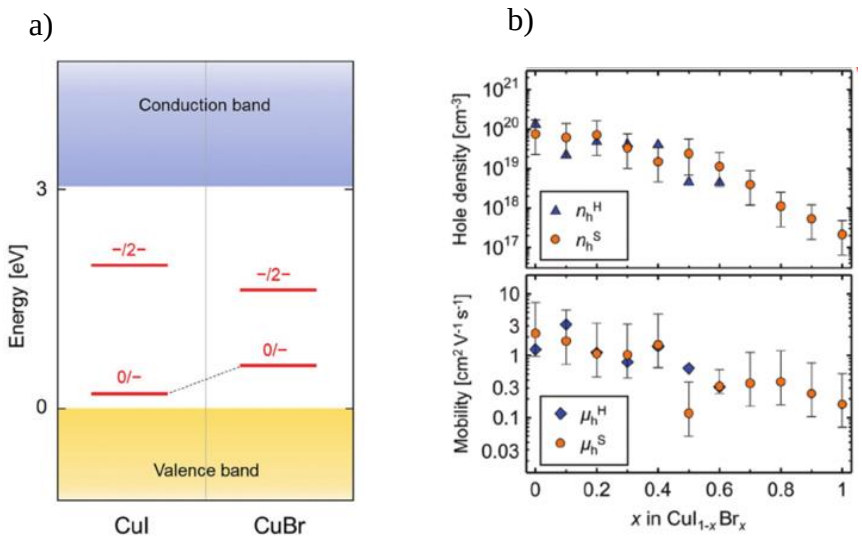

Figure 1.12: a) Charge states transition levels of V_{Cu} in CuI and CuBr . b) The hole concentrations and mobility of $CuI_{1-x}Br_x$ thin films determined by Hall-effect and Seebeck-effect measurements [68].

Hence, the addition of Br to CuI significantly lowered the hole concentrations from 10^{20} to 10^{17} cm^{-3}. Likewise, Br alloying had very little influence on transparency, and all alloys have

significant E_g (≥ 3.0 eV) values. On the contrary, recently, Annadi and Gong published another cation-alloying method utilising Ag^+ [71]. Ag_xCu_{1-x} metal films were deposited via radio frequency (RF) sputtering, and $Ag_xCu_{1-x}I$ thin films were formed under I_2 vapour. They observed that, pure CuI exhibits a high conductivity of 10.5 S cm^{-1}, hole density of 2×10^{19} cm^{-3}, and Hall mobility of 3.5 cm^2 V^{-1} s^{-1}. However, at 0.3 at. % Ag^+, the films showed lower conductivity of 2.6 S cm^{-1} and hole density of 2.2×10^{18} cm^{-3} but maximum mobility of 8.1 cm^2 V^{-1} s^{-1}, Figure 1.13. Additionally, when the alloys exhibit a Ag/Cu ratio exceeding 0.8, the samples show conductivity features with as a high electron mobility of 20.2 cm^2 V^{-1} s^{-1} and n-type conductivity of 0.01 S cm^{-1}. They also showed by Hall measurements, supported by ultraviolet photoelectron spectroscopy, that when Ag^+ fraction increases the Fermi level steadily switches from the VBM to the CBM. The band gap of alloys containing silver was lowered from 3.02 (CuI) to 2.78 eV (AgI). Regarding all these previous works, the study of electronic transport improvement for silver alloying could be extremely interesting. Thus, the next section is dedicated to the description of the structure, electronic structure and the properties of CuI thin films.

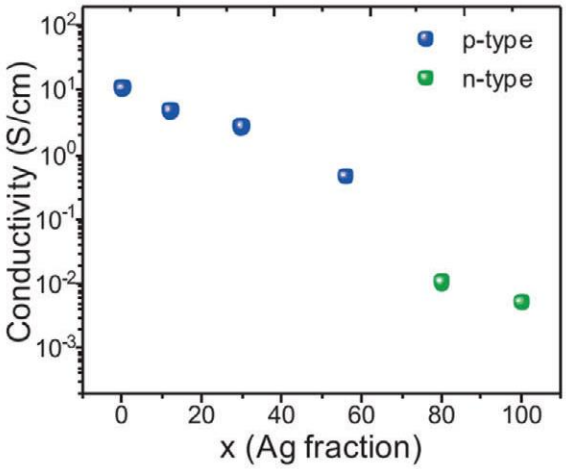

Figure 1.13 Conductivity variations for $Ag_xCu_{1-x}I$ alloys as a function of Ag content adapted from [71].

1.4.5 CuI applications in thermo/optoelectronic devices

Based on the above information on basic optoelectronic properties, CuI material has been studied for several applications which are briefly highlighted below. γ-CuI has emerged as ***a transparent p-type conductor***. It shows considerable conductivity value with significant transparency in visible range. Yang *et al.* [2] reported on the relation between conductivity and visible absorption coefficient in order to determine the figure of merit FOM = $\sigma/\alpha = -1/[R_s \ln (T_{vis} + R)]$, where R_s is the sheet resistance (Ω/sq) given by $1/\sigma t$, t is the film thickness. Due to the absence of R values in the majority of studies, the FOM is usually simplified by using the approximation $R = 0$ and the formula FOM can be simplified into $-1/ (R_s \ln T_{vis})$. To quantify the efficiency of the deposited CuI films, the Figure 1.14 shows that the CuI had a much higher FOM (1.3×10^6 $M\Omega^{-1}$) than the previously reported p-type TCs and even close to the standard ITO (4×10^6 $M\Omega^{-1}$) [72]. These results confirmed the high transparent conductor character of CuI making it a well-established transparent conductor in several applications.

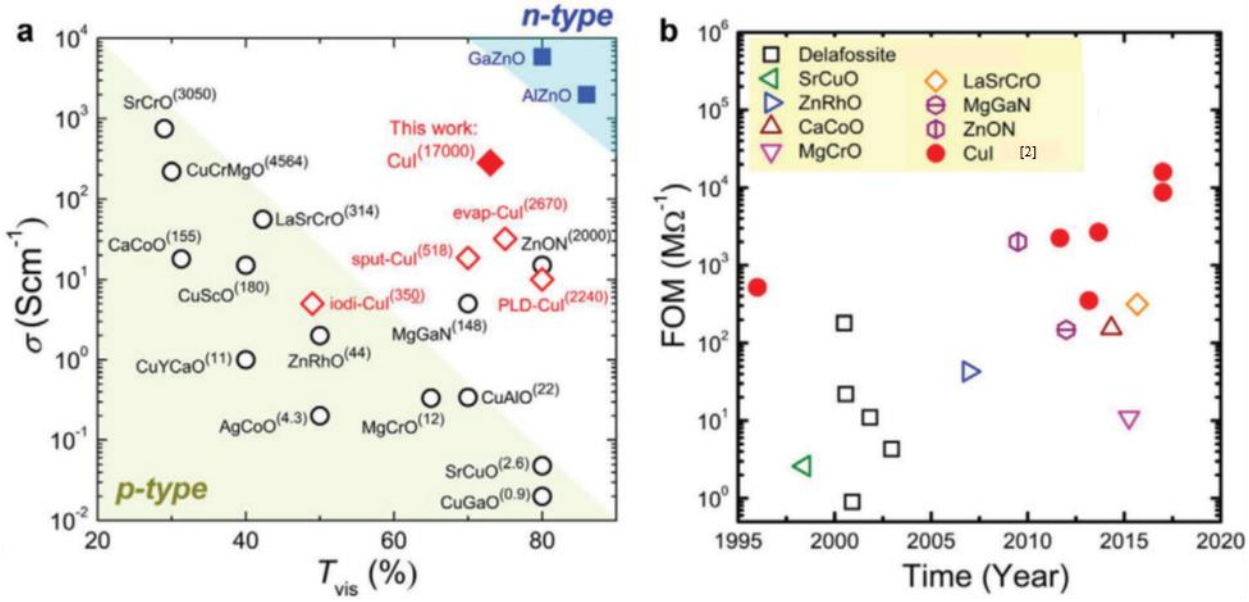

Figure 1.14: a) Electrical conductivity and averaged visible transmittances for CuI and other n- and p-type TCs. b) Comparison of FOM over time for the reported p-type TCs [2].

On the other side, intensive **thermoelectric properties** investigations have made significant progress in energy conversion applications by discovering several novel materials [73]. It is well known that, for high thermoelectric efficiency, electrical, thermal or optical parameters have to be compromised. Seeking for large-area manufacturing, tremendous initiatives have been devoted to creating novel thermoelectric materials using affordable and earth-abundant components. In this direction, CuI is considered among the most attractive transparent materials that exhibited promising thermoelectric performance. It is predicted to show low thermal conductivity and a substantial Seebeck coefficient of 237 μV K^{-1} owing to the presence of the heavy iodine atoms and the significant phonon scattering [74]. For instant, Yang *et al.* [24] who grew 300 nm CuI thin films by reactive sputtering at RT, demonstrated a substantial thermoelectric figure of merit of ZT = 0.21 at 300 K. It should be noted that the high ZT value is 1000 times greater than p-type TCOs and 100 times higher than n-type TCOs like (Al:ZnO [75], In:SnO_2 [76],La:$SrTiO_3$ [77]).

In optoelectronic applications, p–n junction is a key element of optoelectronic devices. CuI thin films showed good compatibility with n-type metal oxide/halide semiconductors such as ZnO, $BaSnO_3$, a-IGZO, AgI, and NiI_2 in the fabrication of transparent p–n hetero/homojunctions diodes [5,17,25,78–81]. For example, Chang Yang *et al.* [78] created a p-CuI/n-ZnO epitaxial thin-film junction with good device performance properties. In addition, Yamada *et al.* [82] have found the photovoltaic effect in a CuI/IGZO heterojunction when it was exposed to UV light. This sparked the interest in using it as a fast-response self-powered UV photodetector [83–85]. Moreover, CuI has previously been reported in extremely efficient blue and UV LEDs and is predicted to substitute GaN in the future due to its exciton binding energy of 58 meV [37,86,87]. Very recently, it is proposed to use a unique structure of n-GaN/p-CuI blue LED using epitaxial p-CuI as hole injection layer [37].

In the field of photovoltaic, CuI has been involved in different solar cell types seeking for increasing the final power conversion efficiency (PCE) and the reliability [88]. For instance, CuI has been reported as a substitute organic hole transport layer (HTL) in the organic or perovskite solar cells. Thanks to the high hole conductivity of CuI and its better band alignment with the perovskite material, the PCE of the solar cell can be improved from 11.1% to 14.6%. It is worth to mention that many of Cu-based HTLs layer has been developed to improve solar cell electrical characteristics. Figure 1.15 summarizes the electrical characteristics of solar cells using different Cu-based HTLs layer. It can be also noticed that, with regard of the deposition method, CuI-based HTL cells can exhibit considerable good electrical characteristic and compete with the other kind of Cu-based HTL cells.

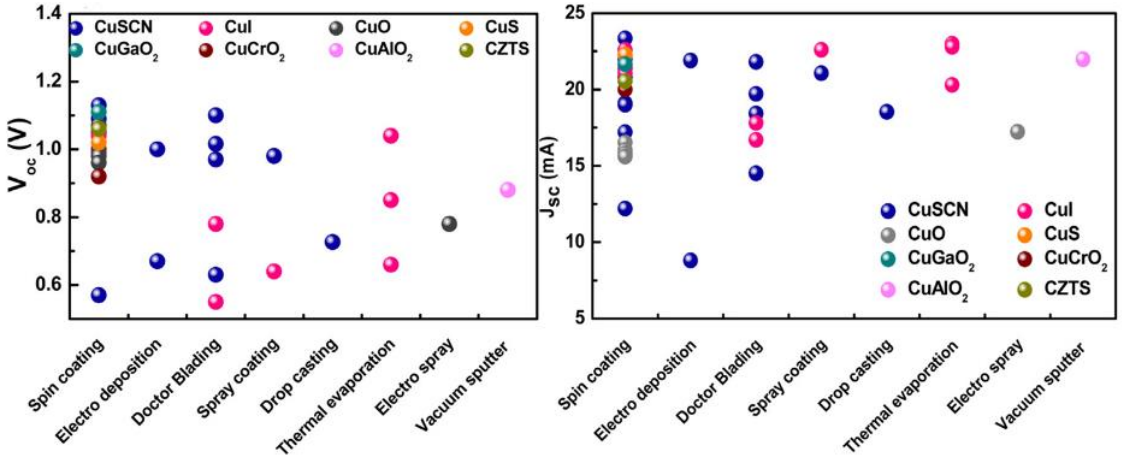

Figure 1.15: Open-circuit voltage and photocurrent density for solar cells with various inorganic Cu-based HTL layers deposited using different methods [89].

1.5 Silver iodide

1.5.1 Crystal structure and phase transition

The pressure-temperature phase diagram of AgI shows that this material exhibits a mixture of wurtzite and zincblende structure at ambient pressure Figure 1.16. The rocksalt structure has been found stable at high pressure. These are different than the other silver halides AgBr and AgCl which are crystallizing in rocksalt structure under normal conditions. Hence, the main differences between AgI and its counterparts (AgBr and AgCl) is the inversion of symmetry in their rocksalt structure [90]. However, the AgI phase changes over wide range of pressure to wurtzite, zincblende, and KOH structures as stated in Table 1.4.

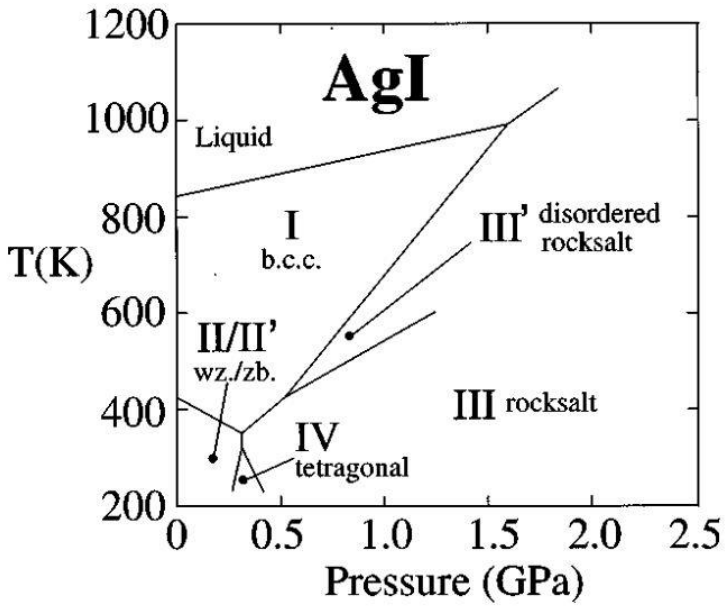

Figure 1.16: Phase diagram of AgI in the low pressure region at point of the (P, T) adapted from [90].

Table 1.4: Summary of AgI structure in the 0 – 14.5 GPa pressure range . Phases II, II', III, and V adopt the wurtzite, zincblende, rocksalt, and KOH structures, respectively, adapted from [90].

Pressure		Lattice parameters			
p (GPa)	Phase	a (Å)	b (Å)	c (Å)	β (°)
0.0	II′	6.4991(7)	$=a$	$=a$	90
0.0	II	4.599(3)	$=a$	7.524(5)	$\gamma=120$
1.5	III	6.0339(2)	$=a$	$=a$	90
3.4	III	5.9577(3)	$=a$	$=a$	90
6.4	III	5.8570(3)	$=a$	$=a$	90
8.9	III	5.7894(3)	$=a$	$=a$	90
11.1	III	5.7320(4)	$=a$	$=a$	90
11.3	V	4.056(1)	4.057(2)	5.615(3)	98.43(4)
11.7	V	4.052(1)	4.052(1)	5.604(3)	98.70(4)
14.3	V	4.007(2)	4.064(2)	5.546(6)	100.39(8)
14.5	V	4.001(1)	4.067(1)	5.545(5)	100.55(8)

In terms of temperature, and at atmospheric pressure, three phases (α, β and γ, also called I, II and II' in Figure 1.16, respectively) have been reported [90,91] The α-phase has a body-centred cubic arrangement of I^- ions with highly mobile Ag^+ ions randomly distributed through the equivalent interstices. The superionic conductor α-phase formed at higher temperature than 420 K transforms into the semiconductor β-phase (wurtzite-like, hexagonal structure) at lower temperature than 420 K. At temperature lower than 408 K, β-phase transforms mostly into γ-phase (zincblende-like, cubic structure) with small amount of β-phase. This reflects the complexity of the phase transitions in small range of temperature.

1.5.2 Band structure and optical properties

Similarly, to copper halides, the unique electronic structure of silver halides is due to very strong hybridization of *d* orbitals of silver with *p* orbitals of halogens in the valence orbit. Electronic configuration of AgI in ground state is Ag: Kr $4d^{10}5s^1$ and I: Kr $4d^{10}5s^25p^5$. As an example, we present the band structure of γ-AgI phase in Figure. 1.17. It shows that the energy band of AgI can be divided into three main groups [92]. Firstly, the lowest bands located in the valence region around -12 to -13 eV and originated from the 5s states of I. Secondly, the valence band maximum (VBM) which is formed from strong hybridization of 4d states of Ag and 5p states of I. Thirdly, the conduction band minimum (CBM) is originated from the s states of Ag overlapped with weak contribution from p and d orbitals of I. As for CuI, AgI is a direct semiconductor with a band gap of 2.26 eV, DFT-GGA methodology [92].

From electronic point of view, it can be noticed in Figure 1.18, that the γ-AgI phase exhibits similar absorption features, when measured at low temperature, as the absorption features of γ-CuI phase measured at room temperature.

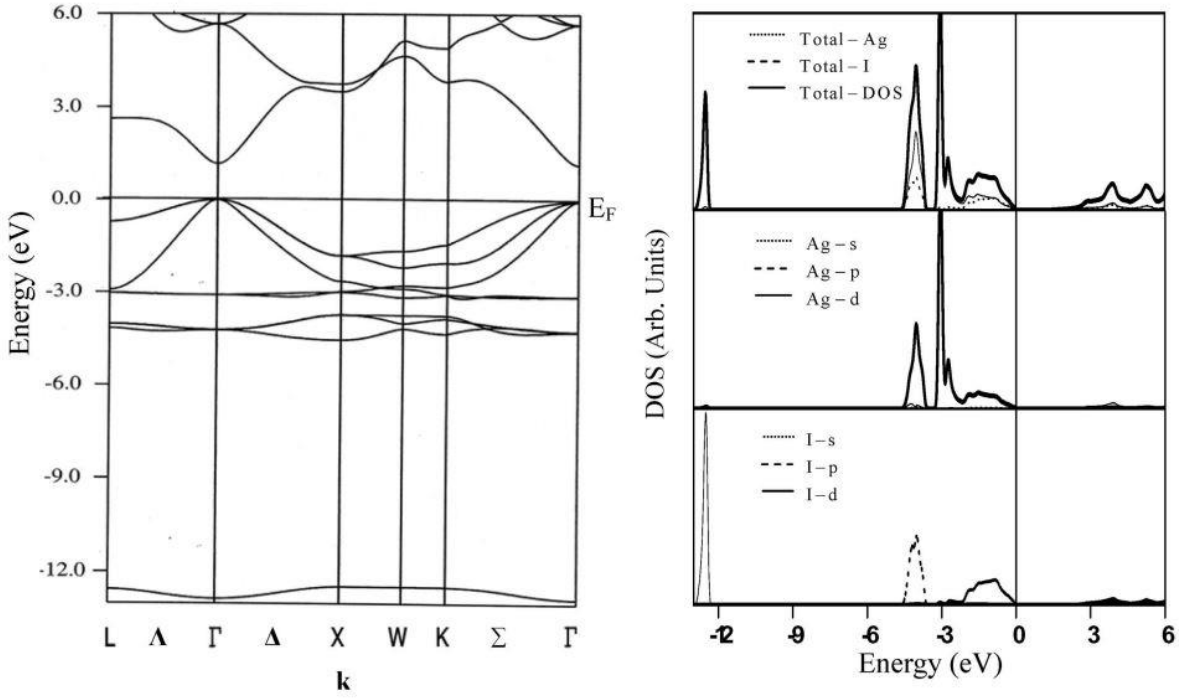

Figure 1.17: Band structure and density of states of γ-AgI along high symmetry directions of the first Brillouin zone adapted from [92].

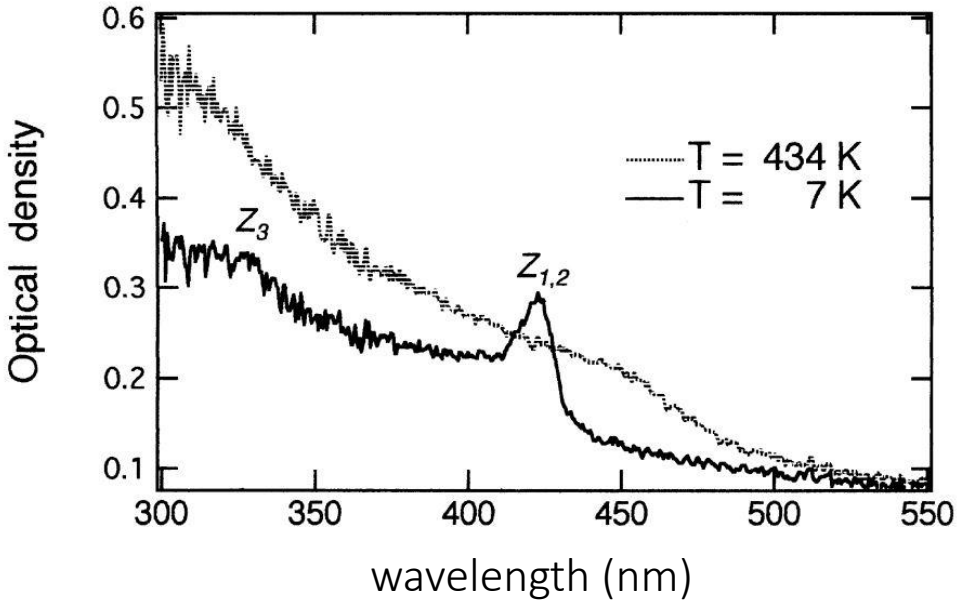

Figure 1.18: Temperature dependence of the optical density spectrum of AgI film, which was in the gamma phase prior to measurements adapted from [93].

Shosuke Mochizuki *et al.* [93] reported on the absorption properties of γ-AgI at low and high temperature. They have shown that the absorption spectrum at 7 K Figure 1.18 is consisted of doubled term Z1,2 and Z3, which is similar to what is found in the case of γ-CuI phase at room temperature, as discussed above in section (1.4.3). However, in the case of γ-AgI, the Z1,2 exciton absorption band appeared at about 2.936 eV (422 nm), while Z3 exciton one appeared faintly at about 3.777 eV (328 nm), respectively with energy difference about 0.841 eV. On the other hand, when the temperature increased, the excitonic sharp peak Z1,2 shifted to longer wavelength and became weak and broader. This weakness in the excitonic absorption could be the reason behind the very weak luminescence of AgI at higher temperature, e.g. room temperature [93,94].

AgI films drew our attention because they play a key role in some application such as energy transmission through hollow fibres reported in this paper [95] described the development of plastic waveguides for infrared energy transmission, particularly CO_2 laser radiation transmission (λ=10.6 μm).

1.6 Ternary silver copper iodide (Ag,Cu)I

CuI and AgI, two parent metal halides, have demonstrated various application potentials. It also shows promise for thin film transistors and photodiodes. Even though Cu and Ag are in the same group, we propose and study the characteristics of a (Ag,Cu)I system. Due to their intrinsic electronic, optical, and chemical characteristics, ternary for semiconductor materials could be a potential approach to tune and control electrical properties as well as optical band gap. So far, the research on structural phase development and superionic conduction in (Ag,Cu)I has mostly focused on these ternary [71,96].

Annadi *et al.* [71] successfully developed a series of ternary $Ag_xCu_{1-x}I$ (x =0, 0.12, 0.30, 0.56, 0.80 thin films using a two-step co-sputtering and iodination technique. They succeeded to develop a (Ag,Cu)I semiconductor system that is possibly p-type or n-type depending on Ag concentration. They also investigated the electrical and optical characteristics of thin films made of (Ag,Cu)I. In addition, the light emitting properties and tunable electronic bands with desired electrical conductivity have been achieved.

In different study, Mohan *et al.* [96] reported on the preparation of Ag-rich $Ag_{1-x}Cu_xI$, (x = 0.05, 0.10, 0.15, and 0.25) and Cu-rich $Cu_{1-y}Ag_yI$, (y = 0.05, 0.10, 0.15, and 0.25) solid solutions. They have produced as nanoparticles by a soft mechanochemical reaction. In their study, at x = 0.25 ($Ag_{0.75}Cu_{0.25}I$), a monophasic solid solution with zincblende structure (a = 0.637 nm) with crystallite size of around ~31 nm was achieved. They found that, according to Vegard's law, the lattice parameter decreases gradually from 0.649 to 0.604 nm with increasing Cu (doping element) concentration, which indicating the development of static cation disorder in the AgI–CuI system. Also, a diode type I–V characteristic has been demonstrated and attributed to possible interfacial microscopic p–n junctions formed by the a soft mechanochemical reaction process.

In the same line, Johan *et al.* [97] reported on the electrical conductivity and phase transition behavior in nanoscale AgI_x-CuI_{1-x} ($0.1<x<1.0$), as a novel polycrystalline AgI-CuI solid solution, produced by mechanochemically method at room temperature. The authors found that the phase transition temperature rises from 149 to 376 °C as the CuI content increases. In addition, the behavior of Ag^+ conductivity in the AgI-CuI system, as well as the diffusion phase change seen in differential scanning calorimetric DSC, were discussed in connection to mixed phases.

In Chapter 4, we describe the structure, morphology, and functional characteristics of (Ag,Cu)I thin films synthesized by a two-step method at room temperature. The metallic copper and silver alloy was deposited by magnetron sputtering before being iodinated with iodine vapor. We synthesized a transparent conductive material with interesting optoelectronic characteristics using this approach.

1.7 Deposition techniques

Many works focus on optoelectronic properties of CuI thin films prepared by different techniques. V***apour reaction*** between copper and iodine was the first way to obtain CuI structure in 1907 [98]. The prepared films exhibited good p-type conductivity with hole density and mobility reach to 5 × 10^{18} cm^{-3} and 6 cm^2 V^{-1} s^{-1}, respectively. However, this method produces a very rough film's surface, which limits its applicability in different fields. Pulsed laser deposition (PLD) [4], thermal evaporation [16] and reactive sputtering [99], have been employed in order to enhance the film structure. S***olution based coating techniques,*** like spin and spray coatings [22,100], were also used. These low cost and reproducible techniques do not require heavy equipment, and could offer high quality films. The next part of this chapter will describe and compare different techniques used for CuI growth. This section is only dedicated to CuI elaboration, but the listed method can be also used to deposit either AgI or (Ag,Cu)I films.

1.7.1 Spin-coating

Spin-coating has become the most widely used solution-processing procedure in laboratories due to its simplicity and low cost. CuI powder can be dissolved in a varied solvents, including acetonitrile [19,22,83,101,102], 2-methoxyethanol [20,103] dipropyl sulphide [104,105], even

deionized water, to make precursor inks. The as-deposited CuI thin films have a polycrystalline microstructure with high optical transmittance (>90%), smooth surface with a RMS value of 0.6 nm, and 5.1 $cm^2.V^{-1}. s^{-1}$ Hall mobility [1]. Acetonitrile was shown to be favourable in the production of smooth CuI thin films with RMS values of less than <1 nm.

1.7.2 Spray coating, and inkjet printing methods

CuI thin films were also deposited by spray coating [106] and ink-jet printing, which are one of the most scalable process. Choi *et al.* [100] published the first CuI thin film transistor TFT in 2016 employing ink-jet printing at a temperature of 150 °C. TFTs with optimum field-effect mobility of 1.86 $cm^2.V^{-1}. s^{-1}$ and I_{on}/I_{off} of $10–10^2$ were tested.

1.7.3 PLD method

Recent researches investigate PLD-grown CuI thin films characteristics [4] using KrF excimer laser ablating a CuI target. Since ionized impurity scattering is minimized with increasing temperature, hole concentration decreases increasing the mobility. At 240 °C, the hole concentration could be adjusted throughout an extensive range of $5 \times 10^{16}–10^{19}$ cm^{-3}, with a Hall mobility maximum reaching 20 $cm^2 V^{-1} s^{-1}$.The film surface was relatively rough (RMS≈4 nm), similar to the iodination deposition technique, and smooth surfaces were only obtainable at low growth temperatures. Another disadvantage of the PLD method is its limited surface deposition area and high cost, which limits large-area samples fabrication.

1.7.4 Vapor iodination method

The vapor method technique remains the most popular method for γ-CuI film synthesis [1,66,107]. A metallic copper film deposited by magnetron sputtering is iodided in an iodine vapor. During iodine vapor exposure, metallic Cu film is transformed into CuI. At a moderate temperature of 120 °C, the chemical reaction between copper and iodine vapor is accelerated, due to the high volatility of iodine.100 nm-thick transparent γ-CuI thin layer can be formed in 20 minutes. CuI thin films show 50% of optical transmittance [3].With range of hole density of (10^{18}- 10^{19})cm^{-3} and hole mobility of 6 cm^2 V^{-1} s^{-1}, CuI thin films have excellent p-type semiconducting characteristics. Unfortunately, with this fast technique, CuI films exhibits rough surfaces (RMS >30 nm) to be integrated into thin films stacking.

1.7.5 Solid iodination method

To deposit γ-CuI, Yamada *et al.* [3] devised a solid-iodination method at room temperature, based on the chemical reaction between Cu_3N and iodine. CuI thin films show 70% of optical transmittance, hole density between $4\times10^{17}$and 10^{18} cm^{-3} and hole mobility between 9 and 21 cm^2 V^{-1} s^{-1}, an improved surface morphology with an RMS ≈ 10 nm.

1.7.6 Vacuum thermal evaporation method

Zi *et al.* [108] reported the deposition of CuI thin films on substrates in a vacuum thermal evaporation chamber. The pressed CuI powders were placed in the evaporation boat to develop a transparent CuI thin film with a low RMS value of 2 nm at room temperature [16]. At higher annealing temperatures, the grain sizes increased with annealing temperature pointing to increase

crystallinity in the films [111]. Cao *et al*. [108] observed 90 % of optical transmittance, hole density $3.0\times10^{19}cm^{-3}$ and hole mobility 25 $cm^2\ V^{-1}\ s^{-1}$, under the optimal substrate temperature of 120 °C. These results indicate that the growth high-quality p-type CuI films by thermal deposition is a simple process.

1.7.7 Reactive sputtering method

CuI thin films were successfully deposited using nonreactive radio frequency (RF) and direct current (DC) magnetron sputtering techniques [2,21,110–114]. In comparison to conventional RF and DC sputtering, reactive sputtering presents important advantage when one take into account the difficulties associated with sintering ceramic CuI target. A metallic Cu disk is used as the target and iodine vapor is supplied continuously during the process. Due to high plasma density and high Cu target electrical conductivity, uniform films could be grown. Cu/I ratio was easily adjusted using this approach, I-rich CuI had the highest CuI conductivity of 283 $S.cm^{-1,}$ with high transmission of 60–85% in the visible spectral range [99]. Yang [113] recently studied the growth mechanism and kinetics of sputtered CuI thin films in detail. At high substrate temperature (358 °C) and high growth rate, uniform structure with a smooth surface (RMS= 2-3 nm) CuI samples were obtained.

1.8 Conclusion

In this chapter, the most relevant information to our studied materials is presented. The basic physical and structural properties of copper and silver halides have been pointed. The main focus has been dedicated to CuI, AgI, and their alloy. A brief introduction on the need of wide bandgap

semiconductor (WBG) and its applications in energy conversion approaches has been highlighted. Comparison between the current and commercial WBG and our case of study, copper halides, has also been discussed. For both CuI and AgI, the crystal structure and phase transitions between the different phases were displayed. In addition, the band structure and the optical properties of both systems were discussed in details. Moreover, the current reported applications of the studied materials, based on their physical and structural properties, have been stated. Finally, the chapter ends with a discussion on the several deposition techniques reported in the literature. Compared to the different techniques, a two-step process including the deposition of both copper and silver thin films and their iodination seems easiest. Indeed, such a two-step process avoids introducing gaseous iodine into vacuum chambers that may contaminate the deposition chamber. It also allows better control in terms of thickness, process duration, and iodine addition amount.

In this thesis, we used sputtering method to synthesize metallic copper and silver-copper alloys films followed by an iodination step using iodine vapour. Experimental details on copper-based films growth will be described in the second chapter of this work.

References

[1] A. Liu, H. Zhu, M. Kim, J. Kim, Y. Noh, Engineering Copper Iodide (CuI) for Multifunctional p-Type Transparent Semiconductors and Conductors, Adv. Sci. (2021) 2100546. https://doi.org/10.1002/advs.202100546.

[2] C. Yang, M. Kneiβ, M. Lorenz, M. Grundmann, Room-temperature synthesized copper iodide thin film as degenerate p-type transparent conductor with a boosted figure of merit, Proc. Natl. Acad. Sci. U. S. A. 113 (2016) 12929–12933. https://doi.org/10.1073/pnas.1613643113.

[3] N. Yamada, R. Ino, Y. Ninomiya, Truly Transparent p-Type γ-CuI Thin Films with High Hole Mobility, Chem. Mater. 28 (2016) 4971–4981. https://doi.org/10.1021/acs.chemmater.6b01358.

[4] P. Storm, M.S. Bar, G. Benndorf, S. Selle, C. Yang, H. von Wenckstern, M. Grundmann, M. Lorenz, High mobility, highly transparent, smooth, p-type CuI thin films grown by pulsed laser deposition, APL Mater. 8 (2020) 091115. https://doi.org/10.1063/5.0021781.

[5] J.-H. Cha, D.-Y. Jung, Air-Stable Transparent Silver Iodide–Copper Iodide Heterojunction Diode, ACS Appl. Mater. Interfaces. 9 (2017) 43807–43813. https://doi.org/10.1021/acsami.7b14378.

[6] X. Yu, T.J. Marks, A. Facchetti, Metal oxides for optoelectronic applications, Nat. Mater. 15 (2016) 383–396. https://doi.org/10.1038/nmat4599.

[7] X.-L. Shi, J. Zou, Z.-G. Chen, Advanced Thermoelectric Design: From Materials and Structures to Devices, Chem. Rev. 120 (2020) 7399–7515. https://doi.org/10.1021/acs.chemrev.0c00026.

[8] C.V. Manzano, O. Caballero-Calero, M. Tranchant, E. Bertero, P. Cervino-Solana, M. Martin-Gonzalez, L. Philippe, Thermal conductivity reduction by nanostructuration in electrodeposited CuNi alloys, J. Mater. Chem. C. 9 (2021) 3447–3454. https://doi.org/10.1039/D1TC00307K.

[9] T. Kamiya, H. Hosono, Material characteristics and applications of transparent amorphous oxide semiconductors, NPG Asia Mater. 2 (2010) 15–22. https://doi.org/10.1038/asiamat.2010.5.

[10] H.A. Al-Jawhari, A review of recent advances in transparent p-type Cu2O-based thin film transistors, Mater. Sci. Semicond. Process. 40 (2015) 241–252. https://doi.org/10.1016/j.mssp.2015.06.063.

[11] Y. Chen, Y. Sun, X. Dai, B. Zhang, Z. Ye, M. Wang, H. Wu, Tunable electrical properties of NiO thin films and p-type thin-film transistors, Thin Solid Films. 592 (2015) 195–199. https://doi.org/10.1016/j.tsf.2015.09.025.

[12] A. Liu, H. Zhu, Y.-Y. Noh, Solution-processed inorganic p-channel transistors: Recent advances and perspectives, Mater. Sci. Eng. R Rep. 135 (2019) 85–100. https://doi.org/10.1016/j.mser.2018.11.001.

[13] Z. Wang, P.K. Nayak, J.A. Caraveo-Frescas, H.N. Alshareef, Recent Developments in p-Type Oxide Semiconductor Materials and Devices, Adv. Mater. 28 (2016) 3831–3892. https://doi.org/10.1002/adma.201503080.

[14] A. Liu, H. Zhu, Y.-Y. Noh, Molecule Charge Transfer Doping for p-Channel Solution-Processed Copper Oxide Transistors, Adv. Funct. Mater. 30 (2020) 2002625. https://doi.org/10.1002/adfm.202002625.

[15] R. Woods-Robinson, Y. Han, H. Zhang, T. Ablekim, I. Khan, K.A. Persson, A. Zakutayev, Wide Band Gap Chalcogenide Semiconductors, Chem. Rev. 120 (2020) 4007–4055. https://doi.org/10.1021/acs.chemrev.9b00600.

[16] M. Grundmann, F.-L. Schein, M. Lorenz, T. Böntgen, J. Lenzner, H. von Wenckstern, Cuprous iodide: A p-type transparent semiconductor, history, and novel applications: Cuprous iodide, Phys. Status Solidi A. (2013) n/a-n/a. https://doi.org/10.1002/pssa.201329349.

[17] N. Yamada, R. Ino, H. Tomura, Y. Kondo, Y. Ninomiya, High-Mobility Transparent p-Type CuI Semiconducting Layers Fabricated on Flexible Plastic Sheets: Toward Flexible Transparent Electronics, Adv. Electron. Mater. 3 (2017) 1700298. https://doi.org/10.1002/aelm.201700298.

[18] G.A. Sepalage, S. Meyer, A. Pascoe, A.D. Scully, F. Huang, U. Bach, Y.-B. Cheng, L. Spiccia, Copper(I) Iodide as Hole-Conductor in Planar Perovskite Solar Cells: Probing the Origin of J–V Hysteresis, Adv. Funct. Mater. 25 (2015) 5650–5661. https://doi.org/10.1002/adfm.201502541.

[19] Y. Zhong, Q. Zhang, Y. Wei, Q. Li, Y. Zhang, Self-assembled monolayer modified copper(I) iodide hole transport layer for efficient polymer solar cells, Chin. Phys. B. 27 (2018) 078802. https://doi.org/10.1088/1674-1056/27/7/078802.

[20] T. Jun, J. Kim, M. Sasase, H. Hosono, Material Design of p-Type Transparent Amorphous Semiconductor, Cu–Sn–I, Adv. Mater. 30 (2018) 1706573. https://doi.org/10.1002/adma.201706573.

[21] V. Raj, T. Lu, M. Lockrey, R. Liu, F. Kremer, L. Li, Y. Liu, H.H. Tan, C. Jagadish, Introduction of TiO2 in CuI for Its Improved Performance as a p-Type Transparent Conductor, ACS Appl. Mater. Interfaces. 11 (2019) 24254–24263. https://doi.org/10.1021/acsami.9b05566.

[22] A. Liu, H. Zhu, W.-T. Park, S.-J. Kang, Y. Xu, M.-G. Kim, Y.-Y. Noh, Room-Temperature Solution-Synthesized p-Type Copper(I) Iodide Semiconductors for Transparent Thin-Film Transistors and Complementary Electronics, Adv. Mater. 30 (2018) 1802379. https://doi.org/10.1002/adma.201802379.

[23] A. Liu, H. Zhu, W.-T. Park, S.-J. Kim, H. Kim, M.-G. Kim, Y.-Y. Noh, High-performance p-channel transistors with transparent Zn doped-CuI, Nat. Commun. 11 (2020) 4309. https://doi.org/10.1038/s41467-020-18006-6.

[24] C. Yang, D. Souchay, M. Kneiß, M. Bogner, H.M. Wei, M. Lorenz, O. Oeckler, G. Benstetter, Y.Q. Fu, M. Grundmann, Transparent flexible thermoelectric material based on non-toxic earth-abundant p-type copper iodide thin film, Nat. Commun. 8 (2017) 16076. https://doi.org/10.1038/ncomms16076.

[25] F.-L. Schein, H. von Wenckstern, M. Grundmann, Transparent *p* -CuI/ *n* -ZnO heterojunction diodes, Appl. Phys. Lett. 102 (2013) 092109. https://doi.org/10.1063/1.4794532.

[26] Best Research-Cell Efficiency Chart, (n.d.). https://www.nrel.gov/pv/cell-efficiency.html (accessed June 21, 2021).

[27] Y. Guo, Q. Wang, Y. Kawazoe, P. Jena, A New Silicon Phase with Direct Band Gap and Novel Optoelectronic Properties, Sci. Rep. 5 (2015) 14342. https://doi.org/10.1038/srep14342.

[28] A. BenMoussa, A. Soltani, U. Schühle, K. Haenen, Y.M. Chong, W.J. Zhang, R. Dahal, J.Y. Lin, H.X. Jiang, H.A. Barkad, B. BenMoussa, D. Bolsee, C. Hermans, U. Kroth, C. Laubis, V. Mortet, J.C. De Jaeger, B. Giordanengo, M. Richter, F. Scholze, J.F. Hochedez, Recent developments of wide-bandgap

semiconductor based UV sensors, Diam. Relat. Mater. 18 (2009) 860–864. https://doi.org/10.1016/j.diamond.2008.11.013.

[29] G. Huang, K. Wang, C.N. Markides, Efficiency limits of concentrating spectral-splitting hybrid photovoltaic-thermal (PV-T) solar collectors and systems, Light Sci. Appl. 10 (2021) 28. https://doi.org/10.1038/s41377-021-00465-1.

[30] M. Shur, Wide band gap semiconductor technology: State-of-the-art, Solid-State Electron. 155 (2019) 65–75. https://doi.org/10.1016/j.sse.2019.03.020.

[31] W. Pacuski, Optical spectroscopy of wide gap diluted magnetic semiconductors based on ZnO and GaN, (n.d.) 139.

[32] L.-C. Chao, P.-C. Chiang, S.-H. Yang, J.-W. Huang, C.-C. Liau, J.-S. Chen, C.-Y. Su, Zinc oxide nanodonut prepared by vapor-phase transport process, Appl. Phys. Lett. 88 (2006) 251111. https://doi.org/10.1063/1.2214146.

[33] T. Shinagawa, H. Takahashi, M. Izaki, Direct growth of ZnO crystals on various Cu substrates by Cu-catalyzed chemical bath deposition, CrystEngComm. 21 (2019) 2476–2480. https://doi.org/10.1039/C9CE00244H.

[34] J. Komiyama, Y. Abe, S. Suzuki, H. Nakanishi, Stress reduction in epitaxial GaN films on Si using cubic SiC as intermediate layers, J. Appl. Phys. 100 (2006) 033519. https://doi.org/10.1063/1.2226988.

[35] R. c. Hanson, J. r. Hallberg, C. Schwab, Elastic and piezoelectric constants of the cuprous halides, Appl. Phys. Lett. 21 (1972) 490–492. https://doi.org/10.1063/1.1654230.

[36] Electronic structure of the copper halides CuCl, CuBr and Cul, Mater. Sci. Eng. B. 39 (1996) 95–100. https://doi.org/10.1016/0921-5107(95)01518-3.

[37] D. Ahn, J.D. Song, S.S. Kang, J.Y. Lim, S.H. Yang, S. Ko, S.H. Park, S.J. Park, D.S. Kim, H.J. Chang, J. Chang, Intrinsically p-type cuprous iodide semiconductor for hybrid light-emitting diodes, Sci. Rep. 10 (2020) 3995. https://doi.org/10.1038/s41598-020-61021-2.

[38] L. O'Reilly, O.F. Lucas, P.J. McNally, A. Reader, G. Natarajan, S. Daniels, D.C. Cameron, A. Mitra, M. Martinez-Rosas, A.L. Bradley, Room-temperature ultraviolet luminescence from γ-CuCl grown on near lattice-matched silicon, J. Appl. Phys. 98 (2005) 113512. https://doi.org/10.1063/1.2138799.

[39] Y. Masumoto, T. Kawamura, K. Era, Biexciton lasing in CuCl quantum dots, Appl. Phys. Lett. 62 (1993) 225–227. https://doi.org/10.1063/1.109000.

[40] N. Nishida, K. Saiki, A. Koma, Heteroepitaxy of CuCl on GaAs and Si substrates, Surf. Sci. 324 (1995) 149–158. https://doi.org/10.1016/0039-6028(94)00708-X.

[41] T. Kawazoe, Y. Masumoto, Luminescence Hole Burning and Quantum Size Effect of Charged Excitons in CuCl Quantum Dots, Phys. Rev. Lett. 77 (1996) 4942–4945. https://doi.org/10.1103/PhysRevLett.77.4942.

[42] M. Nakayama, H. Ichida, H. Nishimura, Bound-biexciton photoluminescence in CuCl thin films grown by vacuum deposition, J. Phys. Condens. Matter. 11 (1999) 7653–7662. https://doi.org/10.1088/0953-8984/11/39/320.

[43] A. Goldmann, J. Tejeda, N.J. Shevchik, M. Cardona, Density of valence states of CuCl, CuBr, CuI, and AgI, Phys. Rev. B. 10 (1974) 4388–4402. https://doi.org/10.1103/PhysRevB.10.4388.

[44] L. Kleinman, K. Mednick, Energy bands and effective masses of CuCl, Phys. Rev. B. 20 (1979) 2487–2490. https://doi.org/10.1103/PhysRevB.20.2487.

[45] J. Valenta, J. Dian, P. Gilliot, B. Hönerlage, Photoluminescence and Optical Gain in CuBr Semiconductor Nanocrystals, Phys. Status Solidi B. 224 (2001) 313–317. https://doi.org/10.1002/1521-3951(200103)224:1<313::AID-PSSB313>3.0.CO;2-B.

[46] L. O'Reilly, G. Natarajan, P.J. McNally, D. Cameron, O.F. Lucas, M. Martinez-Rosas, L. Bradley, A. Reader, S. Daniels, Growth and characterisation of wide-bandgap, I-VII optoelectronic materials on silicon, J. Mater. Sci. Mater. Electron. 16 (2005) 415–419. https://doi.org/10.1007/s10854-005-2307-3.

[47] L. O'Reilly, A. Mitra, G. Natarajan, O.F. Lucas, P.J. McNally, S. Daniels, D.C. Cameron, A.L. Bradley, A. Reader, Impact on structural, optical and electrical properties of CuCl by incorporation of Zn for n-type doping, J. Cryst. Growth. 287 (2006) 139–144. https://doi.org/10.1016/j.jcrysgro.2005.10.057.

[48] UV emission on a Si substrate: Optical and structural properties of γ-CuCl on Si grown using liquid phase epitaxy techniques - Cowley - 2009 - physica status solidi (a) - Wiley Online Library, (n.d.). https://onlinelibrary-wiley-com.bases-doc.univ-lorraine.fr/doi/abs/10.1002/pssa.200881282 (accessed June 21, 2021).

[49] A. Cowley, F.O. Lucas, E. Gudimenko, M.M. Alam, D. Danieluk, A.L. Bradley, P.J. McNally, Electroluminescence of -CuBr thin films via vacuum evaporation depositon, J. Phys. Appl. Phys. 43 (2010) 165101. https://doi.org/10.1088/0022-3727/43/16/165101.

[50] P. Knauth, Y. Massiani, M. Pasquinelli, Semiconductor Properties of Polycrystalline CuBr by Hall Effect and Capacitive Measurements, Phys. Status Solidi A. 165 (1998) 461–465. https://doi.org/10.1002/(SICI)1521-396X(199802)165:2<461::AID-PSSA461>3.0.CO;2-W.

[51] D. Ahn, S.-H. Park, Cuprous halides semiconductors as a new means for highly efficient light-emitting diodes, Sci. Rep. 6 (2016) 20718. https://doi.org/10.1038/srep20718.

[52] L. O'Reilly, A. Mitra, F.O. Lucas, G. Natarajan, P.J. McNally, S. Daniels, A. Lankinen, D. Lowney, A.L. Bradley, D.C. Cameron, Characterisation of n-type γ-CuCl on Si for UV optoelectronic applications, J. Mater. Sci. Mater. Electron. 18 (2007) 57–60. https://doi.org/10.1007/s10854-007-9173-0.

[53] S. Miyake, S. Hoshino, T. Takenaka, On the Phase Transition in Cuprous Iodide, J. Phys. Soc. Jpn. 7 (1952) 19–24. https://doi.org/10.1143/JPSJ.7.19.

[54] W. BÜHRER, W. HÄLG, CRYSTAL STRUCTURE OF HIGH-TEMPERATURE CUPROUS IODIDE AND CUPROUS BROMIDE, in: R.D. ARMSTRONG (Ed.), Int. Symp. Solid Ion. Ion.-Electron. Conduct., Pergamon, 1977: pp. 701–704. https://doi.org/10.1016/B978-0-08-021592-1.50010-6.

[55] Y. Shan, G. Li, G. Tian, J. Han, C. Wang, S. Liu, H. Du, Y. Yang, Description of the phase transitions of cuprous iodide, J. Alloys Compd. 477 (2009) 403–406. https://doi.org/10.1016/j.jallcom.2008.10.026.

[56] D.A. Keen, S. Hull, The high-temperature structural behaviour of copper(I) iodide, J. Phys. Condens. Matter. 7 (1995) 5793–5804. https://doi.org/10.1088/0953-8984/7/29/007.

[57] Copper(I) iodide, Wikipedia. (2021). https://en.wikipedia.org/w/index.php?title=Copper(I)_iodide&oldid=1034819988 (accessed September 13, 2021).

[58] M. Cardona, Optical Properties of the Silver and Cuprous Halides, Phys. Rev. 129 (1963) 69–78. https://doi.org/10.1103/PhysRev.129.69.

[59] J. Wang, J. Li, S.-S. Li, Native *p* -type transparent conductive CuI via intrinsic defects, J. Appl. Phys. 110 (2011) 054907. https://doi.org/10.1063/1.3633220.

[60] A. Goldmann, Band Structure and Optical Properties of Tetrahedrally Coordinated Cu- and Ag-Halides, Phys. Status Solidi B. 81 (1977) 9–47. https://doi.org/10.1002/pssb.2220810102.

[61] W. Yu, G. Benndorf, Y. Jiang, K. Jiang, C. Yang, M. Lorenz, M. Grundmann, Control of Optical Absorption and Emission of Sputtered Copper Iodide Thin Films, Phys. Status Solidi RRL – Rapid Res. Lett. 15 (2021) 2000431. https://doi.org/10.1002/pssr.202000431.

[62] V.A. Nikitenko, S.G. Stoyukhin, V.I. Popolitov, Yu.M. Mininzon, Luminescence of CuI single crystals, J. Appl. Spectrosc. 34 (1981) 410–413. https://doi.org/10.1007/BF00614221.

[63] N.N. Boroznovskaya, L.A. Zyryanova, I.V. Pekov, Luminescent properties of natural copper and silver iodides: Evidence for their composition and structure, Dokl. Earth Sci. 438 (2011) 864–865. https://doi.org/10.1134/S1028334X11060298.

[64] L.A. Zyryanova, N.N. Boroznovskaya, K.V. Tolochko, Luminescent properties of natural copper and silver iodide, Mineral. Mag. 75 (2011). https://www.elibrary.ru/item.asp?id=23445316 (accessed June 25, 2021).

[65] T. Goto, T. Takahashi, M. Ueta, Exciton Luminescence of CuCl, CuBr and CuI Single Crystals, J. Phys. Soc. Jpn. 24 (1968) 314–327. https://doi.org/10.1143/JPSJ.24.314.

[66] G. Lin, F. Zhao, Y. Zhao, D. Zhang, L. Yang, X. Xue, X. Wang, C. Qu, Q. Li, L. Zhang, Luminescence Properties and Mechanisms of CuI Thin Films Fabricated by Vapor Iodization of Copper Films, Materials. 9 (2016) 990. https://doi.org/10.3390/ma9120990.

[67] A. Aktar, S. Ahmmed, J. Hossain, A.B.Md. Ismail, Solution-Processed Synthesis of Copper Oxide (CuxO) Thin Films for Efficient Photocatalytic Solar Water Splitting, ACS Omega. 5 (2020) 25125–25134. https://doi.org/10.1021/acsomega.0c02754.

[68] N. Yamada, Y. Tanida, H. Murata, T. Kondo, S. Yoshida, Wide-Range-Tunable p-Type Conductivity of Transparent CuI1−xBrx Alloy, Adv. Funct. Mater. 30 (2020) 2003096. https://doi.org/10.1002/adfm.202003096.

[69] H. Zhu, A. Liu, Y.-Y. Noh, Transparent Inorganic Copper Bromide (CuBr) p-Channel Transistors Synthesized From Solution at Room Temperature, IEEE Electron Device Lett. 40 (2019) 769–772. https://doi.org/10.1109/LED.2019.2904737.

[70] C.M. Chang, L.M. Davis, E.K. Spear, R.G. Gordon, Chemical Vapor Deposition of Transparent, p-Type Cuprous Bromide Thin Films, Chem. Mater. 33 (2021) 1426–1434. https://doi.org/10.1021/acs.chemmater.0c04586.

[71] A. Annadi, H. Gong, Success in both p-type and n-type of a novel transparent AgCuI alloy semiconductor system for homojunction devices, Appl. Mater. Today. 20 (2020) 100703. https://doi.org/10.1016/j.apmt.2020.100703.

[72] K.H.L. Zhang, K. Xi, M.G. Blamire, R.G. Egdell, P-type transparent conducting oxides, J. Phys. Condens. Matter. 28 (2016) 383002. https://doi.org/10.1088/0953-8984/28/38/383002.

[73] D. Beretta, N. Neophytou, J.M. Hodges, M.G. Kanatzidis, D. Narducci, M. Martin- Gonzalez, M. Beekman, B. Balke, G. Cerretti, W. Tremel, A. Zevalkink, A.I. Hofmann, C. Müller, B. Dörling, M. Campoy-Quiles, M. Caironi, Thermoelectrics: From history, a window to the future, Mater. Sci. Eng. R Rep. 138 (2019) 100501. https://doi.org/10.1016/j.mser.2018.09.001.

[74] M.K. Yadav, B. Sanyal, First-principles study of thermoelectric properties of CuI, Mater. Res. Express. 1 (2014) 015708. https://doi.org/10.1088/2053-1591/1/1/015708.

[75] J. Loureiro, N. Neves, R. Barros, T. Mateus, R. Santos, S. Filonovich, S. Reparaz, C.M. Sotomayor-Torres, F. Wyczisk, L. Divay, R. Martins, I. Ferreira, Transparent aluminium zinc oxide thin films with enhanced thermoelectric properties, J Mater Chem A. 2 (2014) 6649–6655. https://doi.org/10.1039/C3TA15052F.

[76] V. Brinzari, I. Damaskin, L. Trakhtenberg, B.K. Cho, G. Korotcenkov, Thermoelectrical properties of spray pyrolyzed indium oxide thin films doped by tin, Thin Solid Films. Complete (2014) 225–231. https://doi.org/10.1016/j.tsf.2013.12.009.

[77] S. Ohta, T. Nomura, H. Ohta, K. Koumoto, High-temperature carrier transport and thermoelectric properties of heavily La- or Nb-doped SrTiO3 single crystals, J. Appl. Phys. 97 (2005) 034106. https://doi.org/10.1063/1.1847723.

[78] C. Yang, M. Kneiß, F.-L. Schein, M. Lorenz, M. Grundmann, Room-temperature Domain-epitaxy of Copper Iodide Thin Films for Transparent CuI/ZnO Heterojunctions with High Rectification Ratios Larger than 109, Sci. Rep. 6 (2016). https://doi.org/10.1038/srep21937.

[79] A. Annadi, N. Zhang, D. Boon Kiang Lim, H. Gong, New Transparent Magnetic Semiconductor NixCu1–xI which Can Perform as Either P-type or N-type and Success in the P–N Homojunction Diode, ACS Appl. Mater. Interfaces. 12 (2020) 6048–6055. https://doi.org/10.1021/acsami.9b19550.

[80] J.H. Lee, W.-J. Lee, T.H. Kim, T. Lee, S. Hong, K.H. Kim, Transparentp-CuI/n-BaSnO3-$\updelta$heterojunctions with a high rectification ratio, J. Phys. Condens. Matter. 29 (2017) 384004. https://doi.org/10.1088/1361-648X/aa7cbf.

[81] K. Ding, Q.C. Hu, D.G. Chen, Q.H. Zheng, X.G. Xue, F. Huang, Fabrication and Energy Band Alignment of n-ZnO/p-CuI Heterojunction, IEEE Electron Device Lett. 33 (2012) 1750–1752. https://doi.org/10.1109/LED.2012.2218274.

[82] N. Yamada, Y. Kondo, R. Ino, Low-Temperature Fabrication and Performance of Polycrystalline CuI Films as Transparent p-Type Semiconductors, Phys. Status Solidi A. 216 (2019) 1700782. https://doi.org/10.1002/pssa.201700782.

[83] H. Wu, L. Liang, X. Wang, H. Zhang, J. Bao, H. Cao, Solution-processed amorphous p-type Cu-Sn-I thin films for transparent Cu-Sn-I/IGZO p–n junctions, Appl. Phys. Lett. 118 (2021) 222107. https://doi.org/10.1063/5.0051631.

[84] N. Yamada, Y. Kondo, X. Cao, Y. Nakano, Visible-blind wide-dynamic-range fast-response self-powered ultraviolet photodetector based on CuI/In-Ga-Zn-O heterojunction, Appl. Mater. Today. 15 (2019) 153–162. https://doi.org/10.1016/j.apmt.2019.01.007.

[85] J. Liu, Piezo-phototronic effect enhanced UV photodetector based on CuI/ZnO double-shell grown on flexible copper microwire, (2016) 7.

[86] D. Ahn, S.-H. Park, Cuprous halides semiconductors as a new means for highly efficient light-emitting diodes, Sci. Rep. 6 (2016) 20718. https://doi.org/10.1038/srep20718.

[87] S.-D. Baek, D.-K. Kwon, Y.C. Kim, J.-M. Myoung, Violet Light-Emitting Diodes Based on p-CuI Thin Film/n-MgZnO Quantum Dot Heterojunction, ACS Appl. Mater. Interfaces. 12 (2020) 6037–6047. https://doi.org/10.1021/acsami.9b18507.

[88] X. Li, P. Li, Z. Wu, D. Luo, H.-Y. Yu, Z.-H. Lu, Review and perspective of materials for flexible solar cells, Mater. Rep. Energy. 1 (2021) 100001. https://doi.org/10.1016/j.matre.2020.09.001.

[89] R. Singh, P.K. Singh, B. Bhattacharya, H.-W. Rhee, Review of current progress in inorganic hole-transport materials for perovskite solar cells, Appl. Mater. Today. 14 (2019) 175–200. https://doi.org/10.1016/j.apmt.2018.12.011.

[90] S. Hull, D.A. Keen, Pressure-induced phase transitions in AgCl, AgBr, and AgI, Phys. Rev. B. 59 (1999) 750–761. https://doi.org/10.1103/PhysRevB.59.750.

[91] P.V. Smith, A tight-binding approach to the electronic structure of the silver halides—I: Silver chloride, J. Phys. Chem. Solids. 37 (1976) 581–587. https://doi.org/10.1016/0022-3697(76)90107-4.

[92] A. Dashora, A. Marwal, K.R. Soni, B.L. Ahuja, Electronic properties and compton profiles of silver iodide, Pramana. 74 (2010) 1017–1027. https://doi.org/10.1007/s12043-010-0077-9.

[93] S. Mochizuki, Y. Ohta, Excitons in AgI, J. Lumin. 87–89 (2000) 299–301. https://doi.org/10.1016/S0022-2313(99)00321-X.

[94] S. Mochizuki, Stacking faults and excitons in AgI, Phys. B Condens. Matter. 308–310 (2001) 1042–1045. https://doi.org/10.1016/S0921-4526(01)00919-X.

[95] R. Dahan, J. Dror, N. Croitoru, Characterization of chemically formed silver iodide layers for hollow infrared guides, Mater. Res. Bull. 27 (1992) 761–766. https://doi.org/10.1016/0025-5408(92)90084-D.

[96] D.B. Mohan, C.S. Sunandana, Nanophases in mechanochemically synthesized AgI–CuI system: structure, phase stability and phase transitions, J. Phys. Chem. Solids. 65 (2004) 1669–1677. https://doi.org/10.1016/j.jpcs.2004.04.007.

[97] M.R. Johan, T.S. Leng, N.L. Hawari, S. Suan, Phase Transition and Complex Impedance Studies of Mechano- Chemically Synthesized AgI-CuI Solid Solutions, Int J Electrochem Sci. 6 (2011) 10.

[98] K. Bädeker, Über die elektrische Leitfähigkeit und die thermoelektrische Kraft einiger Schwermetallverbindungen, Ann. Phys. 327 (1907) 749–766. https://doi.org/10.1002/andp.19073270409.

[99] C. Yang, M. Kneiβ, M. Lorenz, M. Grundmann, Room-temperature synthesized copper iodide thin film as degenerate p-type transparent conductor with a boosted figure of merit, Proc. Natl. Acad. Sci. 113 (2016) 12929–12933. https://doi.org/10.1073/pnas.1613643113.

[100] C.-H. Choi, J.Y. Gorecki, Z. Fang, M. Allen, S. Li, L.-Y. Lin, C.-C. Cheng, C.-H. Chang, Low-temperature, inkjet printed p-type copper(I) iodide thin film transistors, J. Mater. Chem. C. 4 (2016) 10309–10314. https://doi.org/10.1039/C6TC03234F.

[101] W.-Y. Chen, L.-L. Deng, S.-M. Dai, X. Wang, C.-B. Tian, X.-X. Zhan, S.-Y. Xie, R.-B. Huang, L.-S. Zheng, Low-cost solution-processed copper iodide as an alternative to PEDOT:PSS hole transport layer for efficient and stable inverted planar heterojunction perovskite solar cells, J. Mater. Chem. A. 3 (2015) 19353–19359. https://doi.org/10.1039/C5TA05286F.

[102] W. Sun, H. Peng, Y. Li, W. Yan, Z. Liu, Z. Bian, C. Huang, Solution-Processed Copper Iodide as an Inexpensive and Effective Anode Buffer Layer for Polymer Solar Cells, J. Phys. Chem. C. 118 (2014) 16806–16812. https://doi.org/10.1021/jp412784q.

[103] S. Inudo, M. Miyake, T. Hirato, Electrical properties of CuI films prepared by spin coating, Phys. Status Solidi A. 210 (2013) 2395–2398. https://doi.org/10.1002/pssa.201329319.

[104] H.J. Lee, S. Lee, Y. Ji, K.G. Cho, K.S. Choi, C. Jeon, K.H. Lee, K. Hong, Ultrahigh-Mobility and Solution-Processed Inorganic P-Channel Thin-Film Transistors Based on a Transition-Metal Halide Semiconductor, ACS Appl. Mater. Interfaces. 11 (2019) 40243–40251. https://doi.org/10.1021/acsami.9b12654.

[105] S. Lee, H.J. Lee, Y. Ji, S.M. Choi, K.H. Lee, K. Hong, Vacancy engineering of a solution processed CuI semiconductor: tuning the electrical properties of inorganic P-channel thin-film transistors, J. Mater. Chem. C. 8 (2020) 9608–9614. https://doi.org/10.1039/D0TC02005B.

[106] N.N. Shlenskaya, A.S. Tutantsev, N.A. Belich, E.A. Goodilin, M. Grätzel, A.B. Tarasov, Electrodeposition of porous CuSCN layers as hole-conducting material for perovskite solar cells, Mendeleev Commun. 28 (2018) 378–380. https://doi.org/10.1016/j.mencom.2018.07.012.

[107] F. Geng, L. Yang, B. Dai, S. Guo, G. Gao, L. Xu, J. Han, A. Bolshakov, J. Zhu, Enhanced transmittance and mobility of p-type copper iodide thin films prepared at room temperature via a layer-by-layer approach, Surf. Coat. Technol. 361 (2019) 396–402. https://doi.org/10.1016/j.surfcoat.2019.01.057.

[108] M. Zi, J. Li, Z. Zhang, X. Wang, J. Han, X. Yang, Z. Qiu, H. Gong, Z. Ji, B. Cao, Effect of deposition temperature on transparent conductive properties of γ-CuI film prepared by vacuum thermal evaporation: Effect of deposition temperature on transparent conductive properties of γ-CuI film, Phys. Status Solidi A. 212 (2015) 1466–1470. https://doi.org/10.1002/pssa.201532015.

[109] C. Moditswe, C.M. Muiva, P. Luhanga, A. Juma, Effect of annealing temperature on structural and optoelectronic properties of γ-CuI thin films prepared by the thermal evaporation method, Ceram. Int. 43 (2017) 5121–5126. https://doi.org/10.1016/j.ceramint.2017.01.026.

[110] C. Yang, D. Souchay, M. Kneiß, M. Bogner, H.M. Wei, M. Lorenz, O. Oeckler, G. Benstetter, Y.Q. Fu, M. Grundmann, Transparent flexible thermoelectric material based on non-toxic earth-abundant p-type copper iodide thin film, Nat. Commun. 8 (2017). https://doi.org/10.1038/ncomms16076.

[111] T. Tanaka, K. Kawabata, M. Hirose, Transparent, conductive CuI films prepared by rf-dc coupled magnetron sputtering, Thin Solid Films. 281–282 (1996) 179–181. https://doi.org/10.1016/0040-6090(96)08607-5.

[112] C. Yang, M. Kneiß, F.-L. Schein, M. Lorenz, M. Grundmann, Room-temperature Domain-epitaxy of Copper Iodide Thin Films for Transparent CuI/ZnO Heterojunctions with High Rectification Ratios Larger than 109, Sci. Rep. 6 (2016). https://doi.org/10.1038/srep21937.

[113] C. Yang, E. Rose, W. Yu, T. Stralka, F. Geng, M. Lorenz, M. Grundmann, Controllable Growth of Copper Iodide for High-Mobility Thin Films and Self-Assembled Microcrystals, ACS Appl. Electron. Mater. 2 (2020) 3627–3632. https://doi.org/10.1021/acsaelm.0c00692.

[114] E. Krüger, V. Zviagin, C. Yang, C. Sturm, R. Schmidt-Grund, M. Grundmann, Temperature dependence of the dielectric function of thin film CuI in the spectral range (0.6–8.3) eV, Appl. Phys. Lett. 113 (2018) 172102. https://doi.org/10.1063/1.5051963.

Chapter 2
Synthesis of copper iodide thin films and characterizing techniques

Graphical Abstract

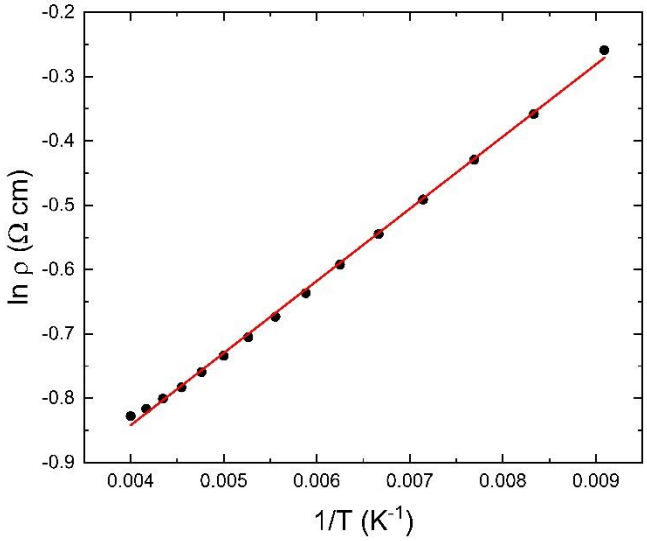

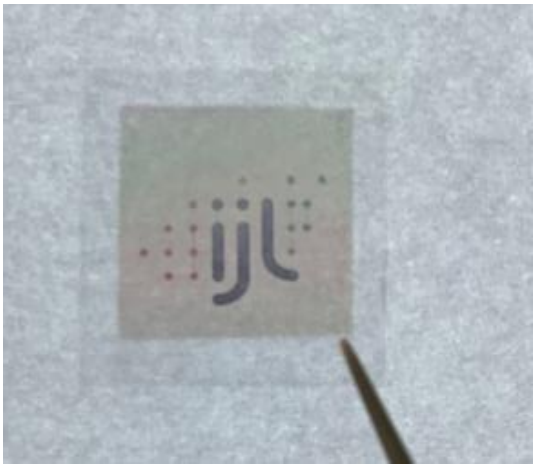

Due to its Arrhenius behavior, the prepared material iodide film exhibit a semiconductor nature as clearly evidenced by the activation energy evolution with the temperature and optically transparent copper iodide film

Contents

2.1 Introduction .....
2.2 Metallic thin film growth and elaboration setup.....
2.3 Vapor iodination .....
2.4 Characterization methods .....
2.4.1 X-ray diffraction (XRD) .....
2.4.2 Scanning electron microscopy (SEM) .....
2.4.3 Electron probe microanalysis (EPMA).....
2.4.4 Transmission electron microscopy (TEM). .....
2.5 Four-point probe method .....
2.6 Hall Effect Measurements .....
2.7 UV-visible spectroscopy.....
2.8 Photoluminescence .....
2.9 Conclusion.....

2.1 Introduction

A holistic characterization of thin films calls for a detailed understanding of composition, crystallization degree, thickness, morphology, adhesion, and physical properties related to their mechanical, magnetic, optical, electrical, and other attributes [1,2]. In the present thesis, copper iodide and copper silver iodide were synthesized via iodination of sputtered copper and copper-silver thin films, respectively. This chapter will describe methods used to synthesize and characterize the iodide films. The film structure was characterized using θ–2θ X-ray diffraction (XRD), and the morphology was imaged using scanning electron microscopy (SEM) and transmission electron microscopy (TEM). The film composition was measured using an electron probe microanalyser (EPMA) and energy dispersive X-ray spectroscopy (EDS or EDX). The optical properties were characterized using UV-visible spectrophotometry in the 250-800 nm range. Photoluminescence (PL) was used to evaluate the optical behavior of the studied material with respect to defect chemistry. The electrical properties were measured using the Hall Effect and four-point probe technique. The resistivity, carrier density, and mobility have been deduced from Hall measurements at both room temperature and low temperature in the van der Pauw geometry. This chapter provides an in-depth examination of each of these techniques.

2.2 Metallic thin film growth and elaboration setup

Magnetron sputtering is among a multitude of PVD techniques. Metallic copper and copper-silver alloys thin films were synthesized at room temperature via magnetron sputtering. In this process, a metallic Cu target was sputtered in the presence of argon plasma to deposit Cu films while a co-sputtering process using Cu and Ag targets was used to deposit a Cu-Ag alloy. The argon plasma is composed of argon ions, electrons and neutral argon atoms and is used to sputter

the metallic targets. All metallic thin films described in this thesis were deposited on soda lime glass and silicon (CODEX international, Si, <100>, intrinsic, thickness 500 µm, resistivity of 200 Ω cm) substrates. The dimensions of the copper and the silver targets (purity higher than 99.9 %) were 50.8 mm diameter and 3 mm thick. A 40 L sputtering chamber was used to synthesize samples, as shown in (Figure 2.1). The pumping system consists of a primary pump and a secondary one. The primary pumps provided an initial vacuum of about 10^{-2} Pa. Once this vacuum level was achieved, a turbomolecular pump was used to achieve a base vacuum of about 10^{-6} Pa. The sputtering chamber was equipped with two magnetron systems separated by 130 mm each other. The distance between the substrates and the target is fixed at 50 mm. The Ag and Cu metallic targets were co-sputtered in the presence of an argon plasma under a fixed argon flow rate (30 standard cubic centimeter per minute (sccm)). Prior to deposition, ultrasonic cleaning was performed using ethanol for approximately 3 minutes per sample. Drying was performed using dust free air flow. The substrates were introduced into the deposition chamber and a radiofrequency plasma (13.56 MHz) etching step was performed to clean surface substrates before the deposition. During the film growth process, the copper target was powered by an Advanced Energy Pinnacle +5 kW DC-pulsed power supply. The discharge frequency was fixed at 50 kHz, and the off time was fixed at 4 µs with an applied current to the copper target (I_{Cu}) fixed at 0.3 A. The silver target was also powered by an Advanced Energy Pinnacle +5 kW DC-pulsed power supply. The discharge frequency was fixed at 100 kHz, and the off time was fixed at 4 µs with an applied current to the silver target (I_{Ag}) ranging between 0.04 and 0.25 A. For these deposition conditions, the total pressure was 0.5 Pa. To ensure the composition homogeneity, the substrate-holder was rotating. Metallic films were deposited without intentional heating and the substrate temperature was lower than 50 °C. The growth rate for Cu was approximately 12.5 nm/minute

while that of the film with the highest silver content was approx. 45 nm/min. The growth rate of silver-copper alloys is higher than that of pure copper and is function of the silver content. The deposition duration was adjusted to get the expected thickness. In most of the case, as-deposited copper films have a thickness of 50 nm. The thickness of silver-copper alloys was ranging between 290 and 450 nm as a function of the silver content. The samples were grown on glass and silicon substrates (2×2 cm^2).

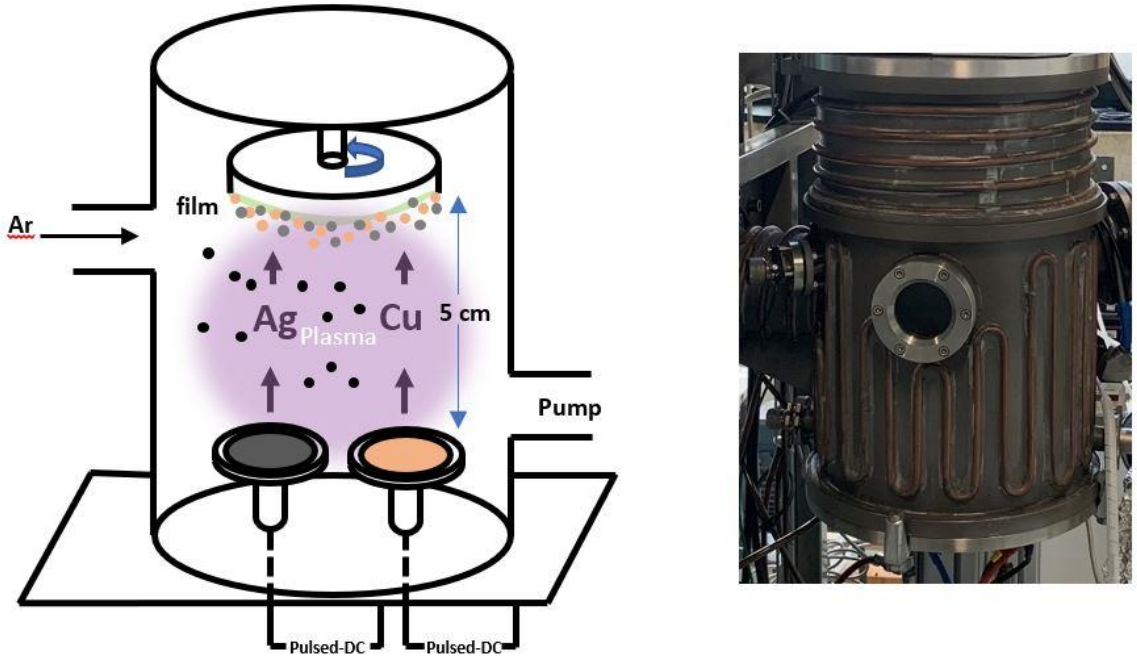

Figure 2.1: Schematic view of the magnetron sputtering chamber used for Cu and Cu-Ag thin film growth. Black, beige and grey circles represent Ar, Cu and Ag respectively.

2.3 Vapor iodination

The synthesis of copper or silver iodide based on iodination of metallic films is widely described in the literature [3–7]. Two main processes are used: iodination either in solid phase or

in gas phase. For our work, we have chosen to use the gas phase process because it may guarantee a higher homogeneity of the iodide film.

The Cu or Cu-Ag thin films deposited on glass or silicon substrates are introduced into a Pyrex® chamber. This reactor is heated using an oil bath (temperature ranging between room temperature to 120 °C). Once the desired temperature is reached, a certain amount (few tenths of gram) of solid I_2 is introduced into the heated Pyrex® chamber. The reactor is hermetically closed using a neoprene butyl seal and tight screw cap. It can be correctly noted that solid iodide immersion in the reactor leads to iodide sublimation due to its extreme volatility even at room temperature. Additionally, the high reactivity of iodide results in near-immediate reaction with copper or silver, making each step extremely time-sensitive. The timer is turned on when the reactor is closed. When the indicated time has elapsed, the reactor is removed from the oil, the seal and the gasket are opened, and the sample immediately taken out from the reactor. These steps are carried out in rapid succession and must be executed with precision. Iodide films are adherent to the substrates and are optically transparent, Figure 2.2.

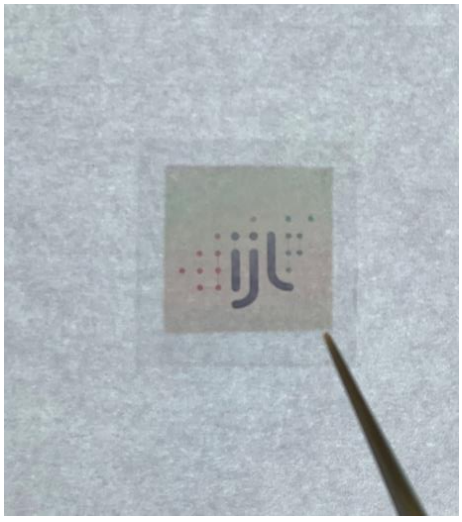

Figure 2.2: Optically transparent copper iodide films formed using the process detailed in section 2.3

These apparatuses or tools may include the neoprene butyl stopper and reactor which are properly washed using potassium iodide solution, Figure 2.3. Potassium iodide is used to dissolve the remaining solid iodine into an I_3^- solution.

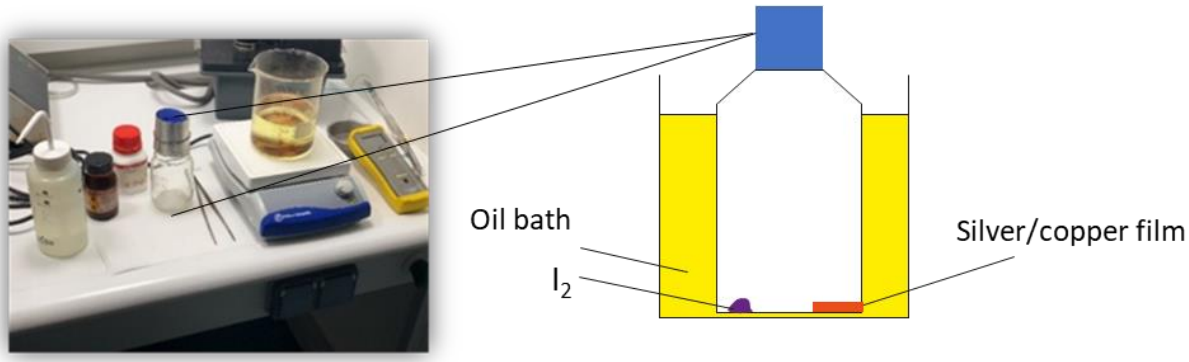

Figure 2.3: Equipment used for the iodination treatment and schematic view of the process used for the growth of copper iodide.

2.4 Characterization methods

2.4.1 X-ray diffraction (XRD)

XRD is an essential tool in material science used to determine the crystalline structure in powder, monolithic solids, and thin film samples [8]. X-ray diffraction is based on the elastic scattering of an X-ray beam on a crystalline material leading to interference that is all the more intense as the material is crystallized. A detector is measuring the intensity of the diffracted beam. The intensity is plotted as a function of the diffracting angles. Since the wavelength of X-rays is in the same order of magnitude than the distance between atoms, XRD is a powerful method to describe the crystallographic structure of crystallized materials. For each material, the position of the diffracted peaks and their intensity act as an ID card of the analyzed material.

XRD follows Bragg's law (Eq. 2.1) as depicted in Figure 2.4. The diffraction angle (θ) is a pivotal element of the technique [8].

$$n\,\lambda = 2\,d_{hkl}\sin\theta \quad (2.1)$$

where n denotes the positive integer of diffraction, λ is the X-ray wavelength, d_{hkl} represents the interplanar distance of the plane (hkl).

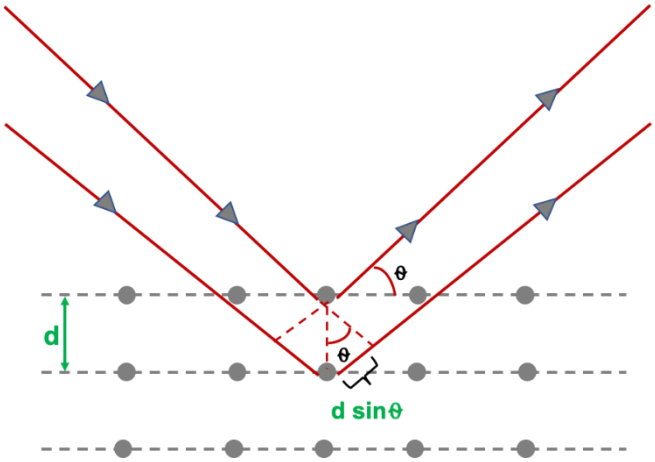

Figure 2.4: Schematic representation of Bragg's Law

To characterize our thin films, we used the Bragg-Brentano configuration with a focused beam geometry. The X-ray source (copper anti-cathode) is fixed while the angle of the sample and the detector is changing (the detector rotates at twice the speed of the sample). The Brucker D8 Advance diffractometer was used for all XRD measurements using Cu $K_{\alpha 1}$ wavelength (λ=0.15406 nm) obtained with a Ge monochromator. The obtained data is compared to the XRD database available in JCPDS and EVA software. An example of one X-ray diffractogram of a CuI film is presented in Figure 2.5.

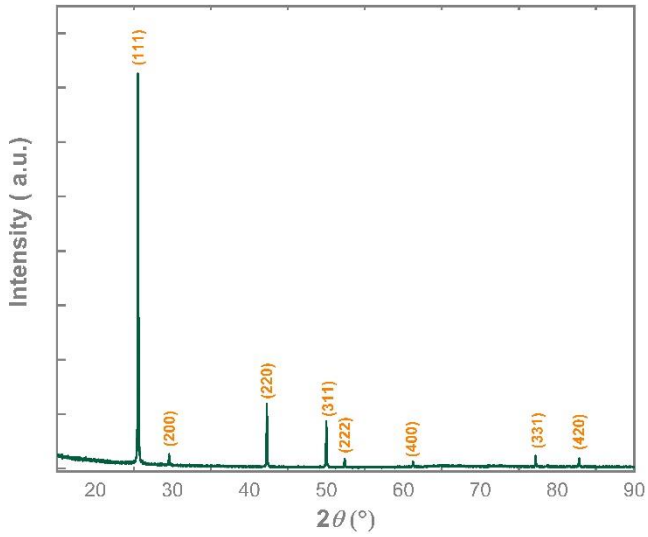

Figure 2.5: Example of a X-ray diffractogram of a CuI thin film synthesized at 75 °C with 0.15 g of I_2 on glass substrate.

2.4.2 Scanning electron microscopy (SEM)

SEM is a widely method used to characterize the morphology of materials in bulk or thin film form. For our work, a field emission gun ZEISS Gemini SEM 500 microscope was used for SEM analysis. In a SEM, a primary electron beam is accelerated using a few tens of thousands kV. Figure 2.6 shows a detailed illustration of SEM interactions, including X-ray, secondary electrons, and backscattered electron emissions. Secondary electrons are collected during sample sweeping, producing an image that gives insight into the surface topography and geometry. Images produced using backscattered electrons show contrast using elemental weight. Figure 2.7 shows an example of SEM characterization of a CuI thin film.

The energy dispersive X-ray spectroscopy (EDS) is a chemical microanalysis method performed with the support of SEM. The technique uses X-ray beams produced from the sample by bombarding the surface with an electron beam. X-rays characteristic to each element fingerprint can then be collected from the sample volume on the nano and microscale [9]. The EDS X-ray

detector measures emitted X-rays in comparison to the known elemental energies, providing detailed chemical or atomic compositional data [9]. Since the thickness of our CuI films is ranging between 100 and 400 nm, the EDS analysis also evidences the silicon substrate, i.e. the electron penetration depth is higher than the film thickness. Thus, the EDS spectrum Figure 2.8 evidences the presence of copper, iodine and silicon into the analyzed sample. To estimate the film composition, we only take into account the copper and iodine peaks. EDS spectra were collected using a 20 keV primary electron beam.

In the EDS calculations, ZAF corrections are used to convert apparent concentrations (raw peak intensity) into (semi-quantitative) concentrations that are corrected for inter-element matrix effects. Z is the atomic number correction, which is related to the element's stopping power; A is the absorption correction, which states that less energetic X-rays from lighter elements are absorbed by heavier elements as they leave the sample; and F is the fluorescence correction, which states that a more energetic X-ray leaving the sample can fluoresce a lower-energy X-ray from a lighter element.

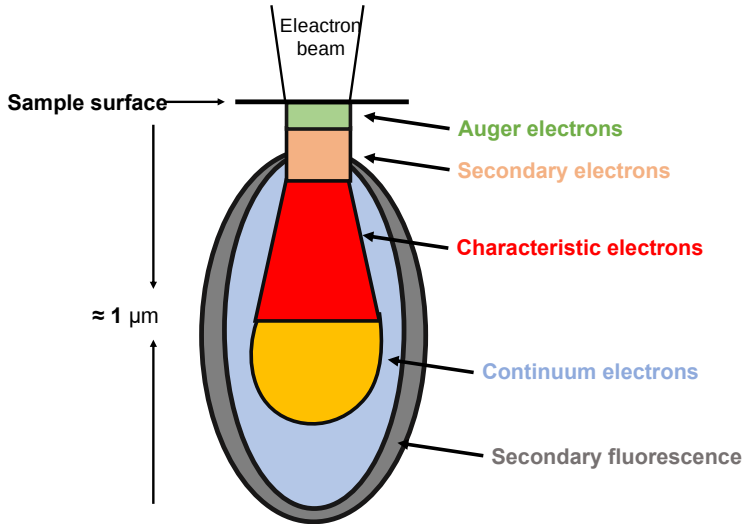

Figure 2.6: Representation of electron interaction with a sample during SEM characterization adapted from [10].

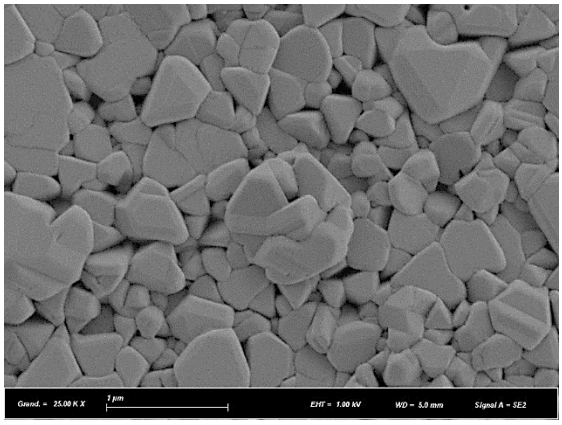

Figure 2.7: SEM image of the surface morphology of CuI thin film prepared on glass substrate.

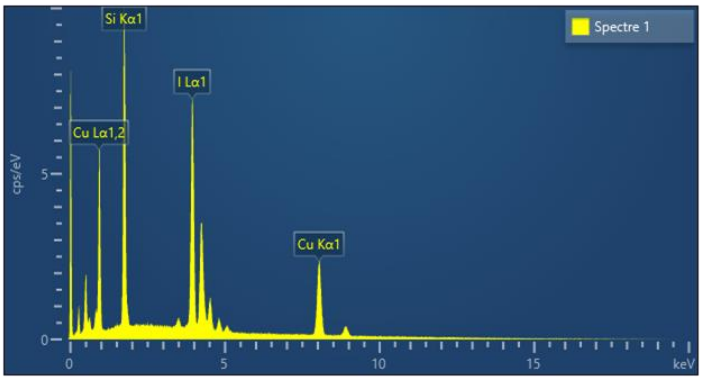

Figure 2.8: EDS spectrum of a CuI film deposited on silicon substrate.

2.4.3 Electron probe microanalysis (EPMA)

Electron probe microanalysis (EPMA) was developed around 1950 when Raimond CASTAING, a French graduate student working under the supervision of André Guinier, built his first microanalyser [10]. EPMA provides better results than standard SEM/EDS systems. The general sensitivity, analysis of light elements, and risks of erroneous qualitative spectra interpretation are all superior with EPMA due to the internal properties of WDS. EDS has a much lower spectral resolution and dead detector time. This technique provides outstanding stability and measurement repeatability thanks to the excitation beam regulation system and sophisticated sample stage capabilities. The principle of EPMA is to bombard the sample surface with a focused electron beam and collect the emitted X-rays. The X-rays are dispersed using Bragg diffraction on a mobile monochromator, which provides a complete X-ray spectrum ranging from zero to over 10 keV. The dispersion technique is called wavelength dispersive X-ray spectroscopy (WDS). The collected spectrum contains a continuous background (Bremsstrahlung emission) and characteristic peaks, which allow for elemental qualitative and quantitative analysis of the material. EPMA-WDS can

be carried out in dedicated instruments called “microprobes” which are usually fitted with 4 WDS spectrometers or in a high current SEM equipped with a single WDS spectrometer [11]. The film composition of synthesized samples was measured using a JEOL 8530-F EPMA. Quantitative measurements were performed at 20 kV and 50 nA using LiF-SP2 crystal and Pel6080-Cu standard for Cu, and MPET-SP4 crystal and RbI-n ° 10413 standard for I. A representative EPMA image of a CuI sample that evidences the different analysis zone is shown in Figure 2.9.

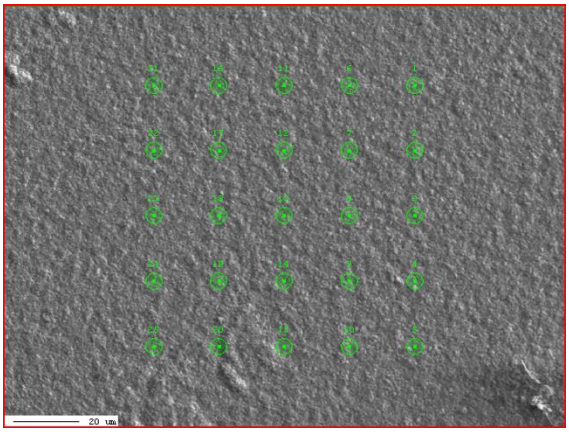

Figure 2.9 : Example of EPMA measurements spots on a CuI film.

2.4.4 Transmission electron microscopy (TEM)

TEM is an electron microscopy technique that relies on an electron beam to image and characterizes materials on the nano-scale. Specifically, the electron beam is transmitted through an ultra-thin specimen (approx. 100 nm thick). Interactions between these transmitted electrons and the sample bring specific information about the microstructure, the atomic arrangements, the crystallographic of the investigated materials. The main components of a TEM apparatus are the electron source (emitted from the electron gun), a sample holder, electromagnetic lenses, and detectors [12]. A set of electron lenses and apertures are placed before and after the sample holder to control and manipulate the emitted and the transmitted electron beams [13,14]. The column is operated under

high vacuum conditions in order to avoid electron interference and scattering by gas molecules [15]. The schematic diagram of the electron beam path in TEM is presented in Figure 2.10

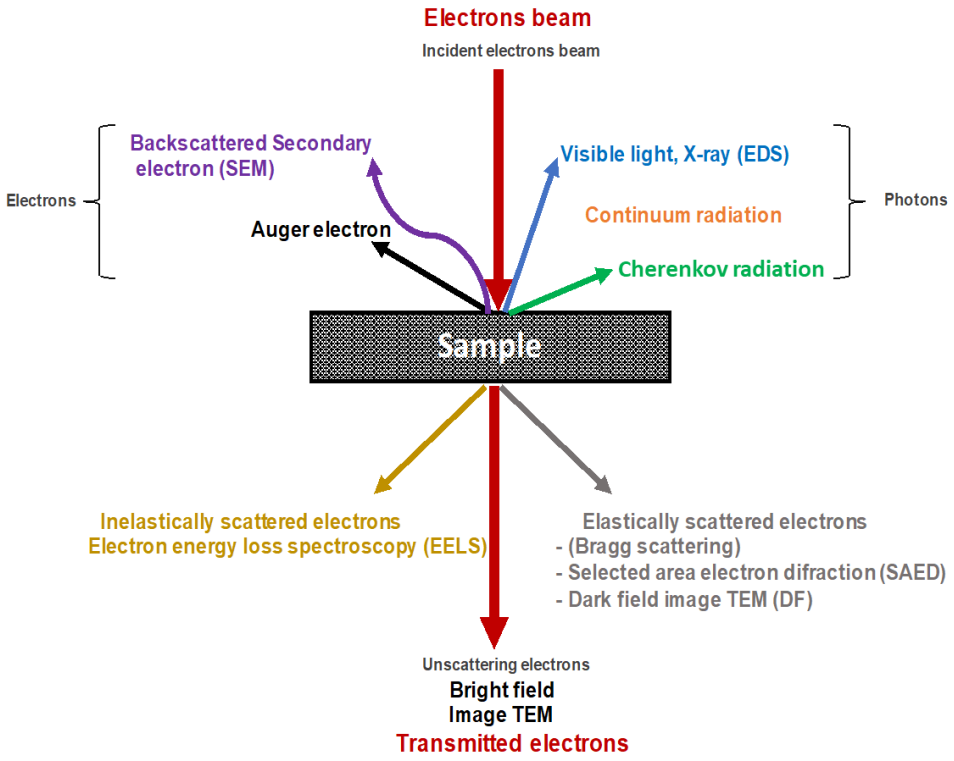

Figure 2.10: Different interactions of an electron beam with a material characterized with an transmission electron microscope.

The focused electron beam is generated at the electron gun and accelerated to the required high energy (few hundreds of kV) directed to the specimen. The transmitted and diffracted electrons are collected by an objective lens forming a diffraction pattern (DP) in the back focal plane and intermediate image in the image plane [16]. For TEM imaging, both an image and DP can be obtained. Switching between the two modes (image and DP) can be achieved by changing the strength of the intermediate lens and inserting a lens aperture. To collect an image, an objective aperture is used in the back focal plane. To collect the DP, and selected area electron diffraction (SAED) aperture is inserted in the image plane.

In imaging mode, bright field or dark field imaging can be used Figure 2.11 a,b. The imaging type is controlled by the position of the objective aperture. In bright field (BF) mode, the objective aperture oriented to allow only the transmitted beam to pass and form the image [17]. In dark field (DF) mode, the transmitted beam is blocked, and one or more diffracted beams are allowing to pass [17]. For imaging, a JEOL - ARM 200F Cold FEG TEM/STEM with TEM 0.19 nm and 0.078 nm scanning transmission electron microscopy (STEM) was used. The equipment has a component called GIF Quanta ER that is used for electron loss energy spectroscopy analyses.

The quality of the TEM analysis is based on the quality of the sample preparation. In our case the thin foil lamella was prepared by the focused ion beam (FIB) method to cut thin cross-sectional slices of the sample. An example of thin foil lamella is depicted in Figure 2.12. This was accomplished using a Helios Nano lab 600i FIB. There are two guns on the MEB-FIB: an electron gun and a gallium ion gun (Ga^{+}). Similarly to a conventional scanning electron microscope, the electron source is used to image the surface of the sample. The second gun fires a beam of Ga^{+} ions, tearing the sample's atoms apart and allowing it to thin.

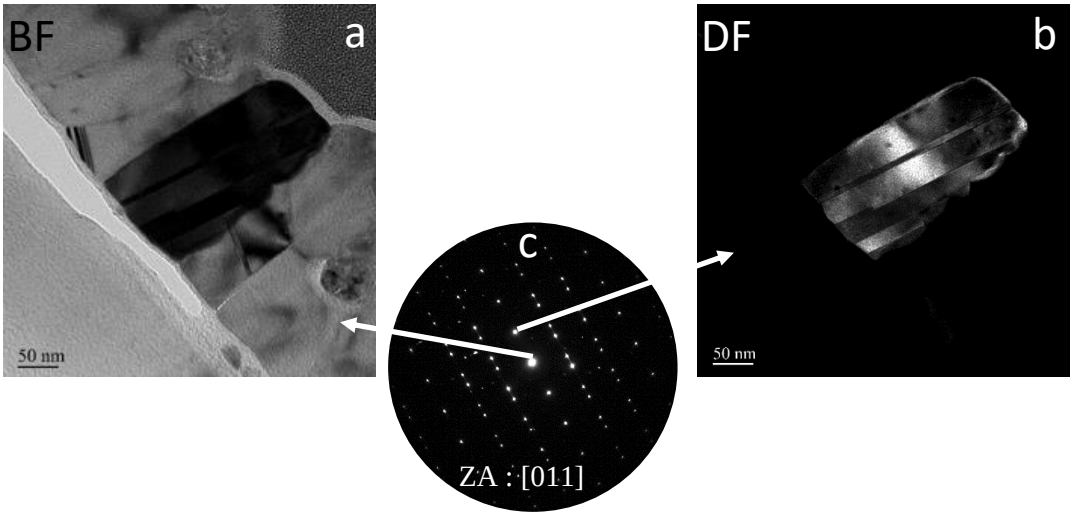

Figure 2.11: a) Bright and b) dark images as well as c) SAED pattern of a prepared CuI thin film sample synthesized with 0.15 g of I_2

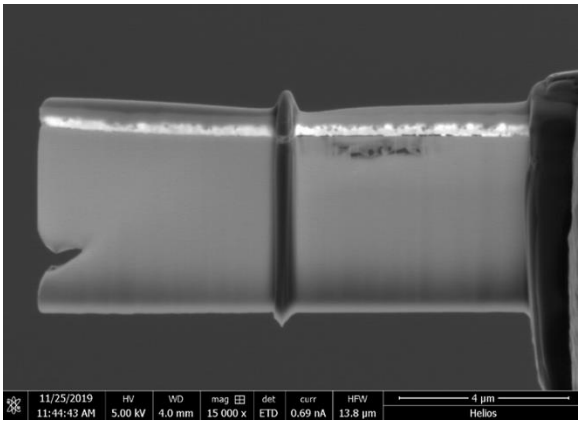

Figure 2.12: CuI lamella elaborated by FIB for TEM measurements.

Regarding the composition analysis, energy-dispersive X-ray spectroscopy (EDS) was used. An EDS system built into the TEM was used for semi-quantitative composition analysis of synthesized samples [18]. The electron beam is used to penetrate the sample and interact with core electrons by exciting them to upper energy levels. The relaxation of these electrons results in X-ray emissions characteristic to each element, providing detailed compositional information. EDS analysis using TEM of a CuI sample is shown in Figure 2.13.

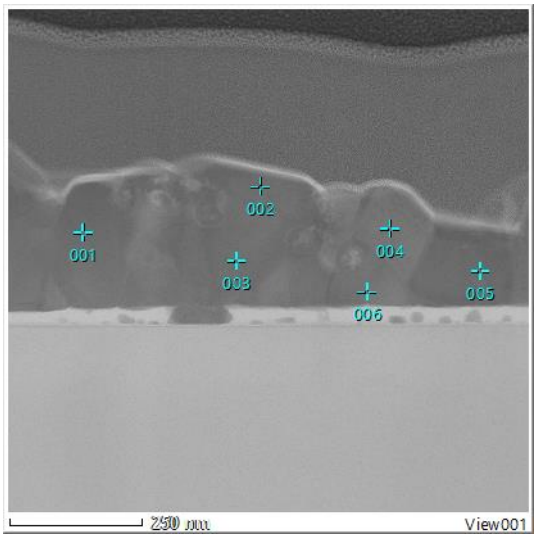

Figure 2.13: One example of EDS analysis of CuI film.

2.5 Four-point probe method

The four-point probe technique was used to measure the electrical resistivity of the CuI and (Ag,Cu)I films. The external probes are connected to a generator (Keithley® 237) which imposes a current (from nano-ampere to milliampere). The central probes are connected to a voltmeter (Keithley® 2700). This setup was used at room temperature and in ambient air. To estimate the electrical resistivity of a thin film, it is mandatory that the film is deposited on an insulating substrate to avoid its contribution. Four probes are placed in line with equal spacing of 1 mm between the probes. A current is applied between the external probe, while the voltage is measured between the internal probes Figure 2.14. This method allows to avoid taking into account the contact resistance. The measurement provides the ratio $\frac{|\Delta V|}{I}$, which is related to the resistivity (ρ in Ω cm) of materials according to the equation:

$$\rho = \frac{\pi}{\ln 2} t \frac{|\Delta V|}{I} \quad (2.2)$$

where the correction factor is equal to $\pi/\ln(2) = 4.53$, t indicates film thickness, I is the applied current, and V is the voltage measured between the inner probes.

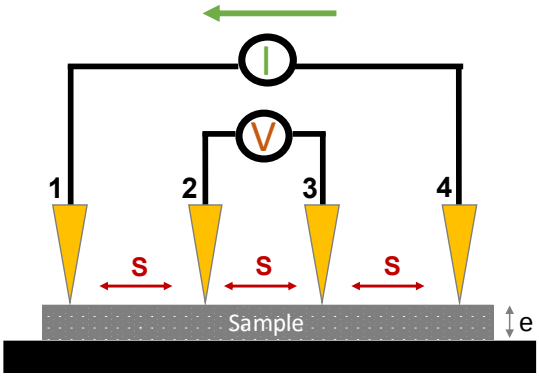

Figure 2.14: Schematic representation of the four point probe method

2.6 Hall Effect Measurements

In the presence of a perpendicular magnetic field B = (0, 0, B) along *z*, an electrical current in the *x* (longitudinal) direction induces an electric field E_y in the transverse (*y*) direction. The charge accumulation is caused by the Lorentz force. As shown in the schematic geometry of Hall effect measurements is presented in Figure 2. 15. The corresponding transverse voltage is the Hall voltage (V_H), which is described as

$$\text{Hall voltage } (V_H) = \frac{BI}{nqt} = \frac{R_H BI}{t} \quad (2.3)$$

Where *B* is magnetic field *B* along the *z* direction perpendicular to the sample, *I* is the electric current passing through the semiconductor along the *x* (longitudinal), *t* is the thickness of the sample in the direction of *B*, *q* is elementary charge of the charge carriers, and *n* is the density of charge carriers [19].

$$R_H = \frac{\mu}{\sigma} = \frac{1}{nq} \quad (2.4)$$

The Hall coefficient is denoted as R_H. The Hall coefficient of n-type materials is negative indicating that the primary charge carriers are negative, i.e. electrons.

The Hall coefficient and conductivity σ of the material can be related to material properties, density of charge carriers *n* and mobility μ by the following relations (q is the charge of the carrier):

$$\sigma = \frac{\mu}{R_H} = n.q.\mu \quad (2.5)$$

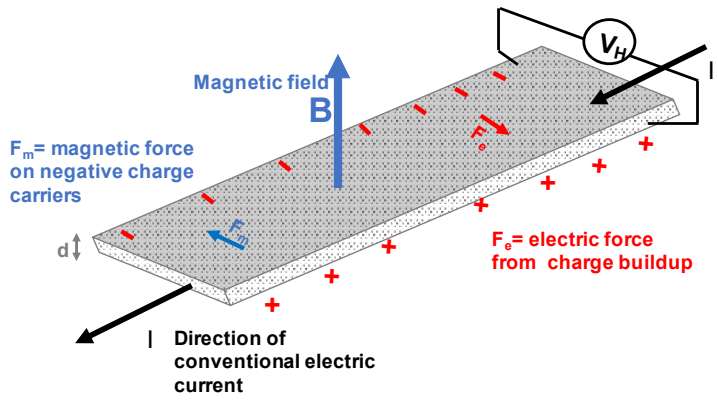

Figure 2.15: Schematic Representation of Hall effect measurement adapted from [20].

The electromagnetic force, magnetic force, and magnetic field are pivotal elements for equipment operation. In this work, Hall effect measurements in semiconductor materials used to deduce conductive type (p or n type), electrical resistivity, and mobility and carrier density in the Van der Pauw geometry (Ecopia, HMS-5000), that uses a magnetic field of 0.57 T. Most of the Hall effect measurements have been performed at room temperature.

Our setup can be cooled to low temperature by using liquid nitrogen. For some selected samples, measurements as a function of the temperature have been performed to show that the resistivity decreases exponentially with temperature, exhibiting Arrhenius type behavior. It clearly shows the semiconductor nature of the prepared material. The activation energy for $Ag_{0.33}Cu_{0.67}I$ was determined by fitting the given data and was found to be 9.6 meV Figure 2.16

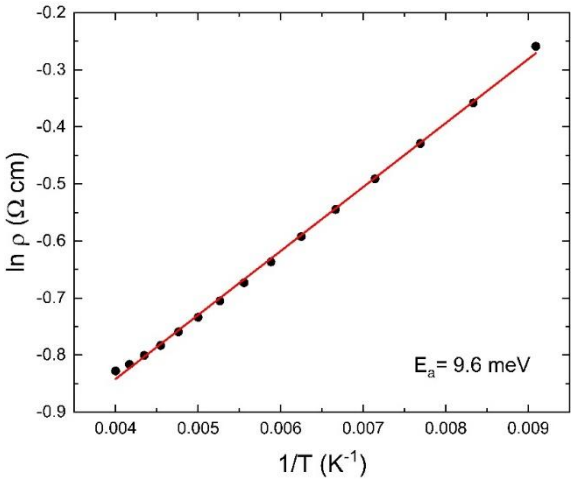

Figure 2.16: Arrhenius plot for calculation of apparent activation energy of (Ag,Cu)I film from 250 to 110 K for x=0.33.

2.7 UV-visible spectroscopy

Ultraviolet-visible spectrophotometry (UV-Vis) is a well-studied technique with a well-established ability to determine the optical properties of thin films [21]. Generated UV and visible beams are passed through a sample, and the transmitted beam intensity is measured. For the experiments outlined in this dissertation, soda-lime glass was the substrate of choice due to its high transmitting power exceeding 90%, as shown in Figure 2.17.

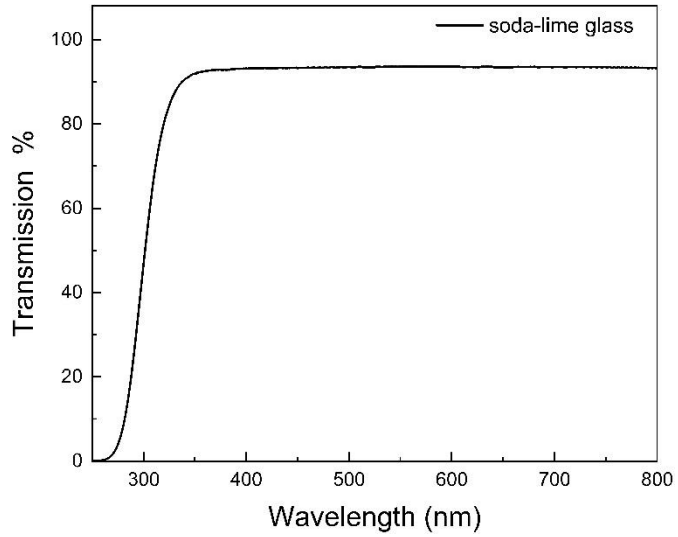

Figure 2.17: Transmittance of Soda Lime Glass

A Varian Cary 5000 UV-Vis-NIR was used to measure the transmittance of synthesized samples. The principle of this equipment is depicted in Figure 2.18. The light source generates the light that passes through the monochromator with mirrors aligned to transfer the light to the beam splitter. Two mirrors at opposite ends reflect the light, producing two beams, one going through the sample while the other passes through. The separated beams are then reflected in the detector.

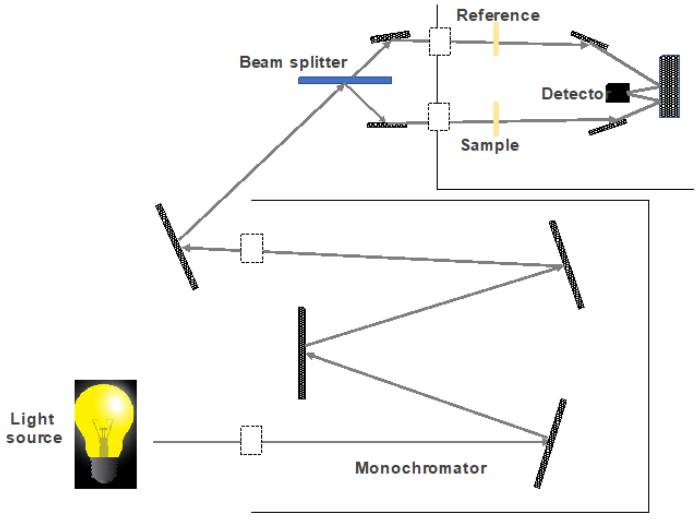

Figure 2.18: schematic illustration of a double beam spectrophotometer

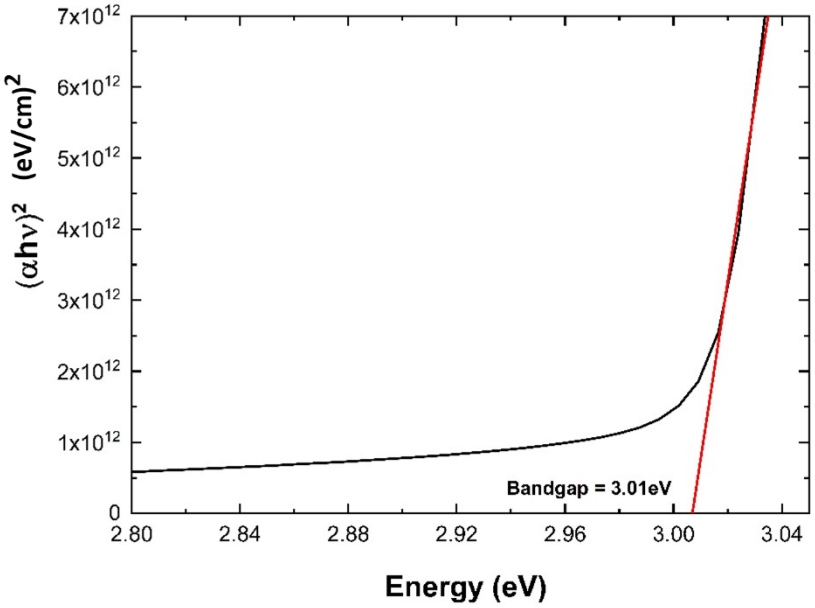

Figure 2.19: Depiction of a typical Tauc plot of CuI film

The UV-visible spectrophotometry can also be used to determine the optical band gap of a thin film using the Tauc method [22]. Neglecting the film reflectance (see section 1.4.5), the absorption coefficient (α) is determined from the transmitted intensity (T_{film}) and the film thickness (t at a specific wavelength).

$$\alpha = \frac{1}{t} ln \frac{1}{Tfilm} \qquad (2.6)$$

The optical band gap E_g is related to the absorption coefficient, and their relationship is described by the following equation.

$$(h\nu\alpha) = B\ (h\nu - E_g)^n \quad (2.7)$$

The *n* exponent shows the transmission nature of the material. In the case of CuI, *n* was $1/2$ indicating a semiconductor with direct allowed transition. *B* is a band tailing parameter constant. Obtained results were plotted in a graph similar to the one described in Figure 2.19.

2.8 Photoluminescence

Photoluminescence (PL) is the measurement of light emitted by materials subjected to an electromagnetic wave [23]. During the PL mechanism, electrons are excited, allowing them to move from the ground state to excited state. Each electronic state within a given material posesses different specific energies. Over time, the excited electrons relax back down to the ground state and release the absorbed energy in form of light emission (radiative process) and/or heat dissipation (nonradiative process). It is worth mentioning that the optical excitation energy should at least be equal to the energy difference between the two transition states. In semiconductor materials, radiative transitions can occur between the valence and conduction bands with energy differences equal to the bandgap or, alternatively, radiative transitions may involve localized defects and impurities [24]. Therefore, PL experiments can help in the identification of specific defects and impurities used to define the bandgap characteristics. PL measurements were performed using a spectrofluorometer (Fluorolog-Horiba) excited by 320 nm. A xenon arc lamp source was used, and the PL emission was analyzed by a detection system equipped with 150 grooves/mm gratings and a cooled silicon-based CCD camera.

In the case of copper iodide, emissions blue in color and strong in nature can be seen along with a weak red emission. Figure 2.20 shows a representative PL spectrum with three observable peaks.

Peak 1 is the highest at 410 nm, peak 2 occurs at 419 nm, and peak 3 is seen at 715 nm. In the following chapters, we will cover these peaks in significant detail.

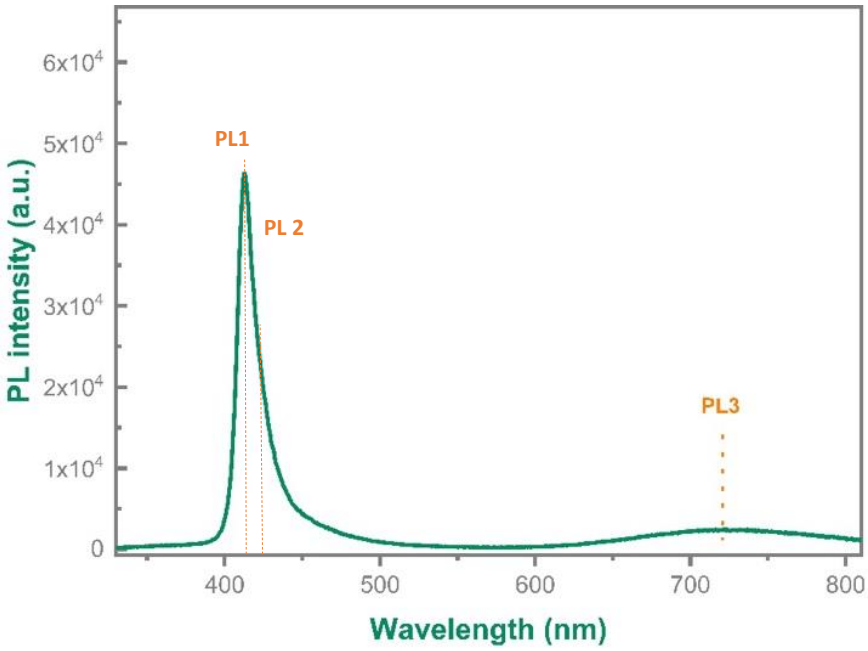

Figure 2.20: Photoluminescence spectra of a typical CuI film

2.9 Conclusion

This chapter examines the synthesis of copper and silver-copper iodide thin films and their characterization techniques. Specifically, this chapter examines XRD, SEM, EPMA, EDS, TEM, four-point probe method, Hall Effect measurements, UV-vis, and PL. The various techniques allow for a thorough analysis of the physical, atomic, electrical, and chemical characteristics of copper iodide ans silver copper iodide thin films. The next chapters will describe the characterization of both iodide thin films.

References

[1] H. Bubert, H. Jenett, eds., Surface and Thin Film Analysis: Principles, Instrumentation, Applications, 1st ed., Wiley, 2002. https://doi.org/10.1002/3527600167.

[2] J. Poortmans, V. Arkhipov, eds., Thin Film Solar Cells: Fabrication, Characterization and Applications, John Wiley & Sons, Ltd, Chichester, UK, 2006. https://doi.org/10.1002/0470091282.

[3] N. Yamada, R. Ino, Y. Ninomiya, Truly Transparent p-Type γ-CuI Thin Films with High Hole Mobility, Chem. Mater. 28 (2016) 4971–4981. https://doi.org/10.1021/acs.chemmater.6b01358.

[4] A. Annadi, H. Gong, Success in both p-type and n-type of a novel transparent AgCuI alloy semiconductor system for homojunction devices, Appl. Mater. Today. 20 (2020) 100703. https://doi.org/10.1016/j.apmt.2020.100703.

[5] M. Grundmann, F.-L. Schein, M. Lorenz, T. Böntgen, J. Lenzner, H. von Wenckstern, Cuprous iodide: A p-type transparent semiconductor, history, and novel applications: Cuprous iodide, Phys. Status Solidi A. (2013) n/a-n/a. https://doi.org/10.1002/pssa.201329349.

[6] J.-H. Cha, D.-Y. Jung, Air-Stable Transparent Silver Iodide–Copper Iodide Heterojunction Diode, ACS Appl. Mater. Interfaces. 9 (2017) 43807–43813. https://doi.org/10.1021/acsami.7b14378.

[7] A. Liu, H. Zhu, M. Kim, J. Kim, Y. Noh, Engineering Copper Iodide (CuI) for Multifunctional p-Type Transparent Semiconductors and Conductors, Adv. Sci. (2021) 2100546. https://doi.org/10.1002/advs.202100546.

[8] U. Pietsch, V. Holý, T. Baumbach, High-Resolution X-Ray Scattering, Springer New York, New York, NY, 2004. https://doi.org/10.1007/978-1-4757-4050-9.

[9] J.I. Goldstein, D.E. Newbury, J.R. Michael, N.W.M. Ritchie, J.H.J. Scott, D.C. Joy, Scanning Electron Microscopy and X-Ray Microanalysis, Springer, 2017.

[10] S.K. Sharma, X-Ray Spectroscopy, BoD – Books on Demand, 2012.

[11] M. Procop, M. Radtke, M. Krumrey, K. Hasche, S. Schädlich, W. Frank, Electron probe microanalysis (EPMA) measurement of thin-film thickness in the nanometre range, Anal. Bioanal. Chem. 374 (2002) 631–634. https://doi.org/10.1007/s00216-002-1514-5.

[12] C.B. Carter, D.B. Williams, Transmission Electron Microscopy: Diffraction, Imaging, and Spectrometry, Springer, 2016.

[13] Handbook of Charged Particle Optics - 2nd Edition - Jon Orloff - Rout, (n.d.). https://www.routledge.com/Handbook-of-Charged-Particle-Optics/Orloff/p/book/9781420045543 (accessed May 10, 2021).

[14] R.F. Egerton, Physical Principles of Electron Microscopy: An Introduction to TEM, SEM, and AEM, Springer US, 2005. https://doi.org/10.1007/b136495.

[15] L.E. Franken, K. Grünewald, E.J. Boekema, M.C.A. Stuart, A Technical Introduction to Transmission Electron Microscopy for Soft-Matter: Imaging, Possibilities, Choices, and Technical Developments, Small. 16 (2020) 1906198. https://doi.org/10.1002/smll.201906198.

[16] Z.L. Wang, Y. Liu, Z. Zhang, eds., Transmission Electron Microscopy and Spectroscopy, in: Handb. Nanophase Nanostructured Mater., Springer US, Boston, MA, 2002: pp. 372–441. https://doi.org/10.1007/0-387-23814-X_13.

[17] F. Krumeich, INTRODUCTION INTO TRANSMISSION AND SCANNING TRANSMISSION ELECTRON MICROSCOPY, (n.d.) 55.

[18] M. Scimeca, S. Bischetti, H.K. Lamsira, R. Bonfiglio, E. Bonanno, Energy Dispersive X-ray (EDX) microanalysis: A powerful tool in biomedical research and diagnosis, Eur. J. Histochem. EJH. 62 (2018). https://doi.org/10.4081/ejh.2018.2841.

[19] M. Grundmann, The Physics of Semiconductors: An Introduction Including Nanophysics and Applications, Springer Berlin Heidelberg, Berlin, Heidelberg, 2010. https://doi.org/10.1007/978-3-642-13884-3.

[20] F. Alnjiman, ZnSnN2 thin films for photovoltaic applications, (n.d.) 140.

[21] A. Gastélum-Barrios, G.M. Soto-Zarazúa, A. Escamilla-García, M. Toledano-Ayala, G. Macías-Bobadilla, D. Jauregui-Vazquez, Optical Methods Based on Ultraviolet, Visible, and Near-Infrared Spectra to Estimate Fat and Protein in Raw Milk: A Review, Sensors. 20 (2020) 3356. https://doi.org/10.3390/s20123356.

[22] P. Makuła, M. Pacia, W. Macyk, How To Correctly Determine the Band Gap Energy of Modified Semiconductor Photocatalysts Based on UV–Vis Spectra, J. Phys. Chem. Lett. 9 (2018) 6814–6817. https://doi.org/10.1021/acs.jpclett.8b02892.

[23] S. Eaton-Magana, C.M. Breeding, An Introduction to Photoluminescence Spectroscopy for Diamond and its Applications in Gemology, Gems Gemol. 52 (2016) 2–17. https://doi.org/10.5741/GEMS.52.1.2.

[24] L. Museur, A. Kanaev, Near band gap photoluminescence properties of hexagonal boron nitride, J. Appl. Phys. (2008) 1.

Chapter 3

Blue emission and twins structure of p-type copper iodide thin films

Graphical Abstract

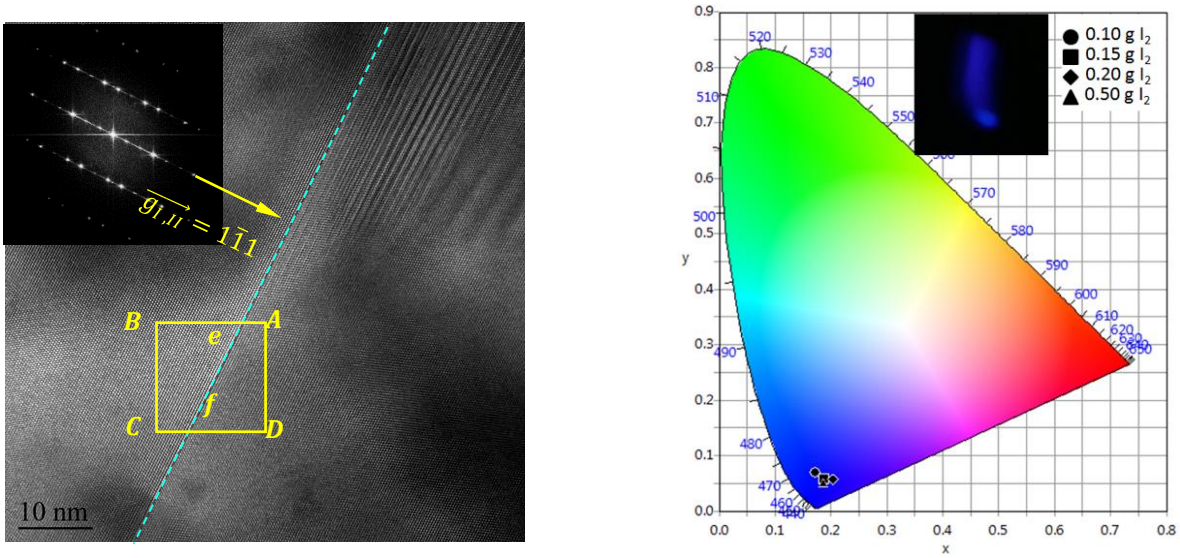

HRTEM micrograph of two twin-related variants with fast Fourier transform (FFT) is shown in the inset and CIE chromaticity diagram coordinates of samples with photo of blue emission from one sample under UV excitation is shown in the inset.

Abstract

Copper iodide is an attractive p-type transparent material suitable for optoelectronic applications. This work reports on the synthesis of copper iodide (CuI) by iodination of sputtered Cu films previously deposited on glass and silicon substrates. The crystalline phase and surface morphology were studied by X-ray diffraction (XRD) and scanning electron microscopy (SEM), respectively. The prepared CuI films crystallize in the zinc blende structure (γ-phase) at different amounts of iodine and exhibit preferential orientation along the <111> direction. Moreover, detailed investigation of the microstructure via high-resolution transmission electron microscopy (HR-TEM) revealed the presence and details of alternating twin crystallographic domains between adjacent grains. The electrical properties of the CuI films were characterized by Hall effect measurements and revealed a p-type carrier behavior for all films. The electrical behavior was discussed and attributed to the change in intrinsic point defects. In addition, the electronic bandgap and luminescence properties were investigated using optical transmission and photoluminescence (PL). The CuI films showed a wide band gap (about 3.05 eV) with an average transmittance of about (66 %) in the visible region. Moreover, the PL showed a blue emission ranging from 400 to 440 nm originating from the excitonic recombination and radiative point defects. The results presented in this chapter have been published in the following reference: O. Madkhali et al., *Blue emission and twin structure of p-type copper iodide thin films*, Surfaces and Interfaces 27 (2021) 101500.

Contents

3.1 Introduction.....
3.2 About the growth conditions .....
3.3 Influence of the amount of iodine on the structure and the properties of CuI thin films.....
3.3.1 Structure and composition of CuI films.....
3.3.2 Microstructure of □-CuI thin films.....
3.3.3 Optical transmission and absorption.....
3.3.4 Electrical properties .....
3.3.5 Photoluminescence .....
3.4 Conclusion.....

3.1 Introduction

Copper iodide (CuI) is considered as wide (about 3.1 eV) [1–6] and direct bandgap material with high exciton binding energy of about 62 meV [1,7]. This wide bandgap and high exciton binding energy are promising features for UV-blue emitting devices with high quantum efficiency [8] with possible operation at room temperature. Moreover, it exhibits intrinsic conductivity of p-type charge carriers. It is worth mentioning that the intrinsic optical and electrical properties of CuI are based on point defect chemistry. Thus, the p-type conductivity of CuI is due to the dominance of Cu-vacancy defects because of their low energy formation [1,9]. In contrast, formation of I-defects leads to the generation of a donor level which can compensate for the acceptors generated by Cu defects. Therefore, the control of defect chemistry in CuI is of great importance. This is considered as a practical way to tune and adjust the electrical response of the CuI. In this line, photoluminescence (PL) is a non-destructive and efficient tool that helps to identify and understand the role of such defects. Thanks to the inclusion of these point defects in the radiative recombinations, PL measurements not only lead to identification of the nature of the defects, but also provide information about the emission colour properties of the material.

Various techniques such as thermal evaporation [9], sputtering [10], mister atomizer [11], ionization [12], sputtering with excess iodine[13], and pulsed laser deposition[14] have been used to prepare CuI thin films. However, depending on the synthesis method, CuI films exhibit a wide range of properties, such as in figure of merit (FOM), which ranges from 350 [12] to 17000 $M\Omega^{-1}$ [13]. Among these thin film growth methods, thermal evaporation and sputtering are simpler and provide acceptable results compared to alternative methods. Compared to all these techniques, a two-step process including the deposition of a copper thin film and its iodination is simpler. Indeed, such a two-step process avoids to introduce gaseous iodine into vacuum chambers that may

contaminate the deposition chamber walls for the elaboration other kind of coatings (metals, nitrides…). It also allows better control in terms of thickness, process duration, and iodine addition amount.

In this chapter, we have focused our work on the deep structural, optical, and electrical studies to better understand the functional properties of CuI. HRTEM has been used to explore in details the structure of the prepared films at the nanoscale. Electrical characterizations were also performed to investigate the electrical conductivity and mobility of the films. PL spectroscopy was used to characterize the luminescence contributions of the point defects.

3.2 About the growth conditions

During this work several attempts to deposit high quality of CuI thin films have been performed. Within the first trials, guided by literature, different deposition conditions have been tested. We have synthesized three main series of samples to study the influence of the iodination duration, of the iodination temperature and of the amount of iodine (see appendix A). For each of these series, the structural, electrical and optical characterizations have been performed. After screening the relevant properties of the three series, it was found that the amount of iodine related series offers better control of the film stoichiometry as well as coherent and understandable functional properties. Thus, in the next sections, we deal with the growth of CuI thin films synthesized at different amounts of iodine by fixing the iodination duration at 60 min and the temperature at 75 °C.

3.3 Influence of the amount of iodine on the structure and the properties of CuI thin films

3.3.1 Structure and composition of CuI films

The X-ray diffractogram of the deposited copper film is shown in Figure 3.1. The (111) and (200) crystallographic planes of this fcc material can be clearly seen and the metallic Cu films have been grown with a preferred orientation along the [111] direction. The X-ray diffractograms of iodinated films obtained with different amounts of iodine on silicon substrate are also shown in Figure 3.1a. Regardless the amount of I_2, the iodinated films are highly crystallized. The same conclusion can be drawn when glass substrates (Figure 3.1b) are used. The position of the diffraction peaks fits well with the γ-CuI structure in agreement with the phase diagram of this material. The X-ray diffractogram of CuI films exhibits peaks corresponding to the (111), (200), (220) and (311) diffraction planes of the zinc blende structure at about 25, 30, 42 and 50°, respectively [1,3,15–21]. Since no metallic copper diffraction peak is detectable after the iodination step, the 50-nm thick sputtered Cu films are completely iodinated after the reaction at 75 °C for 60 minutes. Since the intensity of the (111) diffraction is very high compared to the other peaks, the CuI films show a preferential orientation along the [111] direction. This preferred orientation is similar to that observed on the metallic Cu film. However, the relative intensity of the (200) planes is lower for the copper iodide film suggesting that the preferred orientation of the CuI film may originate both from the preferred orientation of the metallic Cu film and from the peculiarities of iodine diffusion. For films deposited on silicon substrates, the lattice parameter derived from the (111) peak position is a = 0.6048 ± 0.0073 nm. This experimental value is close to the theoretical one (a = 0.6054 nm) [1]. The average coherence length was determined using Scherrer's formula ($\tau = \frac{K.\lambda}{\beta.\cos(\theta)}$). Where τ is the coherence length, K is a dimensionless shape factor, β is the peak broadening at half-

maximum intensity (FWHM) and θ is the Bragg angle. For the different values of iodine mass, the coherence length is ranging between 53 and 67 nm ± 7 nm, while for the deposited copper the coherence length is about 35 ± 4 nm. This twofold size increase has to be compared with that expected from the volume expansion is 4.7 (see section 3.3.2.). Such difference may come from the introduction of defects into the CuI grain that limit the coherence length.

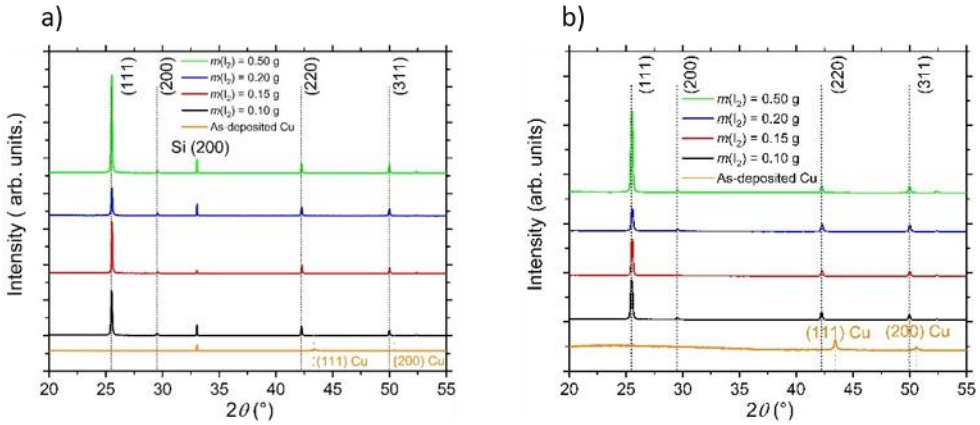

Figure 3.1: Series of X -ray diffractograms of CuI films synthesized with different amounts of iodine and as-deposited Cu film. The vertical dashed lines correspond to the theoretical positions of γ-CuI (black) and Cu (orange) diffraction peaks. a) silicon substrate and b) glass substrate

In a first step, the film composition has been measured using EDS. The I concentration increases with the increase of the I_2 amount (Figure 3.2) but it is still lower than 50 at. %. A second method has also been used to check the film composition: electron probe microanalysis. Only one sample has been characterized by EPMA (0.15 g I_2). This films has the following composition: 52.8 at. % for I and 47.2 at. % for Cu.. From these values, the atomic I/Cu ratio is about 1.12, suggesting an iodine over stoichiometry and then the occurrence of copper vacancies. EPMA results differ from those obtained by EDS where a copper overstoichiometry was suggested. In our opinion, the difference may come from the use of standards in EPMA that should improve the accuracy of the

measurement. Thus, in the next sections, we will consider that the CuI films are iodine overstoichiometric (as deduced from EPMA) and that the increase of the I_2 amount induces a relative increase of the iodine concentration (as deduced from EDS). Although the increase of the iodine amount does not markedly influence the CuI film composition, an increase of the CuI (111) diffraction peak was noticed. These results may suggest that the increase of the iodine amount induce an increase of the iodine concentration that favors the CuI film crystallinity.

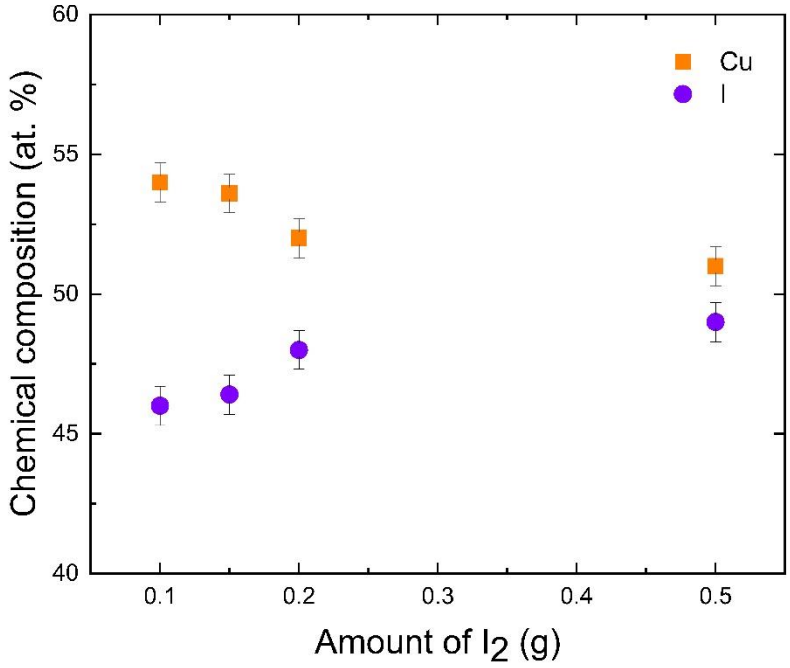

Figure 3.2: Composition of CuI films by EDS

3.3.2 Microstructure of γ-CuI thin films

The cross section of a CuI layer is shown in Figure 3.3a. Compared to the deposited Cu films, this SEM image clearly shows that the film surface is no longer smooth. Moreover, no porosity can be seen on this fracture image. The thickness estimated from this image is about 300 nm. As-deposited

copper films have a thickness of 50 nm. Since the ratio between the molar volume of CuI (33.39 $cm^3\ mol^{-1}$) and that of copper (7.11 $cm^3\ mol^{-1}$) is 4.7, the thickness measured by SEM (300 nm) is close to that expected (235 nm). This result also confirms that the iodination reaction is complete. In Figure 3.3b, the surface morphology of the films shows that they are composed of flat and contiguous equiaxed crystals for sample papered at 0.15 g (for the other samples see appendix B). Some porosities, which could not be detected in the cross section, can be observed on the surface image. The film morphology is independent of the nature of the substrate. A magnification of the surface of a film obtained on a glass substrate is shown in Figure 3.3c. Again, large grains and porosities can be observed. Such porosities may explain the difference between the expected and measured film thickness. The average grain size derived from Figure 3.3c and estimated using the ImageJ software is 2 nm. This value is very high compared to the value estimated by the Scherrer formula, and we will elaborate in the following on the origin of this difference. An interesting point is the appearance of some straight lines on the copper iodide grains. Such behavior has already been observed in the literature[1,22] but there is no clear description of the meaning of such lines. In order to obtain relevant information about these lines, the films were characterized by transmission electron microscopy after FIB preparation.

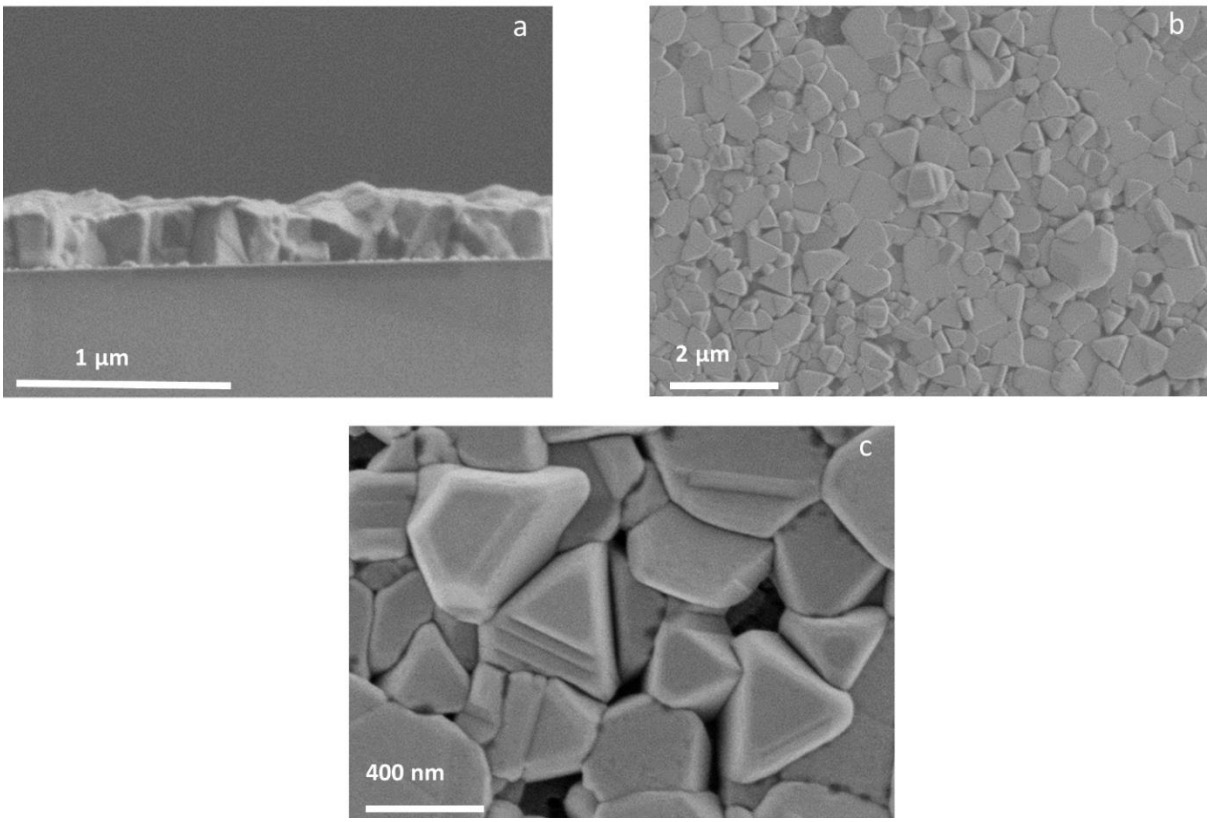

Figure 3.3: a) SEM cross section of a film prepared with 0.15 g I_2 deposited on silicon substrate. b) SEM surface image of the same film and c) surface magnification of a film prepared on a glass substrate with the same amount of iodine.

Although copper iodide thin films have been widely studied in the literature, there are few works that provide a detailed characterization of CuI by TEM [23]. This may be due to the fact that CuI film reduces into copper under the electron beam. To avoid such decomposition, TEM characterization should be carried out at the temperature of liquid nitrogen. Under this condition, the decomposition of CuI is inhibited. Figure 3.4a shows a TEM cross-sectional view of a CuI thin film. The film thickness is consistent with that previously measured using SEM cross section. Interestingly, no porosities can be seen in the analysed film cross section, indicating that density of such porosities is rather low. The CuI film contains large grains with a length of several hundred

nanometers on the film surface. Electron diffraction confirms that the film crystallizes in the γ-CuI structure with a lattice parameter a = 0.615 nm Figure 3.4b.

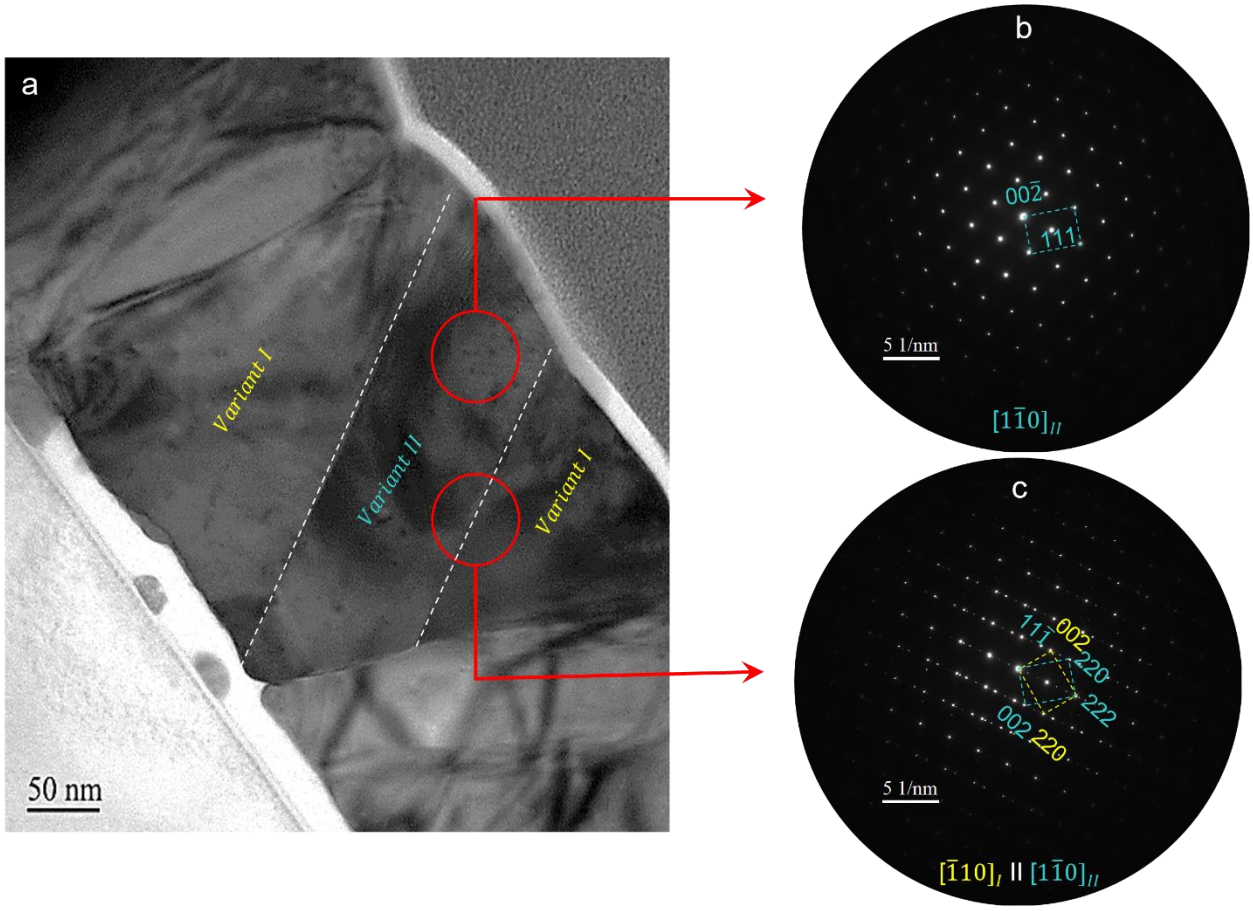

Figure 3.4: a) Bright field TEM micrograph showing twin related variants of thin CuI film (300 nm thick) deposited on silicon substrate. b) Corresponding electron diffraction pattern recorded along $[1\bar{1}0]_{II}$ *zone axis. c) Composite electron diffraction pattern recorded along* $[\bar{1}10]_I \parallel [1\bar{1}0]_{II}$ *zone axes (the scale of figures 3.4b and 3.4c differ)*

In Figure 3.3c, straight lines can be seen on the grain surface. Such lines can also be seen on the TEM cross-section Figure 3.4a. These lines, which pass through the entire layer thickness and reach the film surface are suspected of being to twins. Detailed TEM and electron diffraction analysis revealed that these very thin lines are the traces of the twinning planes separating two contiguous variants. The latter are twin-related as indicated by the composite selected area

diffraction pattern (SAED), recorded along $[10\bar{1}]_I // [\bar{1}01]_{II}$. Trace analysis supported by the bright field TEM micrograph Figure 3.4a and the corresponding diffraction patterns Figure 3.4b and 3.4c indicate that the twinning plane is (111). This twinning plane is expected as the γ-CuI crystallises in the FCC structure. The twinning (111) planes can be also understood according to Yang et al., where the Wulff shapes of CuI fcc crystals had been simulated and demonstrated for reactively sputtered CuI films [24]

One can notice, on the diffraction pattern, diffusion lines running parallel to [111] direction and crossing the (002) and $(11\bar{1})$ reflections, belonging to type I and type II, respectively. This diffusion lines are perpendicular to the trace of the (111) twinning plane. This situation is further a practical way to identify the (111) twinning plane. The bright Figure 3.4a and dark field Figure 3.5a, b, and c images highlight the twinning plane separating the alternating twin-related variants following the sequence: I, II, I.

Figure 3.5 shows TEM dark fields images, showing twinned variants of a thin CuI film deposited on a silicon substrate. TEM dark field images taken with $\vec{g}_I = (002)$ and $\vec{g}_{II} = (11\bar{1})$, respectively, highlight prominence of two twin-related variants, labelled I and II Figures 3.5a and 3.5b. The twin variant of type II is bordered on its most elongated parallel sides by two twin-variants of the type I Figure 3.5c.

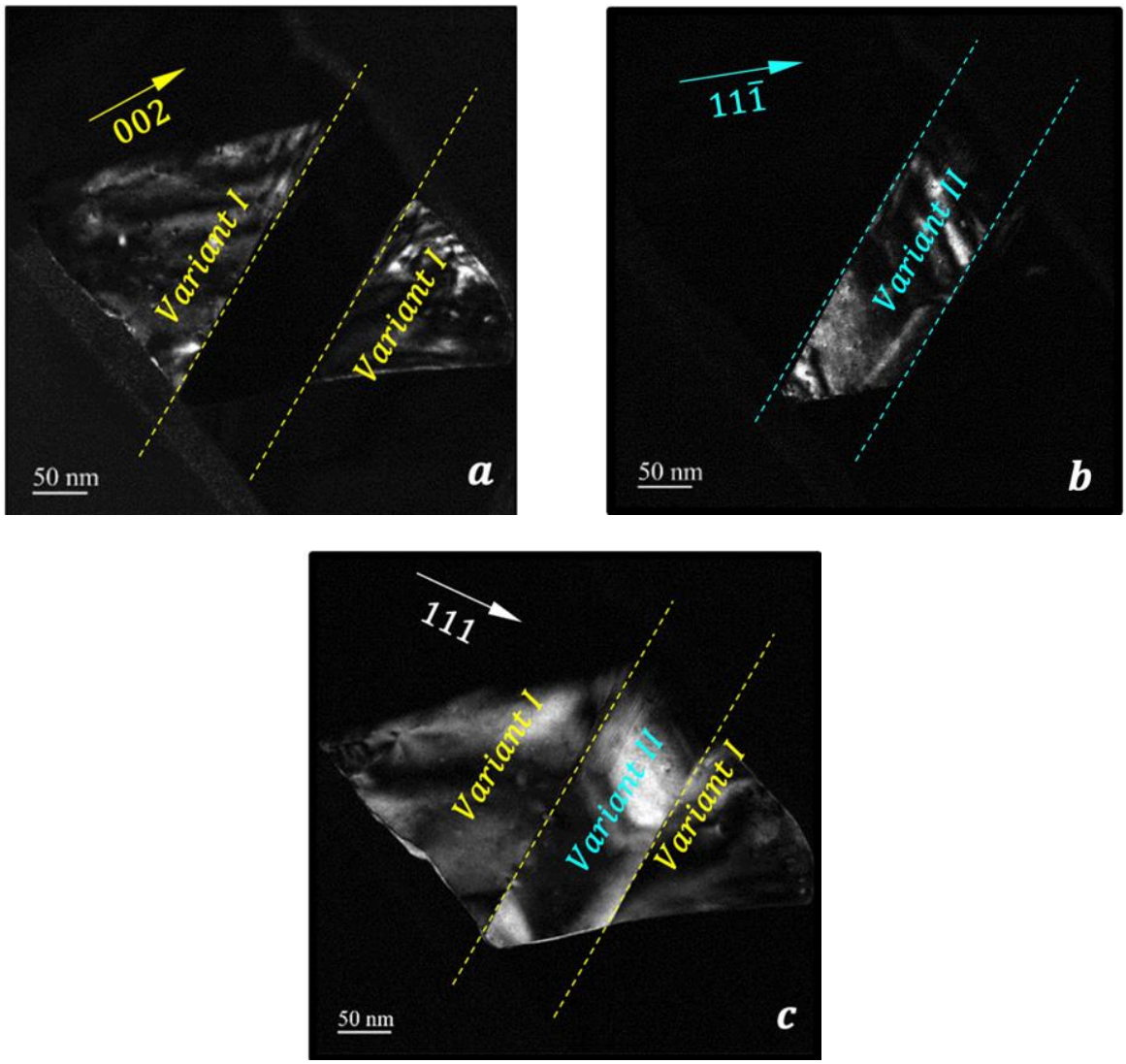

Figure 3.5: Series of dark field TEM images recorded with a) $\vec{g}_I = (002)$, b), $\vec{g}_{II} = (11\bar{1})$ and c) $\vec{g}_{I,II} = (11\bar{1})$, revealing two twin-related variants (I and II). One can notice that $(1\bar{1}1)$ is common to the two twin-related variants, is perpendicular to the twin plane.

STEM analyses were performed on the same area to localize iodine atoms in the thin film Figure 3.6. Along the analytical line, the iodine and copper concentrations are almost constant. The inset fast Fourier transform (FFT) and the corresponding high-resolution images indicate planes with their *d*-spacings of 0.35 nm and 0.31 nm, corresponding to the d_{111} and d_{200} of the γ-CuI phase, respectively.

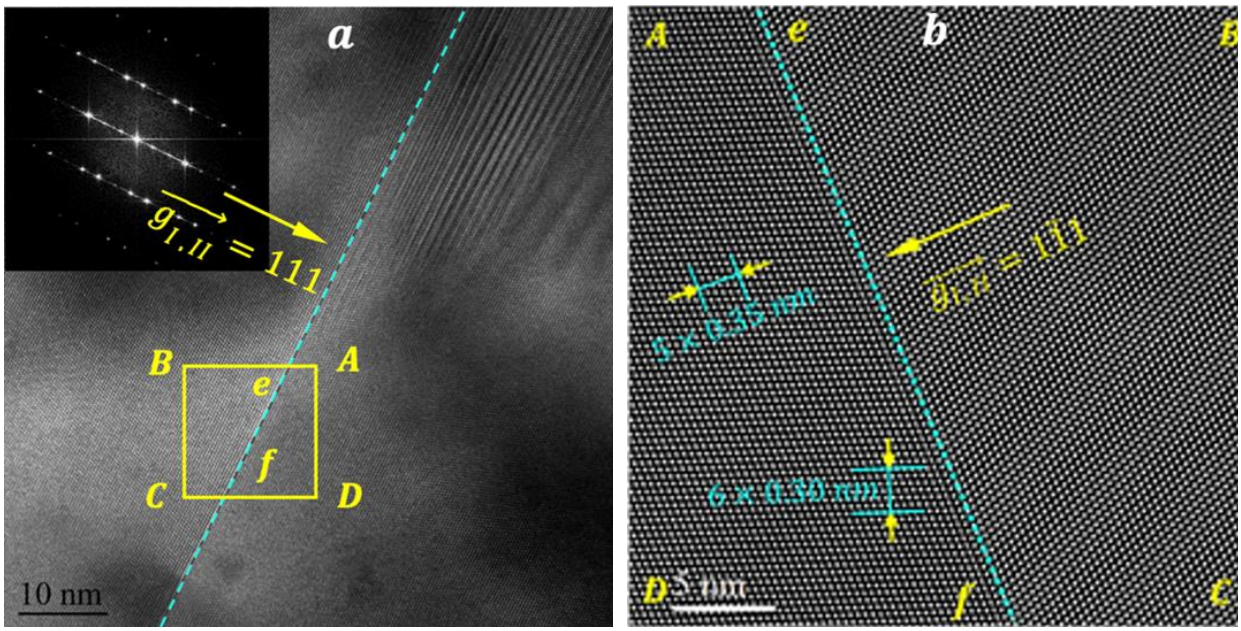

Figure 3.6: a) HRTEM micrograph recorded along [011] exhibiting two twin-related variants with, in the inset, the corresponding Fast Fourier Transform (FFT). b) STEM micrograph recorded along the same $[\bar{1}10]_I \parallel [1\bar{1}0]_{II}$ *zone axis and same area of interest exhibiting the twin plane separating the two twin-related variants. One can notice in Figure 3.6a, in addition to the twin-plane, stacking faults in the variant at right.*

3.3.3 Optical transmission and absorption

The transmittance and absorption coefficient (α) of the γ-CuI film synthesized with different amounts of iodine are shown in Figure 3.7a. As can be seen from this figure, a mean transmittance of 66 % is obtained in the 400-800 nm range when a mass of 0.5 g of iodine was used. Such transmittance value is close to the reported values [10,13]. It can be observed that the sample synthesized with 0.20 g of I_2 shows the lowest transmission value while the sample synthesized with 0.5 g of I_2 exhibit the highest one. This change in the transmission value can be correlated and understood from the crystallinity point of view. Sample with the lowest transmittance is characterized by the smaller crystallites size, approx. 50 nm, while the sample with the highest transmittance exhibits a coherence length of 65 nm. Hence, smaller crystallites size means high

density of the grain boundaries, which lead to scattering of more light and eventually low optical transmission is obtained. A strong absorption is observed at a wavelength close to 400 nm, which corresponds to the band gap of the film. This parameter was determined by the Tauc method, taking into account that γ-CuI is a direct semiconductor shown in Figure 3.7c. Under our synthesis conditions, the optical band gap is estimated around 3.01 eV, which is agreement with literature [1–4,6,23,25]and the theoretical value of 3.203 eV[5] obtained using the PBE0 calculation method[26]. Figure 3.7b shows the evolution of the absorption coefficient as a function of wavelength. The shape of this curve is typical of γ-CuI , showing two maxima : one at 337 nm (3.68 eV) and the second one at 407 nm (3.04 eV). This behaviour is attributed to the onset of the optical band gap of CuI. It has been reported that the origin of these two peaks are the direct optical transitions at the Γ point, called $Z_{1,2}$ and Z_3, respectively [27].

Indeed, the first peak $(Z_{1,2})$ consists essentially of a doublet structure corresponding to heavy-hole (HH) and light-hole (LH)excitons, as reported in [27]. On the other hand, the later peak (Z_3) is assigned to the split-off-hole exciton. It is worth noting that the splitting of energy between the HH and LH is evident at low temperature due to the localization of charge carrier motion. However, careful focus on the $Z_{1,2}$ peak in the present study reveals an asymmetry of the peak maximum that can be attributed to the low splitting energy between the HH and LH at room temperature. This is consistent with the view of Kim *et al.* [27] who showed that this splitting energy decreases with the increase in the temperature.

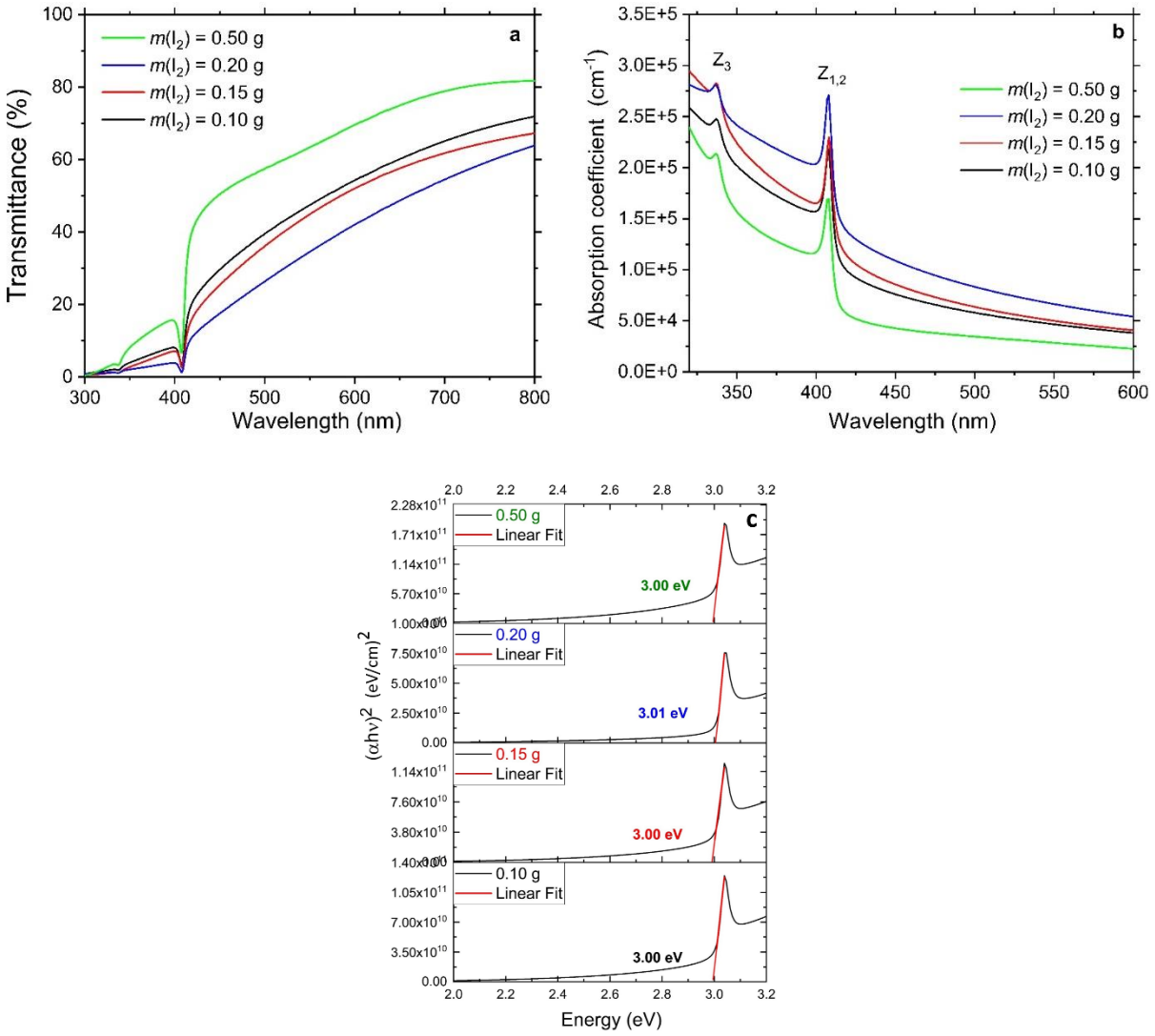

Figure 3.7: a) Transmission spectra of the CuI thin films synthesized with different amounts of iodine. b) Absorption coefficient evolution as a function of the wavelength.c) Tauc plot of all samples.

3.3.4 Electrical properties

The conductivity, charge carrier density and mobility of CuI films are presented in Table 3.1. They were derived from Hall effect measurements using van der Pauw geometry. Regardless the amount of iodine, the films show p-type behavior. At room temperature, the conductivity (σ) of the CuI thin films ranges from 19.6 to 47.4 S cm^{-1}. Despite the presence of defects deduced from XRD analyses and observed by TEM characterization, the electrical conductivity of CuI films

is higher than the reported values [2,11,12]. An optimum of the film conductivity is observed for 0.15 g of iodine. The obtained value of conductivity (47.4 S cm^{-1}) is very high compared to other p-type materials such as Cu_2O [28] or $CuCrO_2$ [29]. This result clearly confirms that CuI is a suitable material for p-type transparent conductive thin films. Therefore, as reported in reference, the reason for p-type conductivity is due to the occurrence of copper vacancies, resulting from their low formation energy compared with other copper iodide defects [1,5,13,30,31]. The mobility of holes in CuI thin films prepared at room temperature is higher than that of spiro-MeOTAD with 4×10^{-5} cm^2 V^{-1} s^{-1} [32] and that of CuSCN (0.1 cm^2 V^{-1} s^{-1}) [33]. Therefore, CuI thin films can serve as a strong hole transport layer for perovskite solar cells [34]. Recently, Yang *et al.* [13] reported an impressive conductivity of 283 S cm^{-1} for CuI thin films prepared by reactive sputtering in the presence of excess iodine. The hole density (p) ranges from 1.4×10^{18} to 4.3×10^{19} cm^{-3}.

Table 3.1 Electrical properties of the γ-CuI thin film

I_2 mass (g)	Resistivity (Ω cm)	Conductivity (S cm^{-1})	Mobility (cm^2 V^{-1} s^{-1})	Carrier concentration (cm^{-3})
0.10	4.1×10^{-2}	24.7	49.6	3.1×10^{18}
0.15	2.1×10^{-2}	47.4	6.9	4.3×10^{19}
0.20	3.1×10^{-2}	32.4	35.5	5.7×10^{18}
0.50	9.6×10^{-2}	10.4	45.9	1.4×10^{18}

The figure of merit (FOM) is defined as the ratio of the electrical conductivity to the absorption coefficient in the visible range. FOM is an important parameter that quantitatively describes the

performance of transparent conductive thin films. Neglecting the optical reflectance, the FOM of CuI thin films prepared with different amounts of iodine is shown in (Table 3.2) and compared with the results obtained by other techniques. The high value of FOM describes good performance of transparent conductive thin films. For transparent conductive materials, there is evidence in the literature that the figure of merit (FOM) can be used to compare the properties of the films. Within the iodine mass tested in the present study, the FOM ranges from 750 to 1900 $M\Omega^{-1}$ Figure 3.8.

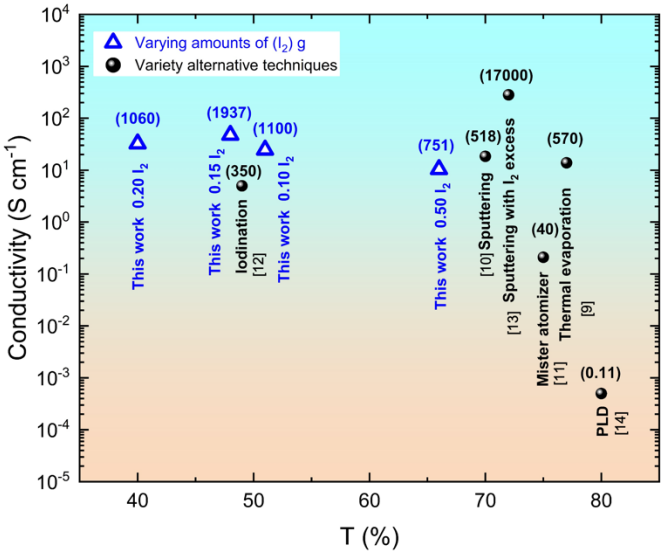

Figure 3.8: Evolution of electrical conductivity and averaged visible transmittances and the figure of merit of CuI films from the present work and from the literature.

Table 3.2: The figure of merit of γ-CuI thin films prepared by various techniques and in the present work.

Preparation method	Thickness (nm)	*T* (%)	Conductivity (S cm^{-1})	FOM ($M\Omega^{-1}$)	Ref.
PLD	500	80	5×10^{-4}	0.11	[14]
Mister atomizer	550	75	0.21	40	[11]
Iodination	500	49	5	350	[12]

Sputtering	100	70	18.5	518	[10]
Sputtering with I_2 excess	200	72	283	17000	[13]
Thermal evaporation	120	77	13.9	570	[9]
Sputtering + iodination	300	51	24.7	1100	Present work
Sputtering + iodination	300	48	47.4	1937	Present work
Sputtering + iodination	300	40	32.8	1060	Present work
Sputtering + iodination	300	66	10.4	751	Present work

3.3.5 Photoluminescence

Photoluminescence (PL) is a powerful technique that provides information about the optical behavior of the material under study, while the defect chemistry of γ-CuI plays an important role in its functionality [9,15,35]. Figure 3.9a shows the PL spectra of the prepared samples. The PL spectra of all samples have similar spectral features. It consists of two main bands around 413 nm (blue region) and 726 nm (red region). Moreover, the fine structure of the fundamental band in the blue region shows maximum at 413 nm (3 eV) and shoulder at slightly lower energy of 418 nm (2.96 eV). This shoulder became significant at I_2-excess conditions Figure 3.9b. Therefore, three PL spectral features can be considered: PL1, PL2 and PL3 at 413 nm (3 eV), 418 nm (2.96 eV) and 726 nm (1.7 eV), respectively. Similar PL peaks were reported by S. Koyasu *et al*. [36] and G. Lin *et al.* [22] for CuI Material. They attributed the origin of the PL1 peak to the electronic transition from the conduction band to the valence band, while the other peaks, PL2 and PL3, are attributed to different defect-related transitions. Tracing the behavior of these defect-related PL peaks reveals a significant contribution of the PL2 peak under I_2-excess conditions, in contrast to the PL3 peak, which becomes more evident under I_2-deficient conditions. This agrees with the work mentioned above. This also confirms the origin of PL2 and PL3 to Cu-vacancy and I-vacancy related transitions, respectively. In other words, the very small energy difference between PL1 and

PL2 indicates that Cu-vacancy forms a shallow acceptor level. This probably indicates the favorable conditions to increase the p-type conductivity. In contrast, the I-vacancy produces deep donor level. Thus, PL2 and PL3 can be assigned to the transition from conduction band to Cu vacancies and from I vacancies to valence band, respectively. As discussed above one can see the important role of the defect chemistry in CuI which, in turn, modifies its electronic structure. However, further optical studies on the samples of this study are required to understand and control the role of these defects, leading to the desired applications.

Furthermore, CuI shows strong blue emission inset in Figure 3.10, which can be exploited in various lightening applications. Moreover, the intrinsic p-type conductivity property opens the door to use CuI as a promising alternative to GaN-based light emitting devices. This may be an interesting approach, especially given the current technical difficulties in fabricating highly doped p-type GaN layers.

In this regard, the chromaticity diagram is used to verify the quality of the emission colors of the phosphor as well as to show its color coordinates in relation to the coordinates of the white light zone. The coordinates of the CIE chromaticity diagram corresponding to the four samples Figure 3.10 verifies their coordinates lies in the blue region with slight shifts depending on the amount of I_2. Therefore, the CuI phosphor can be used as a blue light supplier in a white light generation system. In line with this, Taehwan Jun *et al.* [37] recently reported the generation of white light emission within the Cs-Cu-I system.

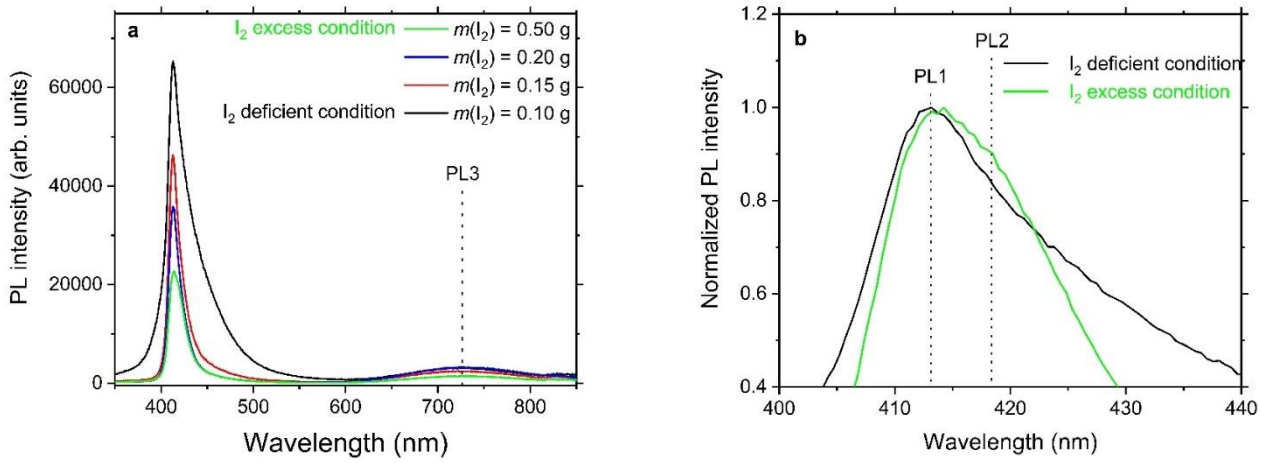

Figure 3.9: a) Photoluminescence spectra of the γ-CuI thin film with different amounts of iodine excited by 320 nm. b) magnification of the high energy peak to show the influence of the iodine amount on the shoulder at 418 nm.

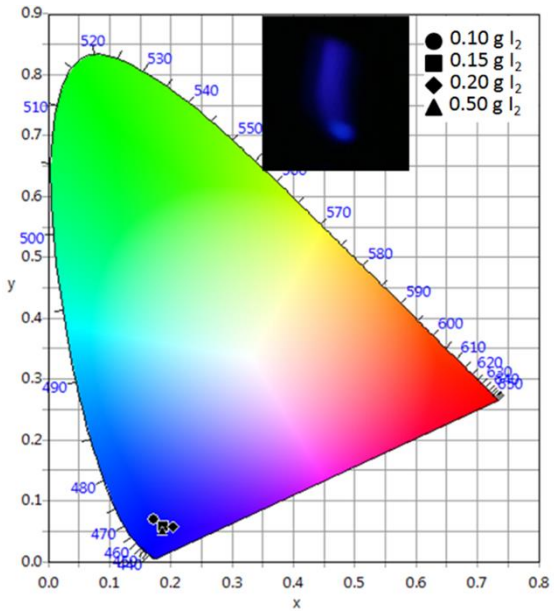

Figure 3.10: CIE chromaticity diagram coordinates of the four samples. The inset corresponds to a photo of the blue emission from one sample under UV-excitation

3.4 Conclusion

In this work, thin CuI films were fabricated to study the structure, microstructure, and functional properties using XRD, SEM, TEM, PL, UV-visible and Hall effect techniques. We obtained copper iodide films showing a strong preferential orientation in the [111] direction. The surface morphology of the films shows that they are composed of flat disoriented grains. The crystallographic twin domains in the CuI grains were analyzed by selected area electron diffraction (SAED), revealing the twin geometry. We synthesized a transparent conductive semiconductor with unique optoelectronic properties, including wide band gap of 3.01 eV. As a result, an average transmittance of 66 % in the visible region was achieved. The photoluminescence (PL) properties of these samples were then carefully evaluated. Consequently, three PL spectral features were obtained: PL1, PL2, and PL3 at 413 nm (3 eV), 418 nm (2.96 eV), and 726 nm (1.7 eV), respectively. CuI thin films were found to host blue light emission under 320 nm excitation. Using 0.2 g I_2, the as-prepared CuI film had an electrical conductivity of 30.8 S cm^{-1} and a mobility of 35.6 cm^2 V^{-1} s^{-1}. These results clearly indicate that γ-CuI is very promising as a transparent semiconductor. Therefore, transparent p-type CuI-based semiconductors are expected to stimulate the development of transparent electronics.

References

[1] M. Grundmann, F.-L. Schein, M. Lorenz, T. Böntgen, J. Lenzner, H. von Wenckstern, Cuprous iodide: A p-type transparent semiconductor, history, and novel applications: Cuprous iodide, Phys. Status Solidi A. (2013) n/a-n/a. https://doi.org/10.1002/pssa.201329349.

[2] N. Yamada, R. Ino, Y. Ninomiya, Truly Transparent p-Type γ-CuI Thin Films with High Hole Mobility, Chem. Mater. 28 (2016) 4971–4981. https://doi.org/10.1021/acs.chemmater.6b01358.

[3] B.M. Morais Faustino, D. Gomes, J. Faria, T. Juntunen, G. Gaspar, C. Bianchi, A. Almeida, A. Marques, I. Tittonen, I. Ferreira, CuI p-type thin films for highly transparent thermoelectric p-n modules, Sci. Rep. 8 (2018). https://doi.org/10.1038/s41598-018-25106-3.

[4] D. Chen, Y. Wang, Z. Lin, J. Huang, X. Chen, D. Pan, F. Huang, Growth Strategy and Physical Properties of the High Mobility P-Type CuI Crystal, Cryst. Growth Des. 10 (2010) 2057–2060. https://doi.org/10.1021/cg100270d.

[5] J. Wang, J. Li, S.-S. Li, Native *p* -type transparent conductive CuI via intrinsic defects, J. Appl. Phys. 110 (2011) 054907. https://doi.org/10.1063/1.3633220.

[6] C. Yang, D. Souchay, M. Kneiß, M. Bogner, H.M. Wei, M. Lorenz, O. Oeckler, G. Benstetter, Y.Q. Fu, M. Grundmann, Transparent flexible thermoelectric material based on non-toxic earth-abundant p-type copper iodide thin film, Nat. Commun. 8 (2017). https://doi.org/10.1038/ncomms16076.

[7] C. Yang, M. Kneiß, F.-L. Schein, M. Lorenz, M. Grundmann, Room-temperature Domain-epitaxy of Copper Iodide Thin Films for Transparent CuI/ZnO Heterojunctions with High Rectification Ratios Larger than 109, Sci. Rep. 6 (2016). https://doi.org/10.1038/srep21937.

[8] B. Zhao, L. Chen, W. Liu, L. Wu, Z. Lu, W. Cao, High efficiency blue light-emitting devices based on quantum dots with core-shell structure design and surface modification, RSC Adv. 11 (2021) 14047–14052. https://doi.org/10.1039/D0RA10173G.

[9] D.K. Kaushik, M. Selvaraj, S. Ramu, A. Subrahmanyam, Thermal evaporated Copper Iodide (CuI) thin films: A note on the disorder evaluated through the temperature dependent electrical properties, Sol. Energy Mater. Sol. Cells. 165 (2017) 52–58. https://doi.org/10.1016/j.solmat.2017.02.030.

[10] T. Tanaka, K. Kawabata, M. Hirose, Transparent, conductive CuI films prepared by rf-dc coupled magnetron sputtering, Thin Solid Films. 281–282 (1996) 179–181. https://doi.org/10.1016/0040-6090(96)08607-5.

[11] M.N. Amalina, Y. Azilawati, N.A. Rasheid, M. Rusop, The Properties of Copper (I) Iodide (CuI) Thin Films Prepared by Mister Atomizer at Different Doping Concentration, Procedia Eng. 56 (2013) 731–736. https://doi.org/10.1016/j.proeng.2013.03.186.

[12] F.-L. Schein, H. von Wenckstern, M. Grundmann, Transparent *p* -CuI/ *n* -ZnO heterojunction diodes, Appl. Phys. Lett. 102 (2013) 092109. https://doi.org/10.1063/1.4794532.

[13] C. Yang, M. Kneiβ, M. Lorenz, M. Grundmann, Room-temperature synthesized copper iodide thin film as degenerate p-type transparent conductor with a boosted figure of merit, Proc. Natl. Acad. Sci. 113 (2016) 12929–12933. https://doi.org/10.1073/pnas.1613643113.

[14] P.M. Sirimanne, M. Rusop, T. Shirata, T. Soga, T. Jimbo, Characterization of transparent conducting CuI thin films prepared by pulse laser deposition technique, Chem. Phys. Lett. 366 (2002) 485–489. https://doi.org/10.1016/S0009-2614(02)01590-7.

[15] Z. Zheng, A. Liu, S. Wang, B. Huang, K.W. Wong, X. Zhang, S.K. Hark, W.M. Lau, Growth of highly oriented (110) γ-CuI film with sharp exciton band, J. Mater. Chem. 18 (2008) 852. https://doi.org/10.1039/b719452h.

[16] M. Yashima, Q. Xu, A. Yoshiasa, S. Wada, Crystal structure, electron density and diffusion path of the fast-ion conductor copper iodide CuI, J. Mater. Chem. 16 (2006) 4393. https://doi.org/10.1039/b610127e.

[17] Y. Seguchi, T. Soejima, Facile vapor-phase synthesis of copper nanostructures on cuprous iodide films, Vacuum. 144 (2017) 53–62. https://doi.org/10.1016/j.vacuum.2017.07.017.

[18] M.R. Johan, K. Si-Wen, N. Hawari, N.A.K. Aznan, Synthesis and Characterization of Copper (I) Iodide Nanoparticles via Chemical Route, Int J Electrochem Sci. 7 (2012) 9.

[19] D.A. Keen, S. Hull, The high-temperature structural behaviour of copper(I) iodide, J. Phys. Condens. Matter. 7 (1995) 5793–5804. https://doi.org/10.1088/0953-8984/7/29/007.

[20] S. Hull, D.A. Keen, W. Hayes, N.J.G. Gardner, Superionic behaviour in copper (I) iodide at elevated pressures and temperatures, J. Phys. Condens. Matter. 10 (1998) 10941–10954. https://doi.org/10.1088/0953-8984/10/48/015.

[21] S. Hull, D.A. Keen, High-pressure polymorphism of the copper(I) halides: A neutron-diffraction study to ∼10 GPa, Phys. Rev. B. 50 (1994) 5868–5885. https://doi.org/10.1103/PhysRevB.50.5868.

[22] G. Lin, F. Zhao, Y. Zhao, D. Zhang, L. Yang, X. Xue, X. Wang, C. Qu, Q. Li, L. Zhang, Luminescence Properties and Mechanisms of CuI Thin Films Fabricated by Vapor Iodization of Copper Films, Materials. 9 (2016) 990. https://doi.org/10.3390/ma9120990.

[23] K. Zhao, G.O. Ngongang Ndjawa, L.K. Jagadamma, A.E. Labban, H. Hu, Q. Wang, R. Li, M. Abdelsamie, P.M. Beaujuge, A. Amassian, Highly efficient organic solar cells based on a robust room-temperature solution-processed copper iodide hole transporter, Nano Energy. 16 (2015) 458–469. https://doi.org/10.1016/j.nanoen.2015.07.018.

[24] C. Yang, E. Rose, W. Yu, T. Stralka, F. Geng, M. Lorenz, M. Grundmann, Controllable Growth of Copper Iodide for High-Mobility Thin Films and Self-Assembled Microcrystals, ACS Appl. Electron. Mater. 2 (2020) 3627–3632. https://doi.org/10.1021/acsaelm.0c00692.

[25] S.A. Mohamed, J. Gasiorowski, K. Hingerl, D.R.T. Zahn, M.C. Scharber, S.S.A. Obayya, M.K. El-Mansy, N.S. Sariciftci, D.A.M. Egbe, P. Stadler, CuI as versatile hole-selective contact for organic solar cell based on anthracene-containing PPE–PPV, Sol. Energy Mater. Sol. Cells. 143 (2015) 369–374. https://doi.org/10.1016/j.solmat.2015.07.003.

[26] C. Adamo, V. Barone, Toward reliable density functional methods without adjustable parameters: The PBE0 model, J. Chem. Phys. 110 (1999) 6158–6170. https://doi.org/10.1063/1.478522.

[27] D. Kim, M. Nakayama, O. Kojima, I. Tanaka, H. Ichida, T. Nakanishi, H. Nishimura, Thermal-strain-induced splitting of heavy- and light-hole exciton energies in CuI thin films grown by vacuum evaporation, Phys. Rev. B. 60 (1999) 13879–13884. https://doi.org/10.1103/PhysRevB.60.13879.

[28] Y. Wang, P. Miska, D. Pilloud, D. Horwat, F. Mücklich, J.F. Pierson, Transmittance enhancement and optical band gap widening of Cu_2O thin films after air annealing, J. Appl. Phys. 115 (2014) 073505. https://doi.org/10.1063/1.4865957.

[29] H. Sun, M. Arab Pour Yazdi, P. Briois, J.-F. Pierson, F. Sanchette, A. Billard, Towards delafossite structure of Cu–Cr–O thin films deposited by reactive magnetron sputtering: Influence of substrate temperature on optoelectronics properties, Vacuum. 114 (2015) 101–107. https://doi.org/10.1016/j.vacuum.2015.01.009.

[30] K.K. Chinnakutti, V. Panneerselvam, D. Govindarajan, A. kumar Soman, K. Parasuraman, S. Thankaraj Salammal, Optoelectronic and electrochemical behaviour of γ-CuI thin films prepared by solid iodination process, Prog. Nat. Sci. Mater. Int. 29 (2019) 533–540. https://doi.org/10.1016/j.pnsc.2019.09.005.

[31] M. Graužinytė, S. Botti, M.A.L. Marques, S. Goedecker, J.A. Flores-Livas, Computational acceleration of prospective dopant discovery in cuprous iodide, Phys. Chem. Chem. Phys. 21 (2019) 18839–18849. https://doi.org/10.1039/C9CP02711D.

[32] T. Leijtens, I.-K. Ding, T. Giovenzana, J.T. Bloking, M.D. McGehee, A. Sellinger, Hole Transport Materials with Low Glass Transition Temperatures and High Solubility for Application in Solid-State Dye-Sensitized Solar Cells, ACS Nano. 6 (2012) 1455–1462. https://doi.org/10.1021/nn204296b.

[33] P. Pattanasattayavong, N. Yaacobi-Gross, K. Zhao, G.O.N. Ndjawa, J. Li, F. Yan, B.C. O'Regan, A. Amassian, T.D. Anthopoulos, Hole-Transporting Transistors and Circuits Based on the Transparent Inorganic Semiconductor Copper(I) Thiocyanate (CuSCN) Processed from Solution at Room Temperature, Adv. Mater. 25 (2013) 1504–1509. https://doi.org/10.1002/adma.201202758.

[34] J.A. Christians, R.C.M. Fung, P.V. Kamat, An Inorganic Hole Conductor for Organo-Lead Halide Perovskite Solar Cells. Improved Hole Conductivity with Copper Iodide, J. Am. Chem. Soc. 136 (2014) 758–764. https://doi.org/10.1021/ja411014k.

[35] A.N. Gruzintsev, W.N. Zagorodnev, Effect of annealing on the luminescence of p-CuI crystals, Semiconductors. 46 (2012) 149–154. https://doi.org/10.1134/S1063782612020133.

[36] S. Koyasu, N. Umezawa, A. Yamaguchi, M. Miyauchi, Optical properties of single crystalline copper iodide with native defects: Experimental and density functional theoretical investigation, J. Appl. Phys. 125 (2019) 115101. https://doi.org/10.1063/1.5082865.

[37] T. Jun, T. Handa, K. Sim, S. Iimura, M. Sasase, J. Kim, Y. Kanemitsu, H. Hosono, One-step solution synthesis of white-light-emitting films via dimensionality control of the Cs–Cu–I system, APL Mater. 7 (2019) 111113. https://doi.org/10.1063/1.5127300.

Chapter 4

Tuning the photoluminescence response and control of the electrical carrier type of (Ag, Cu)I thin films

Graphical Abstract

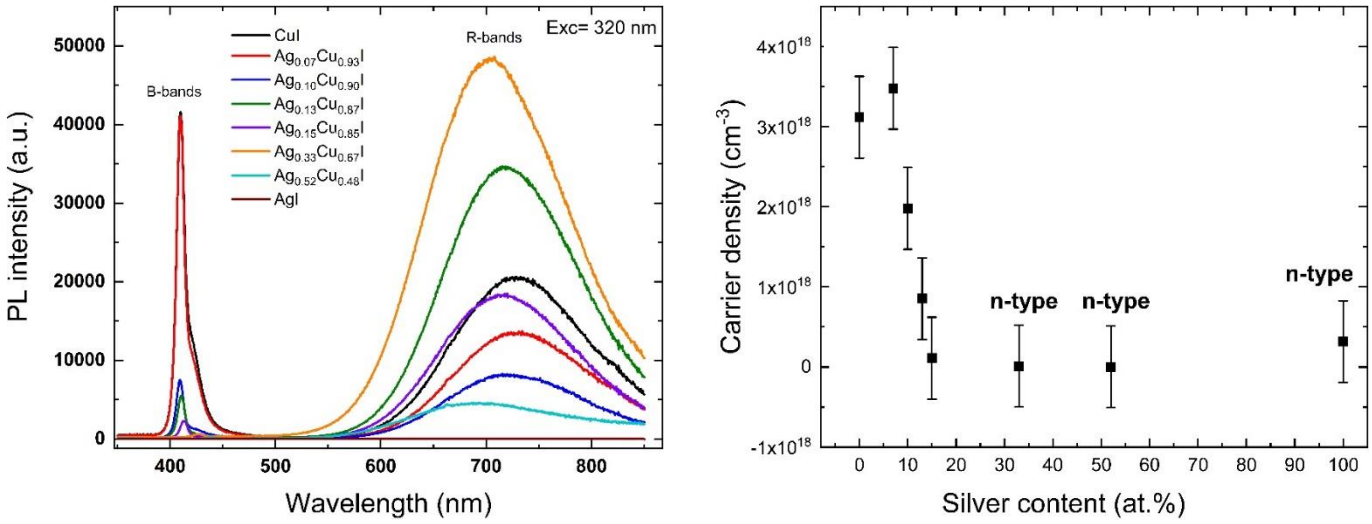

Photoluminescence (PL) spectra and carrier density measured for (Ag,Cu)I film samples

Abstract

This work reports on structural, optical and electrical characterization of (Ag,Cu)I thin films prepared by iodination of co-sputtered Ag-Cu layers. The crystalline structure of the prepared films was investigated by X-ray diffraction (XRD). The film morphology was studied by scanning electron microscopy (SEM). The electrical properties of (Ag,Cu)I films were characterized by Hall effect measurements. Depending on the silver content, the films exhibit either a p-type or a n-type behaviour. The electrical behaviour was discussed and attributed to the change in the intrinsic point defects. The optical properties were examined by optical transmission and photoluminescence (PL). It was found that the film crystallinity and morphology were modified due to the change in the Ag concentration $Ag_xCu_{1-x}I$ ($0 \leq x \leq 0.52$). In addition, the PL results showed a tendency of the PL spectral features of CuI to be changed to those of AgI with the increase of the silver content. A correlation between the optical and electrical results was established and evidenced the origin of the electrical behaviour. It is proposed that presence of Ag in (Ag,Cu)I thin films promotes the formation of iodine vacancies, which act as donor type defect, and eventually, with increasing the Ag content, crossover the carriers from p-type to n-type occurs. The interaction of such donor defect with the intrinsic acceptor defect, represented by Cu-vacancies, governs the functional properties, in particular the optical and electrical, of the material. These findings can pave the way of developing well-controlled (Ag,Cu)I-based devices.

Contents

4.1 Introduction.....

4.2 Composition and (micro)structural characterizations.....

4.2.1 Film composition and structure .....

4.2.2 Film morphology .....

4.2.3 Photoluminescence (PL).....

4.2.4 Optical properties of (Ag,Cu)I films.....

4.2.5 Electrical properties of (Ag,Cu)I thin films.....

4.3 Conclusion.....

4.1 Introduction

As discussed in the chapter I, halide compounds exhibit a competitive optoelectrical properties compared to semiconducting metal oxides [1]. Halide perovskite materials have been studied as strong candidates for the light-absorbing layers in high-efficiency photovoltaics [2]. Transparent conductors have gained widespread attention for their display panel and solar cell applications, including light emitting and light utilization devices [3]. Particularly, Agl and Cul transparent semiconductors are suitable to form heterojunctions exhibiting a diode behavior [1]. The electrical properties of these materials being tuneable, they have been already used in electronic components like light-emitting devices, resistance-changing layer of resistive random-access memory (ReRAM) and light-sensing layer of photodetectors [4]. Further studies are needed to assess the electrical and chemical properties of ternary metal halide, i.e. solid solution, for superior electronic component and device design.

Silver copper iodide is considered as a transparent conductive material (TCM) [1,5]. Silver iodide (AgI) and copper iodide (CuI) are both semiconductors with wide direct band gaps of 2.8 eV [6–9] and 3.1 eV [5,10–12], respectively. AgI exhibits a n-type semiconducting behaviour, while CuI is a p-type semiconductor. AgI, valued for its ionic conductivity and photosensitivity, finds its use in solid-state electrolytes, photographic films and photocatalysts [13]. CuI has a high hole mobility up to 43.9 $cm^2 V^{-1} s^{-1}$ [5,14] setting off from copper vacancies [5]. Silver iodide crystallizes in three structures: the body-centred cubic α-phase, the hexagonal wurtzite-like β–phase, and the cubic zincblende-like γ one [15]. A mixture of the β– and γ–phases is found at ambient temperatures [16], while the α–phase is stable at temperatures above 420 K [17]. The α-AgI shows very high ionic conductivity and, thus, it is named the “superionic” phase [16]. Copper iodide also crystallizes in three phases under atmospheric pressure: α, β and γ phases [5]. The α–phase, that

crystallizes in a rocksalt-like structure, is stable at temperatures higher than 673 K, whereas between 643 and 673 K, copper iodide crystallizes in a β wurtzite-like structure. Finally, the γ–phase crystallizes in a zinc blende-like structure (i.e. a face centred cubic (fcc) structure with the half of the tetrahedral positions occupied) is stable at temperatures lower than 643 K. These two types of semiconductors can be prepared by iodination of the metallic thin films, both being transparent.

Recent studies reported the electrical conductivity and phase transition behaviour at a nanoscale $Ag_xCu_{1-x}I$ ($0.1 < x < 1.0$) [18], in contrast with Kumar *et al.* [19] who emphasized only the Ag rich solid solution $Ag_xCu_{1-x}I$ ($0.75 < x < 1$). Recently, Annadi *et al.* [20] successfully synthesized $Ag_xCu_{1-x}I$ with $0 \leq x \leq 1$. Until now, the existing literature has primarily focused on structural phase formation and superionic conductivity in silver-copper-iodide materials [18,21].

In this chapter, we examine the structure, the morphology and the functional properties of (Ag,Cu)I thin films synthesized at room temperature using a two steps process. Magnetron sputtering was used to deposit a metallic film of copper and silver that was submitted to an iodination step using iodine vapor. Using this method, we synthesized a transparent conductive material with interesting optoelectronic properties. It is worth to mention that, due to the very high reactivity of iodine with Ag (see appendix C), it was decided to prepare these ternary samples at room temperature (RT) instead of at 75 °C, like in the previous chapter on CuI films. In addition, this method attempts to offer an equal opportunity for Cu and Ag to interact with I atoms and avoiding the application of any intentional effects, like temperature of the reaction, which might be favourable for one of them. The pure copper iodide films described in the present chapter were synthesized using different conditions than those presented in chapter 3 (temperature change). Thus, their properties differ with those of the previous chapter (especially for photoluminescence meausurements).

4.2 Composition and (micro)structural characterizations

4.2.1 Film composition and structure

As mentioned in the chapter 2, the Ag content in the as-deposited metallic films has been tuned by controlling the current applied on the Ag target (the copper target current being fixed at 0.3 A). Figure 4.1 shows the evolution of the Ag/(Ag+Cu) atomic ratio as a function of the current applied on the Ag target (this ratio was estimated from EDS measurements). Within the explored current range, a linear relation is evidenced. The increase of the current applied to the silver target induces a linear increase of the amount of sputtered atoms and then an increase of the silver content, as shown in Figure 4.1. These results clearly show the possibility to control the film composition by controlling the deposition parameters.

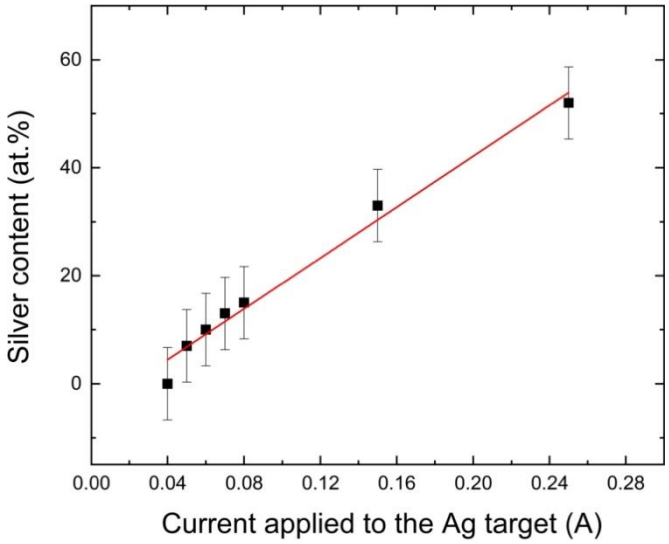

Figure 4.1: Evolution of silver content (at. %) as a function of the current applied to the silver target.

In addition, X-ray diffraction (XRD) has been performed to investigate the influence of Ag addition on the structure of as-deposited metallic AgCu samples Figure 4.2. The sputtering time

was fixed at 10 min and the obtained thickness increases with the silver content into the 250–450 nm range (Table 4.3). Both pure fcc Cu and fcc Ag films with lattice parameter a = 0.3617 and a = 0.4079 nm, respectively were also prepared as shown in Figure 4.2 and used as references. It can be observed that, the Ag_xCu_{1-x} ($0 < x < 0.15$) films crystallize in the same structure than the pure copper films. With the increase of silver content, (111) and (200) diffraction peaks -related to pure Cu- gradually degrade (suggesting a decrease of the crystallinity level) and shift towards low angle (suggesting a progressive substitution of copper atoms by silver ones in the fcc Cu phase). For higher silver contents $Ag_{0.33}Cu_{0.67}$ and $Ag_{0.52}Cu_{0.48}$, the diffractogram shows two broad peaks located at approximatively 39 and 42°. These peaks can be assigned to the (111) diffraction peaks of the fcc Ag and fcc Cu phases, respectively. These peaks are shifted to high angle values for the silver phase and to low angle values for the copper phase. These results clearly indicate that the films are biphased and that each phase is a metastable solid solution.

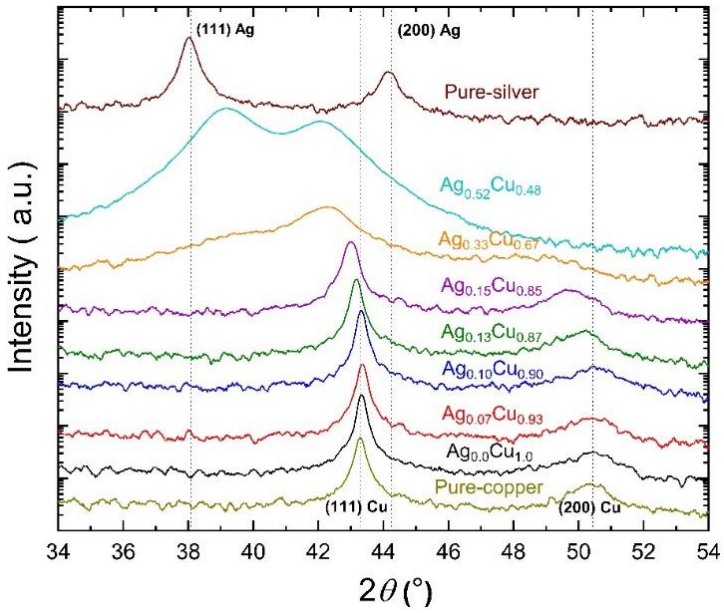

Figure 4.2: X-ray diffractograms (XRD) of as-deposited metallic AgCu films deposited at room temperature.

The metallic AgCu films have been iodinated at room temperature during 120 min. X-ray diffractograms of these iodinated films are presented in Figure 4.3. Whatever the silver content, no diffraction peak of the remaining metallic phase are detected, suggesting that the whole metallic films have reacted with iodine to form the iodide phase. This figure also shows the diffractogram of a pure copper iodide and pure silver iodide film (details about the characterization of AgI films are presented in Appendix D). As previously reported in chapter 3 for CuI films, (Ag,Cu)I ones grow with a strong preferred orientation along the [111] direction. When the silver concentration in $Ag_xCu_{1-x}I$ is in the 0 - 0.15 range, the addition of silver does not change the shape of the diffractogram. Films crystallize into the cubic γ-CuI structure (space group F-43m) (JCPDS#00-006-0246). Using a logarithm scale for the *y* axis, the characteristics planes ((111), (200), (220), (311), (222), and (400)) of γ-CuI phase are evidenced. Further increase of the silver content does not change the diffractogram shape. Although, a slight shift in the position of the diffraction peaks towards lower angle is detected, silver content does not strongly change the diffractogram shape. This shift can be attributed to the difference between Ag and Cu atomic radius (172 and 128 pm, respectively) which leads to lattice expansion when Ag content increases. Although the diffraction peaks of the cubic γ phase are shifted to lower angles, no peak from the hexagonal β-AgI lattice is evidenced [20]. Thus, within the silver composition range tested in this study (0 to 52 at. %), silver atoms substitute copper ones in the cubic γ-CuI phase.

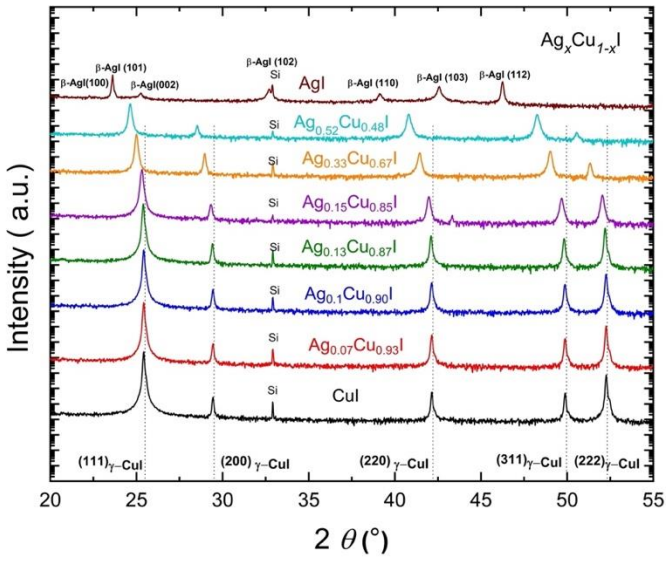

Figure 4.3: XRD of (Ag,Cu)I thin films obtained after 120 min iodination at room temperature.

The lattice expansion can also be observed by plotting the calculated cell parameter as a function of silver content in the grown films Figure 4.4. The linear behaviour, between the lattice parameter and Ag content, obeys Vegard's law and indicates the expansion process due to the substitution of copper atoms by silver ones. This leads to the change of the cubic γ-CuI phase (a = 6.05 Å) [5] towards the onset of the cubic AgI phase (a = 6.49 Å [22]) [20]. In this figure we have considered the cubic AgI phase instead of the hexagonal one to show that a total solid solution of CuI and AgI could be obtained. The mean coherence length was determined using the Scherrer's formula. We have noticed that an increase of silver content induces a decrease of coherence length from 120 to 65 nm for (Ag,Cu)I samples (Table 4.1). This decrease in the coherence length of the (Ag,Cu)I compound can be linked with the decrease in the coherence length values of its metallic precursor (AgCu). It was observed that the coherence length values of the corresponding metallic precursors were decreasing from 39 to 3 nm with increase of the silver content see Table 4.2. As previously

reported for the pure CuI films (chapter 3), the iodination of metallic AgCu films induces a drastic increase of the coherence length.

Table 4.1: Film lattice parameter and coherence length of AgCuI.

Film formula $Ag_xCu_{1-x}I$	**Lattice parameter (nm)**	**Coherence length (nm)**
CuI	6.0545	120
$Ag_{0.07}Cu_{0.93}I$	6.0555	110
$Ag_{0.10}Cu_{0.90}I$	6.0579	100
$Ag_{0.13}Cu_{0.87}I$	6.0627	105
$Ag_{0.15}Cu_{0.85}I$	6.0772	68
$Ag_{0.33}Cu_{0.67}I$	6.1606	70
$Ag_{0.52}Cu_{0.48}I$	6.2456	61
AgI	6.4950	65

Table 4.2: Film lattice parameter and coherence length of AgCu

Film formula Ag_xCu_{1-x}	**Lattice parameter (nm)**	**Coherence length (nm)**
Cu	0.3615	39
$Ag_{0.07}Cu_{0.93}$	0.3617	39
$Ag_{0.10}Cu_{0.90}$	0.3615	40
$Ag_{0.13}Cu_{0.87}$	0.3617	40
$Ag_{0.15}Cu_{0.85}$	0.3648	33
$Ag_{0.33}Cu_{0.67}$	0.3690 & 0.3831	20 & 3
$Ag_{0.52}Cu_{0.48}$	0.3975 & 0.3749	8 & 6
Ag	0.4079	30

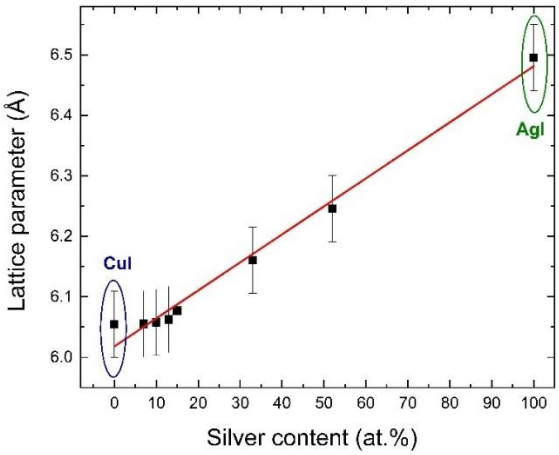

Figure 4.4: Lattice parameter for (Ag,Cu)I thin films samples as a function of silver content. The lattice parameter of the AgI phase comes from the reference [22] and it corresponds to the cubic structure and not to the hexagonal one (Appendix D).

Elemental mapping, using energy dispersive X-ray spectrometry (SEM/EDS), was performed for all samples. The $Ag_{0.33}Cu_{0.67}I$ film was chosen as example Figure 4.5. This analysis clearly evidences the homogeneous distribution of silver, copper and iodine elements in the films. Although we do not show the EDS map of the other sample, a homogeneous distribution of Cu, Ag and I elements is systematically observed for all (Ag,Cu)I films. The chemical composition of the films deduced from EDS measurements are reported Table 4.3. Within the experimental error (± 0.2 at. %), the iodine composition is close to 50 at. % without influence regarding the progressive addition of silver.

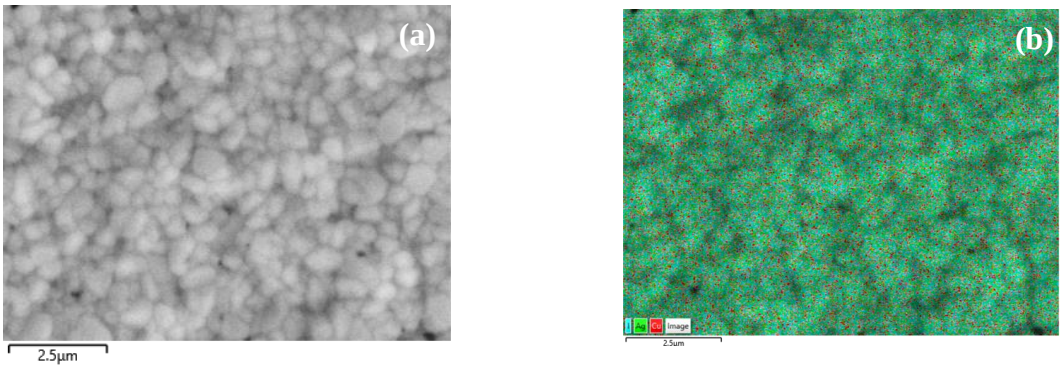

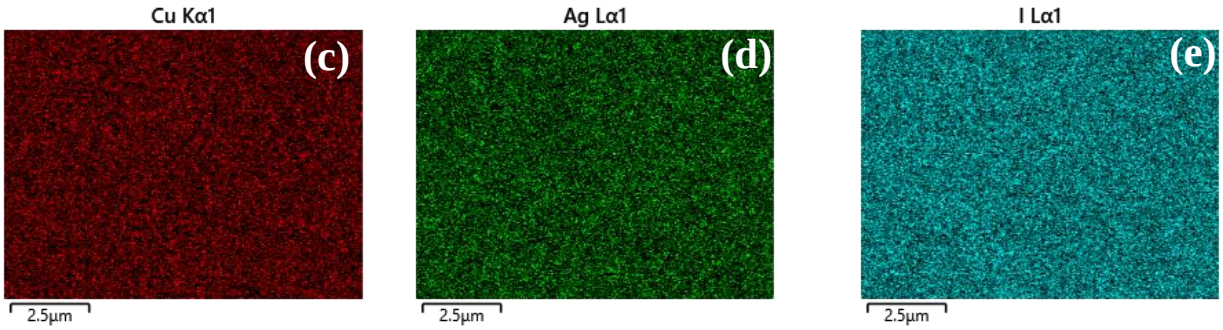

Figure 4.5: Elemental mapping using EDS for the $Ag_{0.33}Cu_{0.67}I$ composition. (a) secondary electron image, (b) cumulative elemental mapping of the elements, (c) Cu, (d) Ag and (e) I.

Table 4.3: Film composition deduced from EDS measurements.

Target current Ag (A)	Ag (at. %)	Cu (at. %)	I (at. %)	Thickness of metallic films (nm)	Measured thickness of iodide films (µm)	Expected thickness (µm)	Film formula $Ag_xCu_{1-x}I$
0.04	0	49.6	50.4	287	1.4	1.34	CuI
0.05	3.5	46.9	49.6	290	1.5	1.30	$Ag_{0.07}Cu_{0.93}I$
0.06	5.1	45.6	49.3	300	1.4	1.31	$Ag_{0.10}Cu_{0.90}I$
0.07	6.6	45.2	48.2	305	1.6	1.30	$Ag_{0.13}Cu_{0.87}I$
0.08	7.6	43.1	49.3	313	1.7	1.34	$Ag_{0.15}Cu_{0.85}I$
0.15	16.6	33.5	49.9	330	1.8	1.37	$Ag_{0.33}Cu_{0.67}I$
0.25	26	24.2	49.8	450	2.5	1.76	$Ag_{0.52}Cu_{0.48}I$

4.2.2 Film morphology

Films morphology has been examined by SEM analysis. In order to compare, the surface morphology was studied for three samples, two binary systems (CuI and AgI) and one ternary $Ag_{0.52}Cu_{0.48}I$, as depicted in Figure 4.6. It can be observed that CuI binary sample shows a compact and dense morphology with irregular and deformed grains Figure 4.6a. This underlines the inhomogeneity of the microstructure and leading to an asymmetry in the average particle size,

about 455 nm Figure 4.6b. CuI films morphology is dependent on the iodination temperature (see Appendix C). Indeed, in chapter 3, the CuI films obtained at 75 °C exhibit regular shape with lower grain size (about 260 nm). For both iodination temperatures, twins are evidenced on the top surface SEM images.

On the contrary, AgI binary sample Figure 4.6e reveals more regular shapes and surfaces with pronounced faceting, compared to CuI. In addition, the estimated average particles sizes, of 556 nm, are more homogeneous. Twins are also observed on pure AgI films.

In the case of ternary sample Figure 4.6c, the morphology of the film surface represents an intermediated state between the two binary films. The grains are starting to get into regular shape close to what are found in the AgI case, but without sharp grain edges. In addition, the average particle size, estimated from the histogram statistics, is approximatively 311 nm Figure 4.6d which is significantly lower than the pure CuI one. This shrinking in the average grains size could explain the existence of some large holes between some grains. We will discuss about the existence of these holes in the section related to the photoluminescence. Microstructure modifications are probably induced by the presence of Ag in the CuI film.

CuI

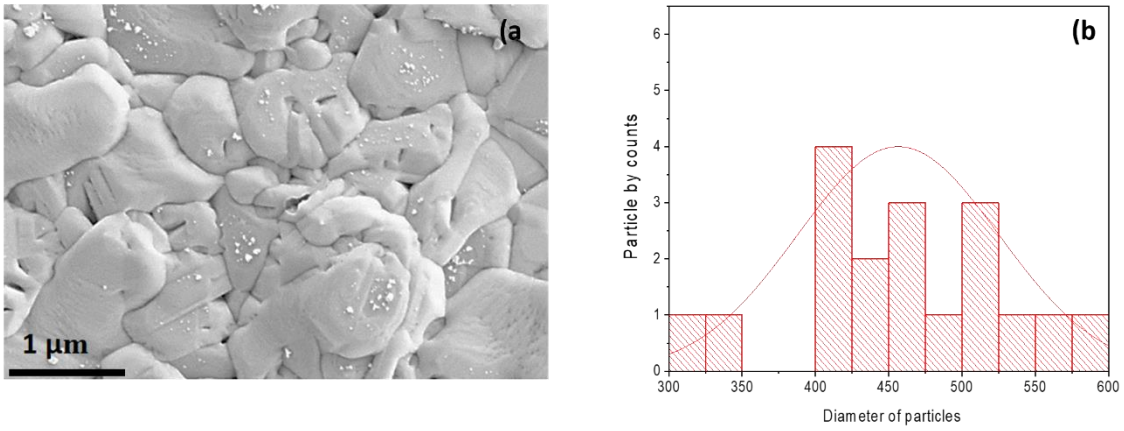

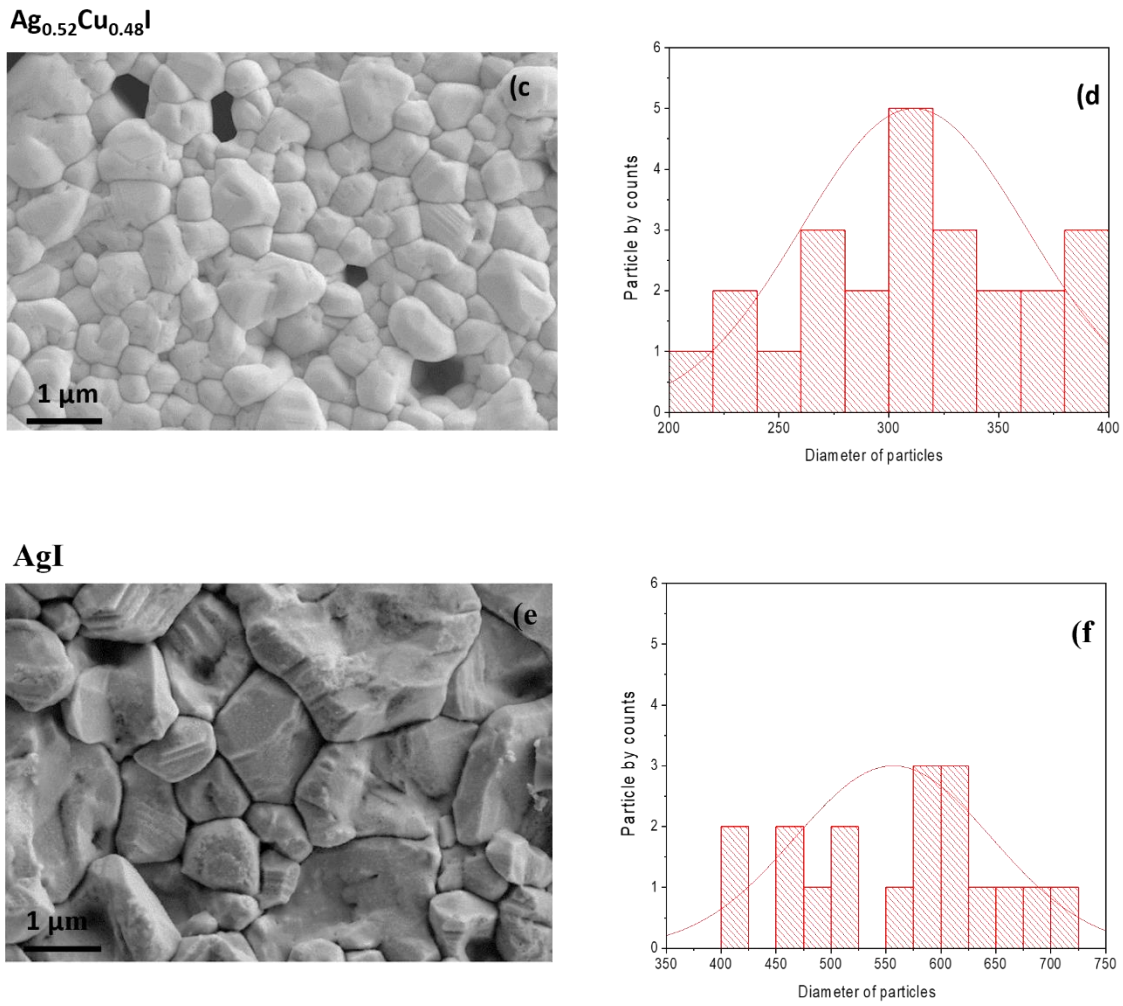

Figure 4.6: Scanning electron microscopy (SEM) images and histograms of particle size distribution prepared on Si. (a) & (d) CuI, (b) & (e) $Ag_{0.52}Cu_{0.48}I$ (c) & (f) AgI.

In order to study the growth of the (Ag,Cu)I layer in TEM, a cross section of the sample was attempted by FIB. Unfortunately, due to the porosity of the (Ag,Cu)I layer, the cross section was impossible to analyze. As it can be seen on the SEM micrograph Figure 4.7a, some nanometric pores appears at the surface of the film which let us think that the (Ag,Cu)I layer is porous. During the cutting process ion beam bombardment widen the pores. The thinner we want the layer (less than 100 nm for TEM analyses), the more difficult is to prevent the pores widening phenomenon.

In our case, the layer is even partially splitted from the substrate Figure 4.7d, which makes TEM analyses impossible. Recently, Zhong *et al*. [23] published their work on a new method to protect pores of porous layers from ion beam damage. This method consists in using FIB to sputter and redeposit material onto the edges of cracks and pores in order to fill it [23].

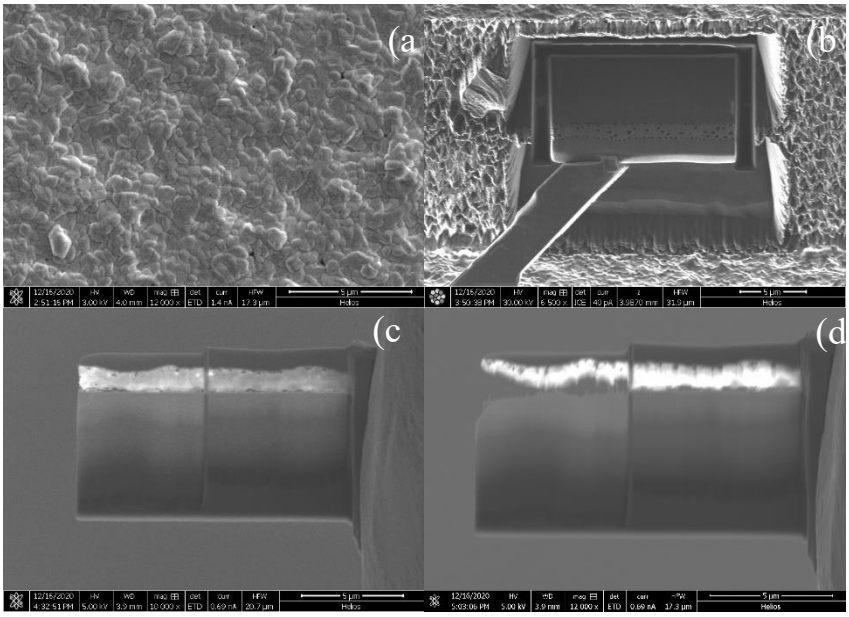

Figure 4.7: a) SEM micrographs of: top surface of the (Ag, Cu)I layer b) porous sample slice ready for final thinning. c) thick FIB lamellae for TEM analyses. d) damaged FIB lamella due to ion bombardment.

4.2.3 Photoluminescence (PL)

To further investigate the optical response of the ternary samples, a photoluminescent (PL) experiment was performed at room temperature. Figure 4.8 shows the PL spectra of as-prepared samples containing variable Ag concentration $Ag_xCu_{1-x}I$ ($0 \leq x \leq 0.52$). PL spectra exhibited two fundamental bands located in blue and red regions. The band in the blue region revealed narrow peak at approximately 410 nm (B-band) with a shoulder at 418 nm. The second band in the red region (R-band) was broader and centered around 730 nm. The origin of these PL bands have been

reported for CuI by Satoshi Koyasu *et al.* [24] and Guochen Lin *et al* .[25]. They attributed the B-band, and its shoulder, to the radiative excitonic recombination and transition from the conduction band to Cu-vacancy defect states in CuI, respectively. On the other hand, the PL of the R-band was assigned to transitions from I-vacancy defect states to the valence band. In the case of ternary composition, the relative spectral features of these bands were dependent on the Ag content. The PL intensity of the B-band decreases and shows redshift with increasing Ag content Figure 4.8b. On the contrary, blueshift for R-band position is observed.

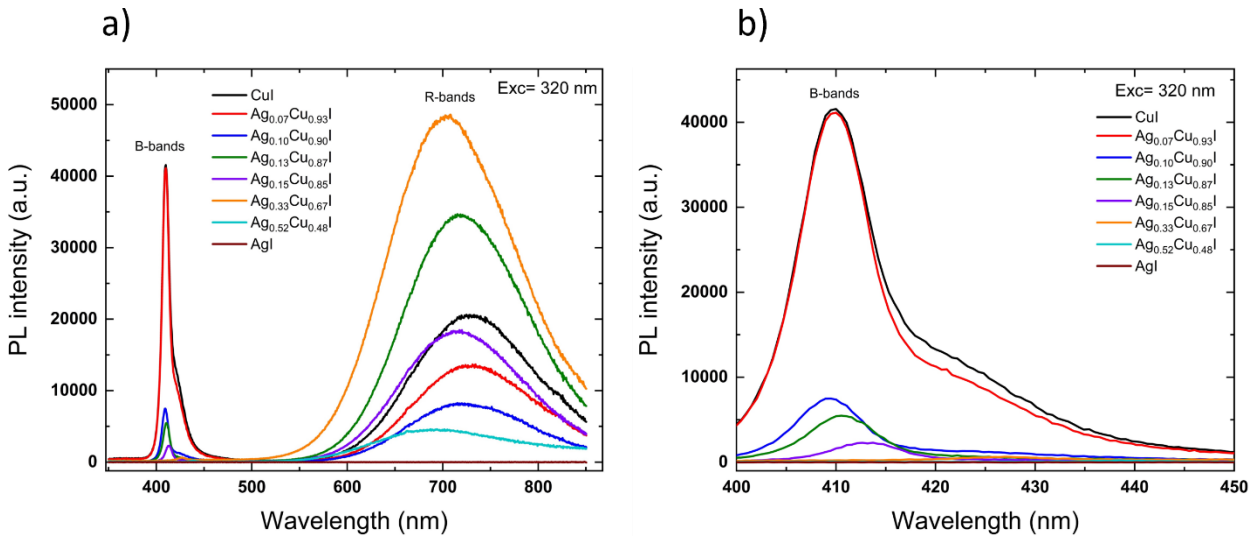

Figure 4.8: a) Photoluminescence (PL) spectra of the (Ag,Cu)I thin films samples for various $Ag_xCu_{1-x}I$ films ($0 \leq x \leq 0.52$). b) Zoom on the B-band

For a better understanding, we should focus on the method used to grow films. As mentioned in the experimental details, films have been prepared by co-sputtering of Cu and Ag, with variable Ag concentrations. Next, each film was iodinated by exposure to the same quantity of iodine for a fixed duration (2 h). Due to the higher reactivity of Ag to iodine compared to Cu, I atoms reacted

preferentially with Ag. This produced a deficiency in I atoms, during the growth of CuI crystal in the ternary compositions, compared with binary CuI sample. Hence, as the Ag concentration increases, the number of I-vacancies increases in the CuI cubic lattice structure. This likely the reason behind the tendency of phase changes from cubic structure (pure CuI crystals) to hexagonal one (ternary (Ag,Cu)I) [20], although this phase change was not observed in our study.

This can explain the decrease in the intensity of the B-band, which is associated to the excitonic transition of Cu-I band structure. In addition, it induces redshift in the position of the B-band towards reported excitonic PL peak of Ag-I; around 430 nm measured at low temperature [26]. While in our case measuring the PL at room temperature shows absence of the PL bands related to AgI, agrees with the literature [26].

On the other hand, the blueshift in the R-band could be attributed to the position change of CBM and VBM (conduction and valence band maxima) as reported in [20]. The authors reported a change in the CBM and VBM positions with a movement of the corresponding Fermi level towards CBM, as the Ag fractions increase. Considering that the origin of the R-band is a transition from a donor (I-vacancy) defect state to the valence band, the blueshift in the PL of the R-band can be relevant.

In addition, the behaviour of the relative PL intensity of R-band/B-band (PLR/PLB) for different Ag contents could be attributed to the density of I-vacancies in CuI crystal Figure 4.9. The relative PL intensity increases within the copper rich conditions ($x \leq 0.33$) before decreasing in the silver rich sample $Ag_{0.52}Cu_{0.48}I$. As the R-band is associated to the I-vacancy in the CuI crystals, this maybe infer that CuI lattice structure, containing I vacancies, can be sustained under sub-stoichiometric conditions (i.e., copper rich) in the ternary composition, as demonstrated in XRD. However, at over-stoichiometric conditions (i.e., silver rich), the relative intensity of the R-band/B-

band decreases. This can be linked to a high density of I-vacancies in CuI lattice rising possible vacancies recombination which could form void in the structure, as can be seen in Figure 4.6c. These important vacancies density may reduce the number of optically active sites (I-vacancies) and leads to decrease the R-band/B-band intensity.

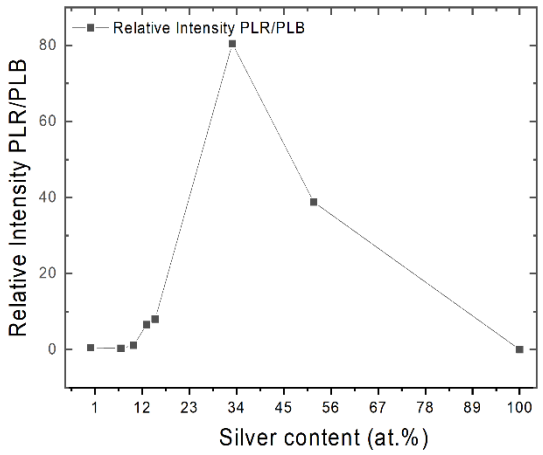

Figure 4.9 relative the R-band/B-band intensity of the (Ag,Cu)I thin films samples as a function of the silver content (corresponding to $Ag_xCu_{1-x}I$ $(0 < x < 0.52)$).

These relative spectral modifications, due to the Ag contents, will not only change the electrical response, as will discussed later, but also change the color of the emitted light. The CIE chromaticity diagram Figure 4.10 can intuitively represents the properties of the emission color with different Ag content. Change of the coordination point, in different color regions, corresponds to the change of silver content. This confirms the possibility of controlling the emission color, by adjusting the stoichiometric ratio, giving an excellent way to engineer light emitting devices, based on (Ag,Cu)I.

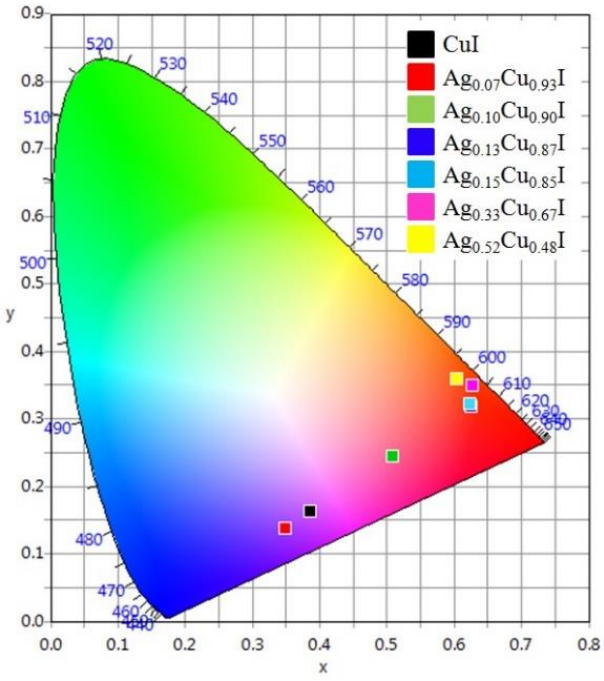

Figure 4.10: CIE chromaticity diagram coordinates of all samples

4.2.4 Optical properties of (Ag,Cu)I films

The optical transmission of the prepared samples has been measured at room temperature. Figure 4.11 shows transmittance spectra depending on silver content. This behavior in (Ag,Cu)I material has been also reported by Annadi et al [20], where some of their samples that contain high Ag content exhibit higher transmittance compared to other samples, which doesn't follow the behavior observed for our samples. On the other side, the films thicknesses increase with increasing the Ag content. This supports the fact of high reactivity of silver with I atoms, which speed up the reactions of the components and lead to higher growth rate of the films. As the deposition duration is kept constant for all growth films, samples with higher silver contents exhibit higher thickness. The estimated films thicknesses as a function of silver content are found to be 1.4, 1.5, 1.4, 1.6, 1.7, 1.8 and 2.5 μm for CuI, $Ag_{0.07}Cu_{0.93}I$, $Ag_{0.10}Cu_{0.90}I$, $Ag_{0.13}Cu_{0.87}I$, $Ag_{0.15}Cu_{0.85}I$, $Ag_{0.33}Cu_{0.67}I$

and $Ag_{0.52}Cu_{0.48}I$, respectively. A decrease of the transmittance with the thickness is expected, but it is not the case here. It is difficult to interpret this behavior as other parameters; beside the film thickness should be considered. Films roughness, optical properties of AgI, compared to CuI, and their ternary compounds, as well as the formed local structural defects, could compete together and contribute in the average transmission of whole film.

On the other hand, the estimated bandgap in Figure 4.12, extracted from Tauc's plot, shows a decrease, from 3 eV (CuI) to 2.7 eV (AgI), as a function of silver content Figure 4.13. Such a behavior is in agreement with the reported change in the bandgap of AgCuI [20]. This bandgap engineering approach could also be a chance.

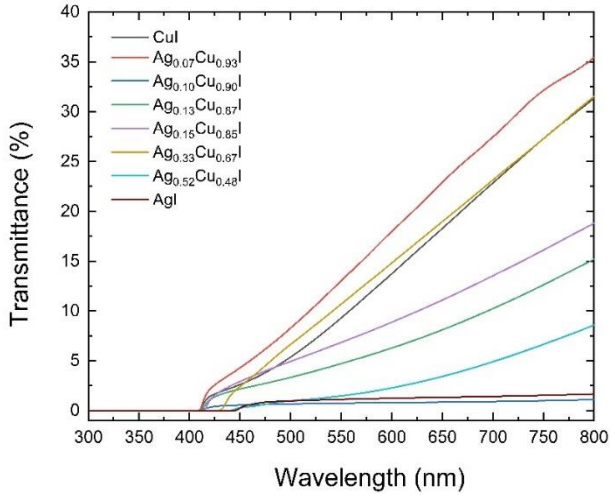

Figure 4.11: Transmission spectra of the (Ag,Cu)I thin films in the 0 – 52 at. % silver content range.

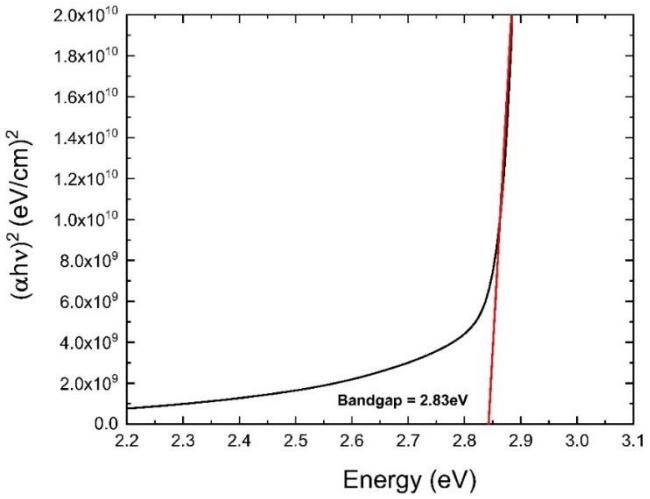

Figure 4.12: Depiction of a typical Tauc's plot of (Ag,Cu)I film for $Ag_{0.33}Cu_{0.67}I$

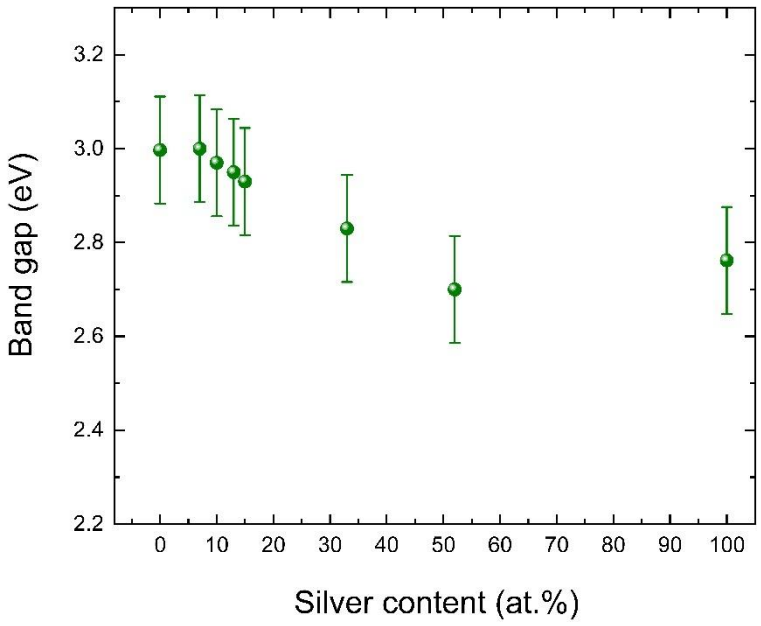

Figure 4.13: The variation of the band gap as a function of the silver content (corresponding to $Ag_xCu_{1-x}I$ *(0 < x < 0.52)).*

4.2.5 Electrical properties of (Ag,Cu)I thin films

In order to investigate the electrical response of the prepared samples, Hall effect measurements have been performed. The obtained electrical resistivity, mobility and carrier density as a function of the Ag content are displayed in Figure 4.14 (a, b, c respectively).

Pure CuI film exhibits an electrical resistivity of 0.33 Ω cm while pure AgI film exhibits an electrical resistivity of 13.6 Ω cm. Addition of silver at low content ($x < 0.15$) induces a weak increase of the resistivity. A maximum of 17.5 Ω cm is measured for the $Ag_{0.33}Cu_{0.67}I$ film. CuI is intrinsically p-type thanks to the domination of Cu-vacancy (acceptor) point defect due to its low formation energy [5,24,27]. As mentioned above, addition of silver results in I-vacancies formation (donor type defect) which compensates the Cu-vacancy. This compensation effect makes the material less conductive and explains the increase of the electrical resistivity with

increasing silver content Figure 4.14a. This eventually reduces the number of holes in the material and results in decreasing its carrier density until a crossover from p-type to n-type is occurred Figure 4.14c and Table 4.4.

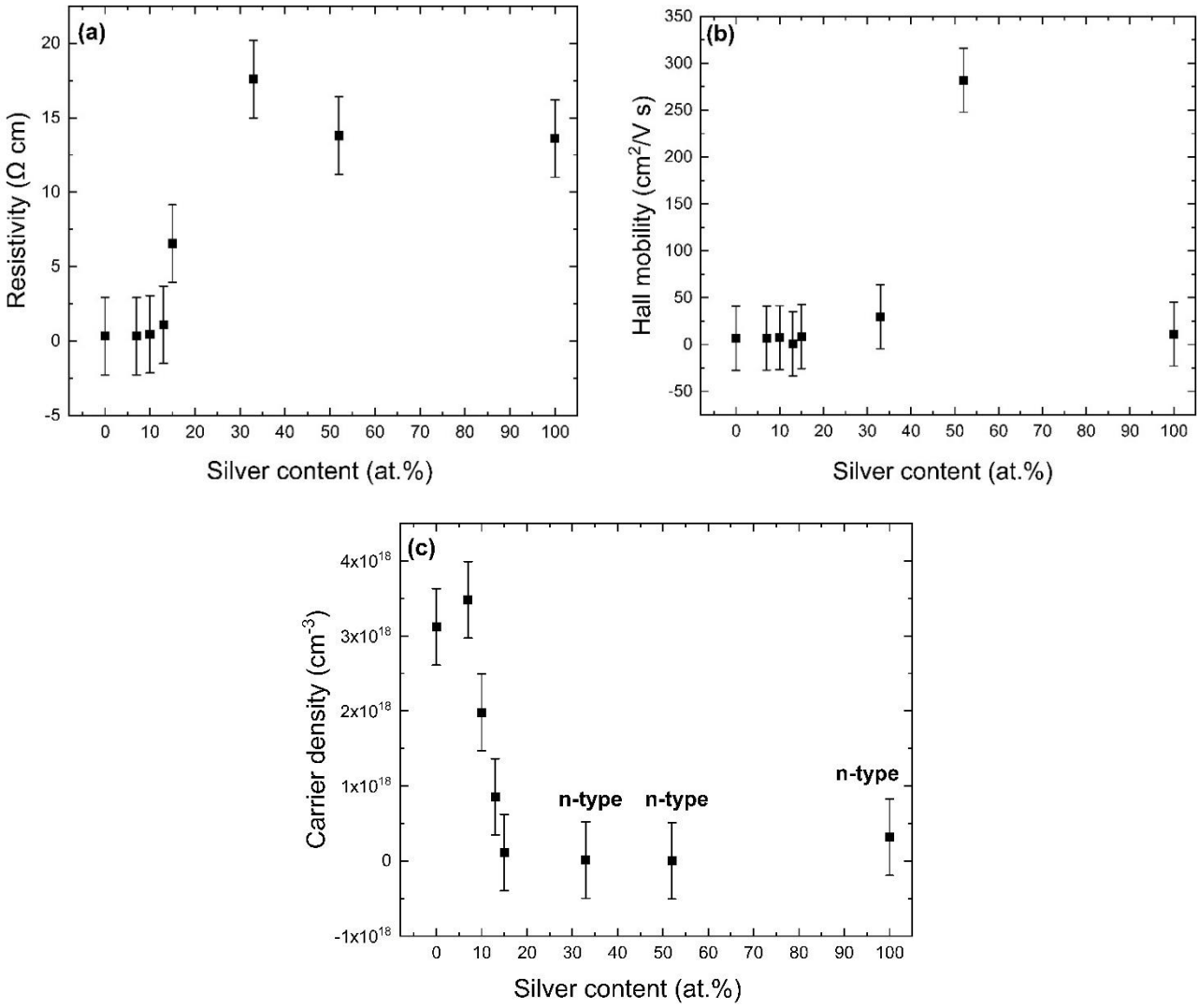

Figure 4.14: Resistivity(a), Hall mobility(b) and carrier density(c) measured for (Ag,Cu)I films depending on silver content.

The change of the defect type influence occurs when the silver content increases from ($0.15 \leq x \leq 0.52$). In this line, it is interesting to note the similarity between the behaviour of the measured electrical resistivity and the relative R-band/B-band intensity associated to the I-vacancies in the PL results Figure 4.15.

Table 4.4: carrier concentration of the (Ag,Cu)I thin films samples.

Film formula $Ag_xCu_{1-x}I$	Carrier concentration (cm^{-3})
CuI	3.12E18
$Ag_{0.07}Cu_{0.93}I$	3.48E18
$Ag_{0.10}Cu_{0.90}I$	1.98E18
$Ag_{0.13}Cu_{0.87}I$	8.55E17
$Ag_{0.15}Cu_{0.85}I$	1.12E17
$Ag_{0.33}Cu_{0.67}I$	–1.2E16
$Ag_{0.52}Cu_{0.48}I$	–2.15E15
AgI	–3.174E17

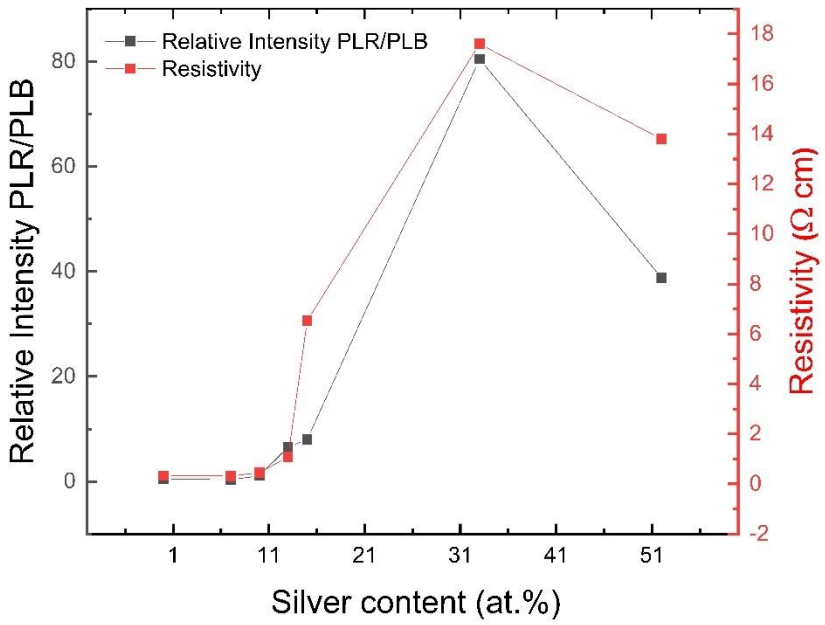

Figure 4.15: Electrical resistivity and the relative the R-band/B-band intensity of the (Ag,Cu)I thin films samples as a function of the silver content.

The strong coherency between the electrical and optical measurements emphasizes the link between I-vacancies and the electrical response (i.e. resistivity). It is worth to mention that, the reported increase of (Ag,Cu)I resistivity, as a function of Ag content, has been attributed to the increase in the number of activated electrons from Ag^{+} [20]. Hence, a continuous increase in the resistivity, with increasing Ag fraction, is expected. However, in our case, the resistivity follows the same behaviour that the relative R-band/B-band intensity and decreases in the over-stoichiometric condition. This strongly motivates us to propose that the origin of the activated electrons, which play a primary role in the resistivity response, is a consequence of the generated I-vacancies. In addition, increasing such donor type defects likely neutralize the ionized positive scattering centers and leads to improve the carrier mobility as shown in Figure 4.13b. Thus, the Cu-vacancies not only act as acceptors, but also as ionized impurities. For obtaining more information about the material property, the temperature influence on the resistivity was measured for sample $Ag_{0.33}Cu_{0.67}I$ Figure 4.16a. It can be observed that the resistivity exhibits Arrhenius type behaviour by decreasing exponentially with the temperature Figure 4.16b. This indicates the semiconductor nature of the prepared material. Figure 4.16c shows the evolution of the activation energy as a function of the silver content except the sample $Ag_{0.52}Cu_{0.48}I$.

Activation energy is extracted by fitting the obtained data and found to be 9.6 meV for $Ag_{0.33}Cu_{0.67}I$ Figure 4.16b. Indeed, there is a lack of information about the low temperature behaviour of (Ag,Cu)I and the expected activation energy value. However, for comparison point of view, Yamada *et al.* [28], reported different activation energies ranging from 4 to 200 meV for a CuIBr alloys and showed an increase in the activation energy with doping by Br.

Here, the value of the estimated activation energy falls within their range. Hence, the temperature dependence behaviour may be explained as follows. The resistivity shows decreasing function

with the temperature, in other words, it indicates a thermal stimulated conductivity. It is well-established that, in this study and literature, the conductivity of p-type CuI-based materials is originating from the majority of Cu-Vacancy (acceptor). Hence, it can be proposed that increasing (decreasing) of the conductivity (resistivity) with temperature is attributed to the ionization of the shallow acceptor Cu vacancy with activation energy equivalent to 9.6 meV.

In Chapter 3, we discussed how important it is to understand FOM since it defines the behaviour of transparent conductive thin films. The FOM of (Ag,Cu)I thin films prepared with varying content of silver (Table 4.5). As shown in Figure 4.17, the high value of FOM indicates the strong performance of transparent conductive thin films in the first and second of this series. According to the literature, the figure of merit (FOM) may be used to compare the properties of different transparent conductive materials. Within the silver content tested in the present study, the FOM ranges from 240 to 5 $M\Omega^{-1}$, which is lower than the range reported by Anil et al [20], that is between 1390 and 23$M\Omega^{-1}$.

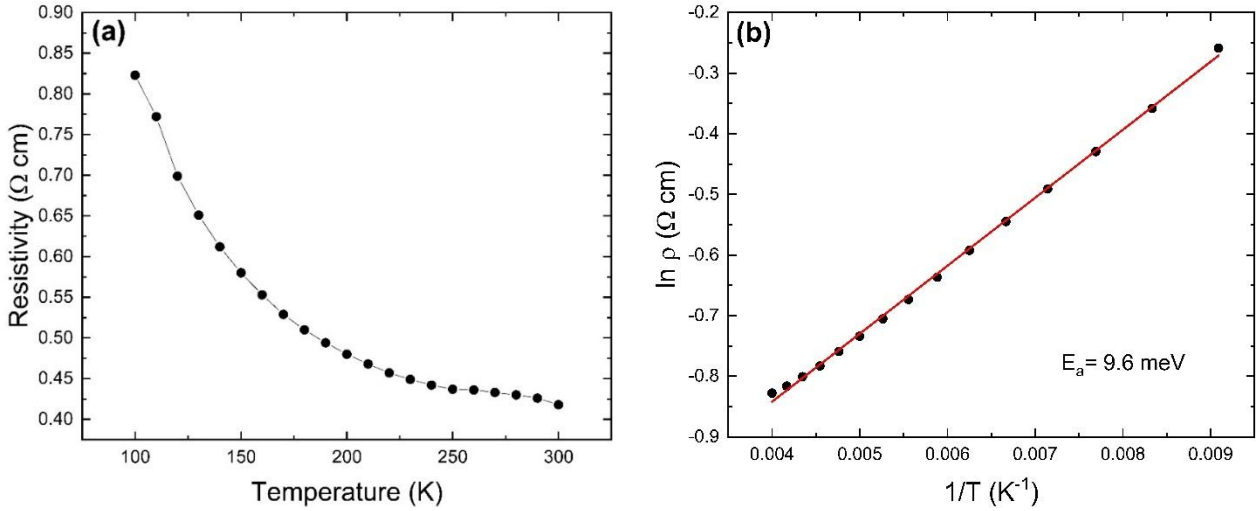

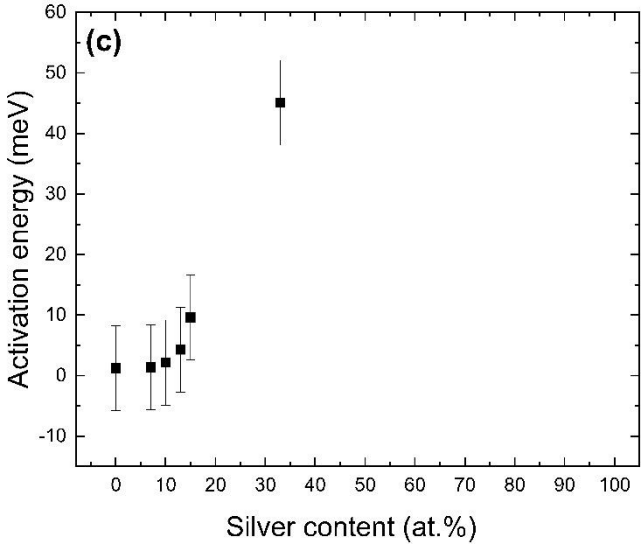

Figure 4.16: (a) Resistivity vs. temperature for $Ag_{0.33}Cu_{0.67}I$. (b) Arrhenius plot for calculation of apparent activation energy from 250 to 110 K (c) Activation energy as a function of silver content.

Table 4.5: Thickness, transmittance, conductivity and the figure of merit of the (Ag,Cu)I thin films samples.

Film formula $Ag_xCu_{1-x}I$	**Thickness (µm)**	**T (%)**	**Conductivity (S cm^{-1})**	**FOM ($M\Omega^{-1}$)**
CuI	1.4	11.5	3.1	200
$Ag_{0.07}Cu_{0.93}I$	1.5	14.4	3.11	240
$Ag_{0.10}Cu_{0.90}I$	1.4	0.61	2.21	61
$Ag_{0.13}Cu_{0.87}I$	1.6	5.9	0.92	52
$Ag_{0.15}Cu_{0.85}I$	1.7	7.4	0.15	10
$Ag_{0.33}Cu_{0.67}I$	1.8	11.9	0.057	4.82
$Ag_{0.52}Cu_{0.48}I$	2.5	2.4	0.072	4.83
AgI	3.3	0.87	0.074	5

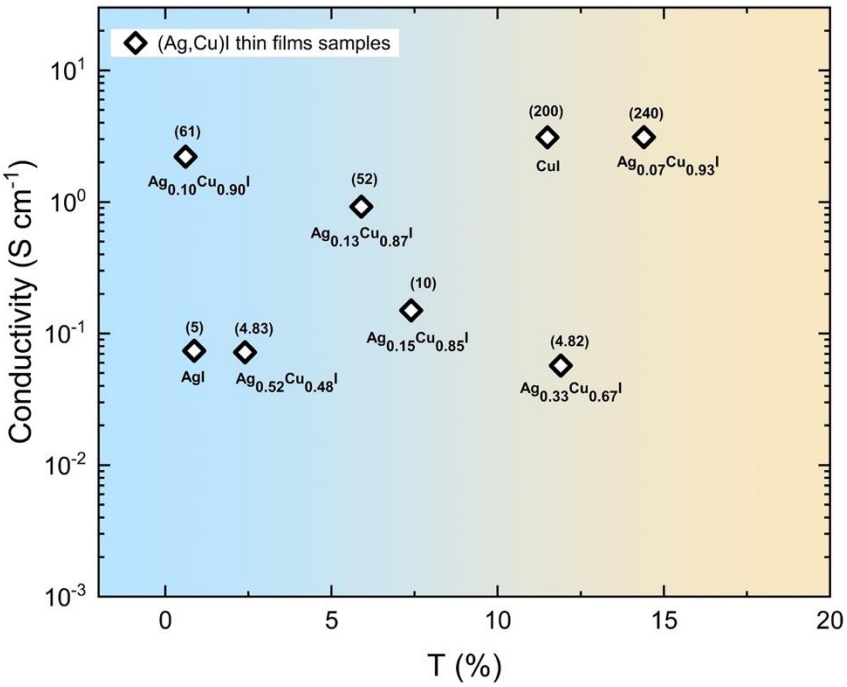

Figure 4.17: Evolution of electrical conductivity and averaged visible transmittances and the figure of merit of the (Ag,Cu)I films.

4.3 Conclusion

In this work, we have synthesized at room temperature (Ag,Cu)I films using a two step process. The silver-copper metallic films deposited via magnetron sputtering have been submitted to an iodination step using iodine vapor. The iodide films have been characterized using XRD, SEM, PL, UV-visible and Hall effect techniques. Iodide films show a strong preferred orientation along the [111] direction. Within the silver content tested in this study, all the films crystallize in the γ-CuI structure. The linear evolution of the lattice constant vs. the silver content indicates that silver atoms substitute copper ones into the copper iodide lattice. The surface morphology of the films is not flat and includes tiny porosities. The increase of the silver concentration induces a progressive decrease of the optical band gap from 3 to 2.7 eV. In addition, the photoluminescence (PL) properties of all $Ag_xCu_{1-x}I$ samples have been carefully evaluated. The PL results show three

bands related spectral contributions at different wavelengths: 410, 418 and 730 nm. The origin of these PL contributions is attributed to radiative excitonic recombination, the transition from the conduction band to Cu-vacancy defect states, and transitions from I-vacancy defect states to the valence band respectively Moreover, the PL results show a coherent trend with the electrical results and lead to rigorous interpretation about the origin of the carrier's behavior. The electrical conductivity has been measured at low temperature and allows us to access the activation energy. Our findings show also a crossover from p-type to n-type material as the Ag contents increases while the structure does not change. This has been discussed in details and correlated with both the optical and electrical results. As the Ag content increases, the resistivity increases from 0.32 to 17.6 Ω.cm. The change in the film stoichiometry results in modification of the points defects which, in turns, tune the functional response from the material. This approach opens the door to have a practical control on the functional properties from the process point of view.

References

[1] J.-H. Cha, D.-Y. Jung, Air-Stable Transparent Silver Iodide–Copper Iodide Heterojunction Diode, ACS Applied Materials & Interfaces. 9 (2017) 43807–43813. https://doi.org/10.1021/acsami.7b14378.

[2] Q. Chen, N. De Marco, Y. (Michael) Yang, T.-B. Song, C.-C. Chen, H. Zhao, Z. Hong, H. Zhou, Y. Yang, Under the spotlight: The organic–inorganic hybrid halide perovskite for optoelectronic applications, Nano Today. 10 (2015) 355–396. https://doi.org/10.1016/j.nantod.2015.04.009.

[3] C.G. Granqvist, Transparent conductors as solar energy materials: A panoramic review, Solar Energy Materials and Solar Cells. 91 (2007) 1529–1598. https://doi.org/10.1016/j.solmat.2007.04.031.

[4] H. Kim, J.S. Han, S.G. Kim, S.Y. Kim, H.W. Jang, Halide perovskites for resistive random-access memories, J. Mater. Chem. C. 7 (2019) 5226–5234. https://doi.org/10.1039/C8TC06031B.

[5] M. Grundmann, F.-L. Schein, M. Lorenz, T. Böntgen, J. Lenzner, H. von Wenckstern, Cuprous iodide: A p-type transparent semiconductor, history, and novel applications: Cuprous iodide, Physica Status Solidi (a). (2013) n/a-n/a. https://doi.org/10.1002/pssa.201329349.

[6] Y. Wang, J. Mo, W. Cai, L. Yao, L. Zhang, Synthesis of nano-AgI arrays and their optical properties, Journal of Materials Research. 16 (2001) 990–992. https://doi.org/10.1557/JMR.2001.0139.

[7] Y. Lu, S. Zhu, E. Huang, Y. He, J. Ruan, G. Liu, H. Yan, Pressure-driven band gap engineering in ion-conducting semiconductor silver orthophosphate, J. Mater. Chem. A. 7 (2019) 4451–4458. https://doi.org/10.1039/C8TA10606A.

[8] P.V. Smith, A tight-binding approach to the electronic structure of the silver halides—II: The silver iodide polymorphs, Journal of Physics and Chemistry of Solids. 37 (1976) 589–597. https://doi.org/10.1016/0022-3697(76)90108-6.

[9] M.Y. Bashouti, R. Talebi, T. Kassar, A. Nahal, J. Ristein, T. Unruh, S.H. Christiansen, Systematic Surface Phase Transition of Ag Thin Films by Iodine Functionalization at Room Temperature: Evolution of Optoelectronic and Texture Properties, Scientific Reports. 6 (2016) 21439. https://doi.org/10.1038/srep21439.

[10] K. Zhao, G.O. Ngongang Ndjawa, L.K. Jagadamma, A.E. Labban, H. Hu, Q. Wang, R. Li, M. Abdelsamie, P.M. Beaujuge, A. Amassian, Highly efficient organic solar cells based on a robust room-temperature solution-processed copper iodide hole transporter, Nano Energy. 16 (2015) 458–469. https://doi.org/10.1016/j.nanoen.2015.07.018.

[11] N. Yamada, R. Ino, Y. Ninomiya, Truly Transparent p-Type γ-CuI Thin Films with High Hole Mobility, Chemistry of Materials. 28 (2016) 4971–4981. https://doi.org/10.1021/acs.chemmater.6b01358.

[12] C. Yang, D. Souchay, M. Kneiß, M. Bogner, H.M. Wei, M. Lorenz, O. Oeckler, G. Benstetter, Y.Q. Fu, M. Grundmann, Transparent flexible thermoelectric material based on non-toxic earth-abundant p-type copper iodide thin film, Nature Communications. 8 (2017). https://doi.org/10.1038/ncomms16076.

[13] T. Tani, H. Mifune, S. Yamashita, S. Aiba, T. Ohzeki, K. Yamane, Ionic and Electronic Properties of Silver Iodide Grains, J. Imaging Sci. Technol. 51 (2007) 202. https://doi.org/10.2352/J.ImagingSci.Technol.(2007)51:3(202).

[14] D. Chen, Y. Wang, Z. Lin, J. Huang, X. Chen, D. Pan, F. Huang, Growth Strategy and Physical Properties of the High Mobility P-Type CuI Crystal, Crystal Growth & Design. 10 (2010) 2057–2060. https://doi.org/10.1021/cg100270d.

[15] M. Vukic, D. Veselinovic, V. Markovic, Crystalline forms of silver iodide II: Determination of phase transformations, J Serb Chem Soc. 72 (2007) 857–868. https://doi.org/10.2298/JSC0709857V.

[16] Y.H. Han, H.B. Wang, I.A. Troyan, C.X. Gao, M.I. Eremets, Pressure induced ionic-superionic transition in silver iodide at ambient temperature, J. Chem. Phys. 140 (2014) 044708. https://doi.org/10.1063/1.4862824.

[17] K. Funke, R.D. Banhatti, P. Grabowski, J. Nowinski, W. Wrobel, R. Dinnebier, O. Magdysyuk, Low-temperature α-AgI confined in glass: Structure and dynamics, Solid State Ionics. 271 (2015) 2–9. https://doi.org/10.1016/j.ssi.2014.09.033.

[18] M.R. Johan, T.S. Leng, N.L. Hawari, S. Suan, Phase Transition and Complex Impedance Studies of Mechano- Chemically Synthesized AgI-CuI Solid Solutions, Int. J. Electrochem. Sci. 6 (2011) 10.

[19] P.S. Kumar, P. Balaya, P.S. Goyal, C.S. Sunandana, Effect of Cu-substitution on the conductivity of Ag-rich AgI–CuI solid solutions, Journal of Physics and Chemistry of Solids. 64 (2003) 961–966. https://doi.org/10.1016/S0022-3697(02)00455-9.

[20] A. Annadi, H. Gong, Success in both p-type and n-type of a novel transparent AgCuI alloy semiconductor system for homojunction devices, Applied Materials Today. 20 (2020) 100703. https://doi.org/10.1016/j.apmt.2020.100703.

[21] D.B. Mohan, C.S. Sunandana, Nanophases in mechanochemically synthesized AgI–CuI system: structure, phase stability and phase transitions, Journal of Physics and Chemistry of Solids. 65 (2004) 1669–1677. https://doi.org/10.1016/j.jpcs.2004.04.007.

[22] O. Madelung, U. Rössler, M. Schulz, Silver iodide (AgI) crystal structure, high pressure modifications, lattice parameters: Datasheet from Landolt-Börnstein - Group III Condensed Matter · Volume 41B: "II-VI and I-VII Compounds; Semimagnetic Compounds" in SpringerMaterials (https://doi.org/10.1007/10681719_130), Springer-Verlag Berlin Heidelberg, n.d. https://doi.org/10.1007/10681719_130.

[23] X.L. Zhong, An in-situ method for protecting internal cracks/pores from ion beam damage and reducing curtaining for TEM sample preparation using FIB, (2020) 9.

[24] S. Koyasu, N. Umezawa, A. Yamaguchi, M. Miyauchi, Optical properties of single crystalline copper iodide with native defects: Experimental and density functional theoretical investigation, Journal of Applied Physics. 125 (2019) 115101. https://doi.org/10.1063/1.5082865.

[25] G. Lin, F. Zhao, Y. Zhao, D. Zhang, L. Yang, X. Xue, X. Wang, C. Qu, Q. Li, L. Zhang, Luminescence Properties and Mechanisms of CuI Thin Films Fabricated by Vapor Iodization of Copper Films, Materials. 9 (2016) 990. https://doi.org/10.3390/ma9120990.

[26] S. Mochizuki, Y. Ohta, Excitons in AgI, Journal of Luminescence. 87–89 (2000) 299–301. https://doi.org/10.1016/S0022-2313(99)00321-X.

[27] D.K. Kaushik, M. Selvaraj, S. Ramu, A. Subrahmanyam, Thermal evaporated Copper Iodide (CuI) thin films: A note on the disorder evaluated through the temperature dependent electrical properties, Solar Energy Materials and Solar Cells. 165 (2017) 52–58. https://doi.org/10.1016/j.solmat.2017.02.030.

[28] N. Yamada, Y. Tanida, H. Murata, T. Kondo, S. Yoshida, Wide-Range-Tunable p-Type Conductivity of Transparent CuI1−xBrx Alloy, Advanced Functional Materials. 30 (2020) 2003096. https://doi.org/10.1002/adfm.202003096.

General conclusion

Halide semiconductors are at the very beginning of semiconductor technology and science. Two types of materials have been prepared in this work: binary (CuI) and ternary (Ag,Cu)I thin films. A brief introduction on the general and basic properties of copper-based halide materials has been given. All the necessary structural, microstructural and functional properties of the prepared samples have been investigated.

For the binary system (CuI), metallic copper thin films have been synthesized at room temperature via magnetron sputtering. These films have been submitted to an iodination step using iodine vapour. The influence of the iodine amount has been presented in this manuscript. Although the iodination step occurs at low temperature, the CuI films are highly crystallized. The reaction with iodine induces the formation of large iodide grains, but porosities are evidenced on the top surface using SEM. The careful investigation of the microstructure by TEM, reported for first time for CuI films, evidence the occurrence of twins in the CuI grains. Such new result were obtained using a nitrogen cooled sample holder. In addition to the structural and microstructural characterization of CuI films, optical and electrical properties have been investigated. The p-type behaviour of CuI has been confirmed by Hall effect measurements. Compared to other p-type oxide, CuI films exhibit high electrical conductivity. Such high values come with high transparency in the visible range. The optical band gap of the CuI films is approx. 3.05 eV. The combination of optical and electrical properties induce high value of figure of merit. Finally, the photoluminescence result allows better understanding and assign the presence of native defects that resulted in eye-observed

strong blue emission. These results clearly evidence that a two step process for the synthesis of copper iodide is a suitable process to deposited high quality copper iodide thin films.

The ternary (Ag, Cu)I thin films have been also prepared through a two-step method: deposition of metallic Ag-Cu films by magnetron sputtering followed by an iodination process. The silver content of the films was ranging between 0 and 55 at. %. The as-prepared films exhibit a strong preferred orientation along the [111] direction. Whatever the silver content, only the the γ-CuI structure is evidenced by X-ray diffraction. Silver atoms substitute copper ones in the copper iodide lattice, as evidenced by the linear evolution of the lattice constant vs. silver content. Although metallic films at high silver content are biphased, EDS mapping on iodide thin films clearly evidence that the copper and silver are homogeneously distribution along the film surface. Optical and electrical properties have been investigated as a function of the silver content. When the silver concentration is lower than approx. 30 at. %, the films exhibit a p-type conductivity while a n-type one is evidenced for higher silver content. In addition the optical bandgap of (Ag,Cu)I thin films can be modulated between 3.04 and 2.7 eV. Guided by the PL results, the alloying effects develop distinct luminescent levels resulting from defects. The PL results demonstrate three bands with distinct spectrum contributions at 410, 418, and 730 nm. Radiative excitonic recombination is thought to be the origin of these PL contributions. This has been reported as a promising candidate to widely tune the CBM and VBM, which can be used to energetically better match band alignments in optoelectronic device applications. Moreover, our findings show a clear correlation between the photoluminescence and electrical measurements. This help us to interpret and define the origin of the behaviour of the generated carriers. Electrical resistivity at room temperature increases from 0.32 to 17.6 Ω cm as the Ag content increases

Finally, the low temperature electrical conductivity helps us to access the electrical activation energy. This parameter increases with the silver content. This has been described in detail and correlated with both the optical and electrical results.

Perspective

From the above findings it can be realized the interesting optical and electrical features of copper iodide-based materials in the optoelectronic applications. During this work, we tried to shine light on these properties and propose an interpretation of the obtained results by correlating the structure, optical, and electrical results. However, this research line, within our team, is still in the beginning and many features and phenomena need to be deeply investigated and explored. For instance, the appearance of the twin structure in CuI material is very promising and deserved to be more investigated. I would propose to do a dedicated study to carefully examine the effect of different preparation conditions on the behaviour of such local twin structure. Hopefully to approach a methodology to fully control its structural properties like the size, the shape, the twin angle…etc. In addition, the link between these structures modifications and the optical and electrical properties of the deposited layer can be also interested. This also required the deep study of the nucleation of the early growth stages of the material. In the meantime, similarly to CuI samples, we will conduct a theoretical approach to figure out the fundamental properties of the ternary alloy AgCuI thin films. A detailed study about the growth mechanism using TEM characterization of partially iodided films seems very promising.

Moreover, from the application point of view, the luminescence properties of the prepared samples showed a blue emission with color characterizations that can be controlled by the processing parameters. Together with optimizing the electrical response between n and p types in (Ag, Cu)I,

multilayer structure can be a promising candidate for approaching an efficient light emitting diode device.

The different features of copper and silver-copper iodides thin films prepared using our two step process should be compared to those obtained on iodide films obtained by magnetron sputtering of iodide targets.

Appendix A

Determination of the optimum elaboration conditions for copper iodide

Copper iodide thin films have been elaborated at different conditions in order to determine the optimum processing parameters. During our study we have checked three main parameters: temperature, duration time and different amounts of iodine, represented in three series as follows:

Series I: Temperature (50 - 75 - 90 - 120) °C, 0.1 g I_2 , 180 min

Series II: Duration (20 - 30 - 60 - 150) minutes, 0.1 g I_2 , 75 °C

Series III: I_2 amount (0.10 – 0.15 – 0.20 – 0.50 g), 60 minutes, 75 °C

- ***Series I: Temperature (50 - 75 - 90 - 120) °C, 0.1 g I_2, 180 min***

In this series we have prepared CuI thin films at fixed amounts of iodine (0.1g) and during long duration (180 minutes) in order to ensure a complete reaction. Whatever the iodination temperature, X-ray diffraction analyses confirm that all samples crystallised in the γ-CuI phase (not shown here). The electrical properties of the prepared series have been measured using Hall effect experiment. Table A.1 shows the obtained results for the carrier concentration, the mobility and the conductivity. It can be observed that all the films exhibit poor electrical properties with low electrical mobility and conductivity. Thanks to the importance of the electrical mobility as a parameter in different applications, we have selected the mobility as criteria for optimizing our elaboration conditions. From Table A.1, we can see that the film prepared at 75 °C shows slightly higher mobility. Thus, we switched to study the effect of elaboration duration for CuI films prepares at this temperature 75 °C, in the second series.

Table A.1: CuI prepared at different temperature with fixed 0.1 g I_2, 180 min

Temperature (°C)	Carrier concentration (cm^{-3})	Mobility ($cm^2 V^{-1} s^{-1}$)	Conductivity ($S\ cm^{-1}$)
50	4.17E+18	2.40	1.3
75	3.03E+18	2.60	1.1
90	1.36E+18	1.01	0.8
120	3.61E+18	1.20	0.6

In this series CuI films have been prepared at different durations (20 - 30 - 60 - 150) minutes and fixed amount of iodine (0.1 g), and fixed temperature (75 °C). Table A.2 shows the electrical properties of this series measured by Hall effect experiment. We can see that all films reveal good electrical parameter with best mobility of 44.7 $cm^2V^{-1}s^{-1}$ prepared with duration time at 60 minutes. The further investigation of the crystal structure of this series shows that all films crystallize in the γ-CuI phase with the [111] preferred orientation, as depicted in XRD (Figure A.1). In addition, see Figure A.2 and Table A.3, the estimate coherence length deduced from Scherrer formula shows that the sample prepared at 60 min has the highest coherence length (i.e., high crystallinity). Moreover, the SEM micrographs (Figure A.3) show almost same surface morphology of all films. From the above findings, we can conclude that the optimum temperature and duration parameters are 75 °C and 60 minutes, respectively. Hence, the third series III (chapter 3 in the main body of the manuscript) has been dedicated to study the effect of I_2 amount at fixed elaboration temperature 75 °C and duration 60 minutes. It is worth to mention that this series has been chosen to be presented in the main body of the manuscript due to its best electrical and optical related results compared to the other two series as shown from FOM (Figure A.4).

Table A.2: CuI prepared at different duration with fixed 0.1g I_2, 75 °C

Duration (minutes)	Carrier concentration (cm^{-3})	Mobility ($cm^2 V^{-1} s^{-1}$)	Conductivity ($S\ cm^{-1}$)
20	4.55E+18	26.3	19
30	6.42E+18	20.5	21
60	2.29E+18	44.7	16
150	7.31E+18	23.9	28

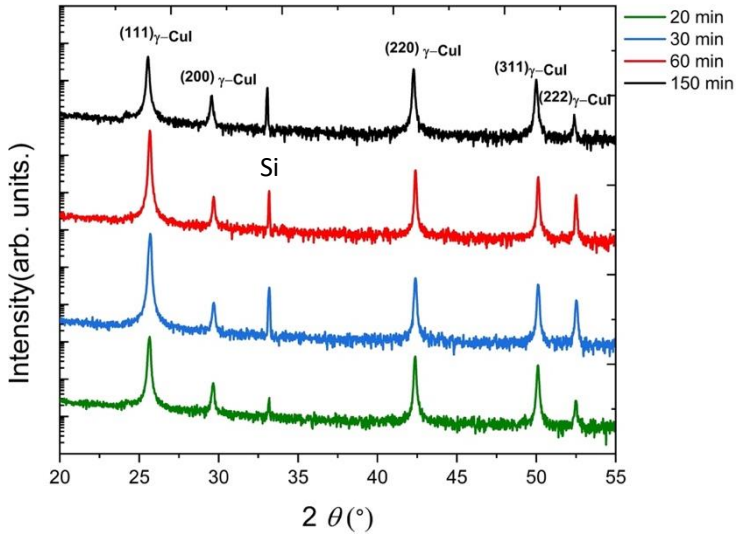

Figure A.1: Series of X -ray diffractograms of CuI films synthesized with different durations.

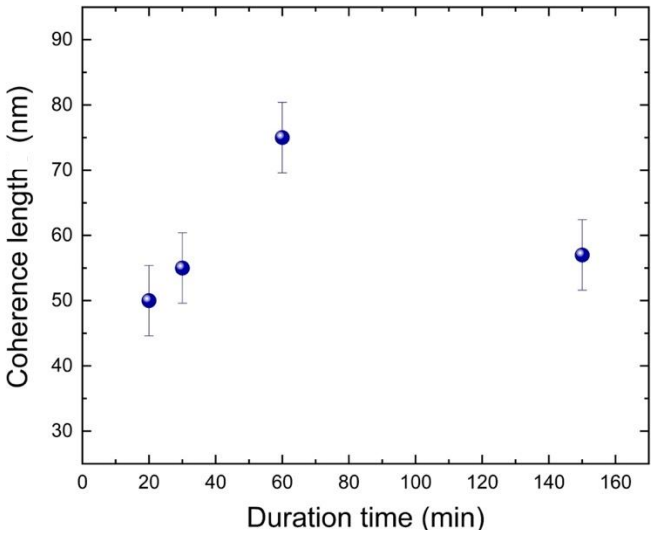

Figure A.2: Evolution of the coherence length of the γ-CuI films as a function of duration.

Table A.3: Lattice parameter and coherence length of the γ-CuI thin film prepared at different duration.

Duration (minutes)	Lattice parameter (nm)	Coherence length (nm)
20	0.605231	50
30	0.605295	55
60	0.604791	75
150	0.605670	57

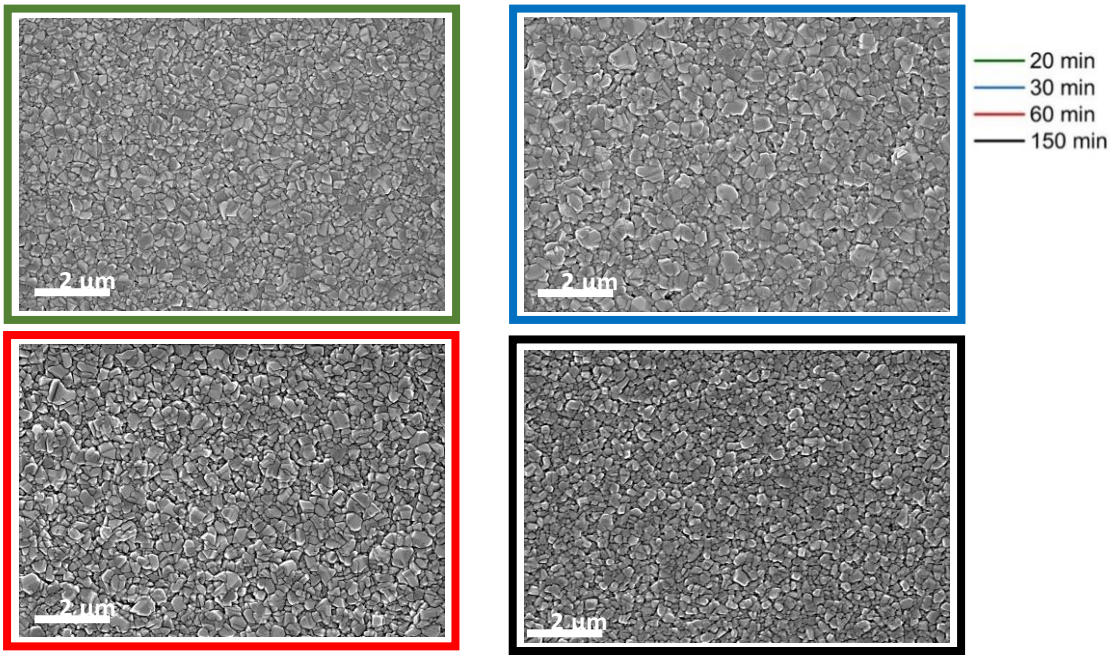

Figure A.3: Scanning electron microscopy (SEM) images of the γ-CuI thin film prepared at different duration.

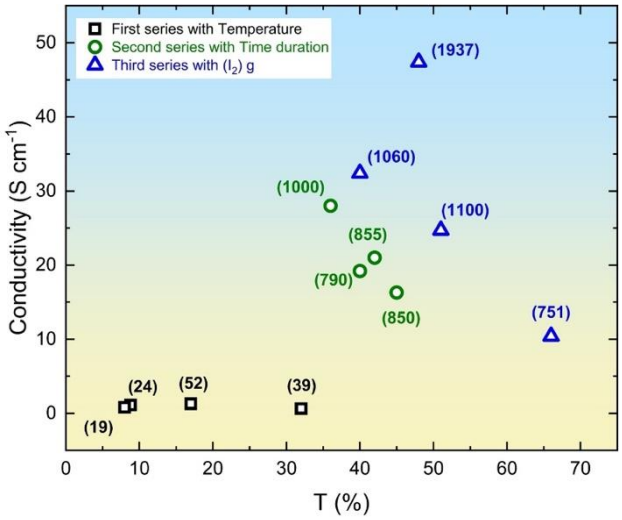

Figure A.4: Evolution of electrical conductivity and averaged visible transmittances and the figure of merit of γ-CuI films of three series.

Appendix B

Surface morphology of γ-CuI samples prepared at various I_2 amount (0.10 – 0.15 – 0.20 – 0.50 g), 60 minutes, 75 °C

The surface morphology of these samples have been studied by SEM (Figure B.1). The SEM micrographs exhibit, as estimated from ImageJ softwire, almost the same grain size (approx. 250 nm) for the samples prepared with 0.10, 0.15 and 0.20 g I_2.). Only the sample prepared with 0.50 g shows slightly higher grain size. In addition, the AFM analysis (Figure B.2) has been performed for all samples. The surface roughness increases with the I_2 amount, except for the sample prepared with 0.5 g I2 that shows a RMS value of 19 nm due to large and flat grains.

a) 0.10g of iodine with mean grain size 247 nm

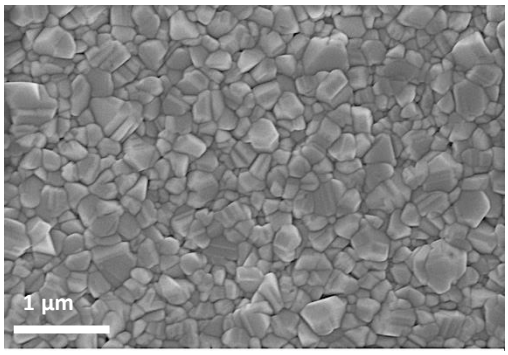

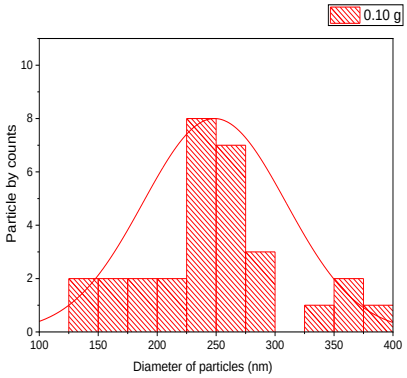

b) 0.15g of iodine with mean grain size 255 nm

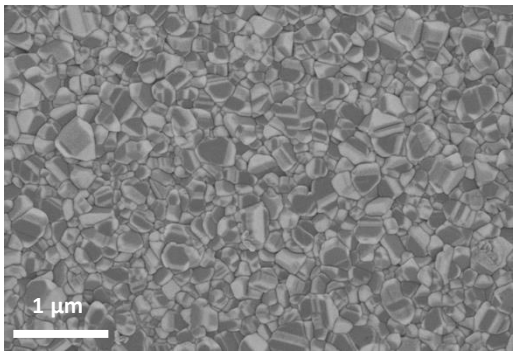

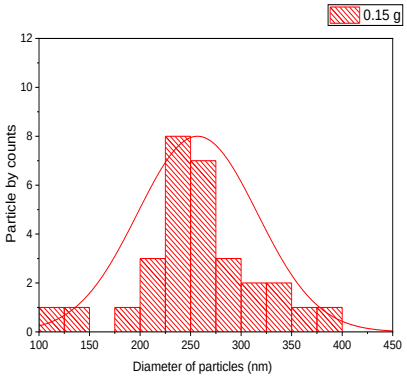

c) 0.20g of iodine with mean grain size 248 nm

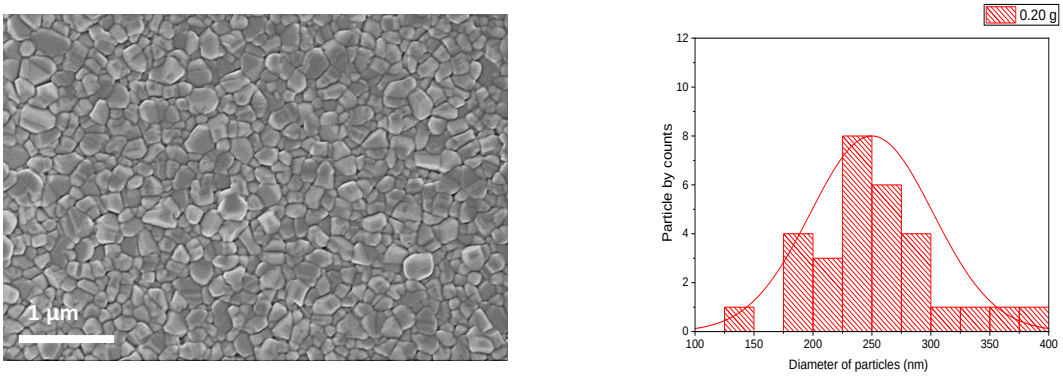

d) 0.50g of iodine with mean grain size 290 nm

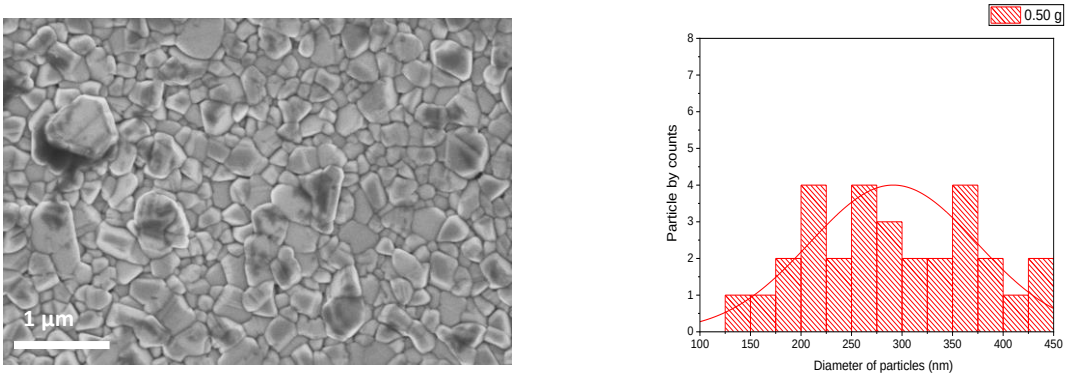

Figure B.1: Scanning electron microscopy (SEM) images and histograms of particle size distribution prepared with different amount of iodine. (a) 0.1g (b) 0.15g, (c) 0.2g and (d) 0.5g.

a) 0.10g of iodine with root mean square roughness 21 nm

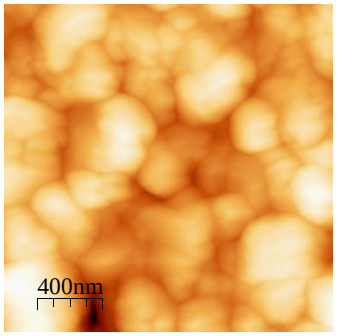

RMS Average = 21 nm

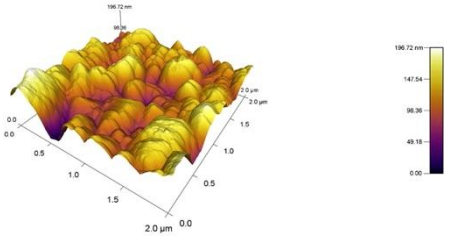

b) 0.15g of iodine with root mean square roughness 23 nm

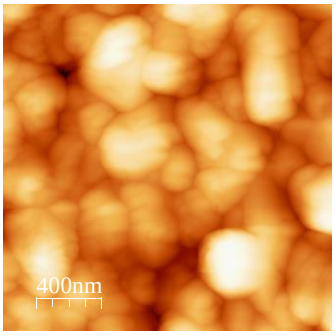

RMS Average = 23 nm

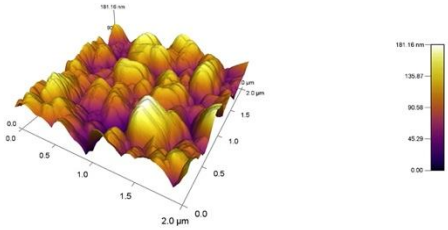

c) 0.20g of iodine with root mean square roughness 35 nm

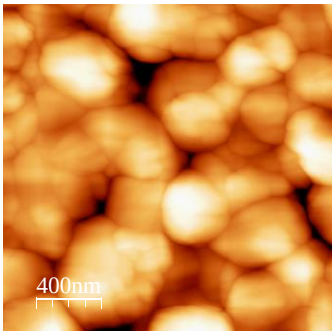

RMS Average = 35 nm

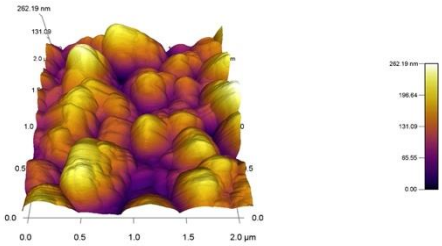

d) 0.50g of iodine with root mean square roughness 19 nm

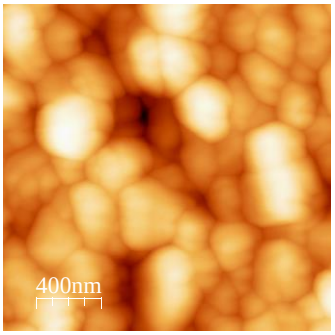

RMS Average = 19 nm

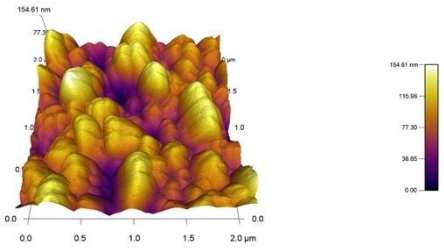

Figure B.2. AFM images(2μm×2μm) and root-mean-square roughness (RMS) values of γ-CuI films prepared with different amount of iodine.

Appendix C

Evidence of the high reactivity of Ag to I_2 compared to Cu

The surface morphology of silver iodide and copper iodide thin films is presented in Figure C1. The CuI films have been formed either at room temperature or at 75 °C (amount of I_2 = 0.10 g and iodination duration: 120 minutes). The surface morphology of CuI films is strongly dependent on the iodination temperature. At room temperature, the films exhibit large flat grains (mean grain size: 455 nm) with few observable twins (Figure C1a). On the other hand, the films obtained at 75 °C show facetted grains with a grain size close to 250 nm (Figure C1b). The increase of the iodination temperature induces an improvement of the crystalline quality of copper iodide films. The surface morphology of a silver iodide film synthesized at room temperature (iodination duration: 120 minutes and 0.10 g of I_2) is depicted in Figure C1c. AgI film exhibit facetted grains with a mean size of 556 nm. Twins are clearly evidenced on silver iodide grains. The morphology of AgI grains is very similar to that observed on CuI films formed at 75 °C, suggesting that the reactivity of silver with iodine is higher to that of copper. This is the reason why the deposition of AgI films has been chosen to be performed at RT.

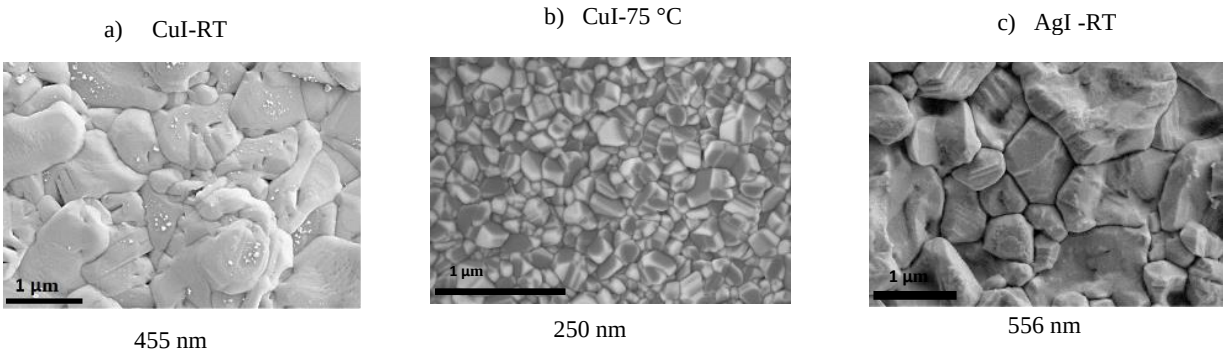

Figure C.1: Scanning electron microscopy (SEM) images prepared on Si. (a) CuI-RT (b) CuI-75 °C and (c) AgI-RT.

Appendix D

Elaboration of silver iodide films

Silver iodide (AgI) thin films have been prepared by deposition of silver metallic films using sputtering technique followed by iodination process at different amount of iodine (0.10, 0.15, 0.20 and 0.50 g), 10 minutes, 100 °C. Transparent film (Figure D.1) are obtained with bandgap value around 2.8 eV (Figure D.2). Whatever the amount of I_2, X-ray diffraction clearly evidence that the 70 nm thick silver film is fully transformed into AgI (no remaining silver metallic diffraction peak) and that the silver iodide crystallize into the wurtzite-like structure (β-AgI phase) (Figure D.3). A preferred orientation along the [101] direction is evidenced for AgI films. Using the Scherrer's formula the coherence length is approx. 64 nm.

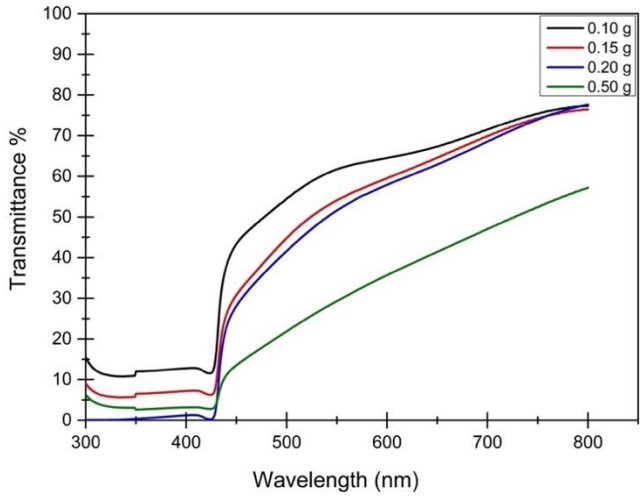

Figure D.1: Transmission spectra of the AgI thin films synthesized with different amounts of iodine and inset of Tauc plot of AgI film

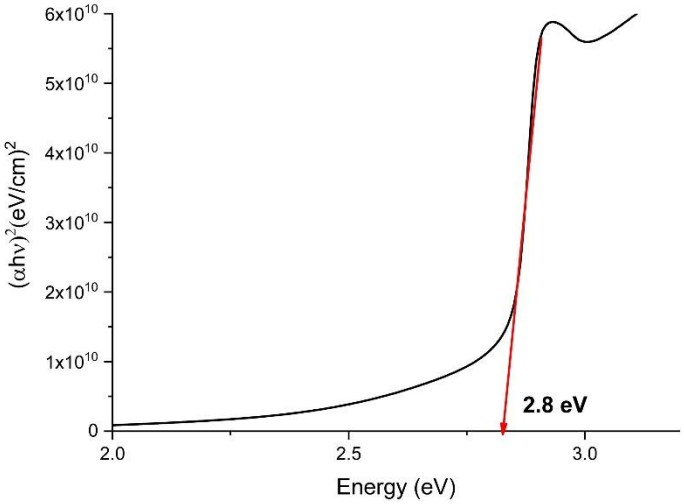

Figure D.2: Depiction of a typical Tauc's plot of AgI film for 0.10 g of I_2.

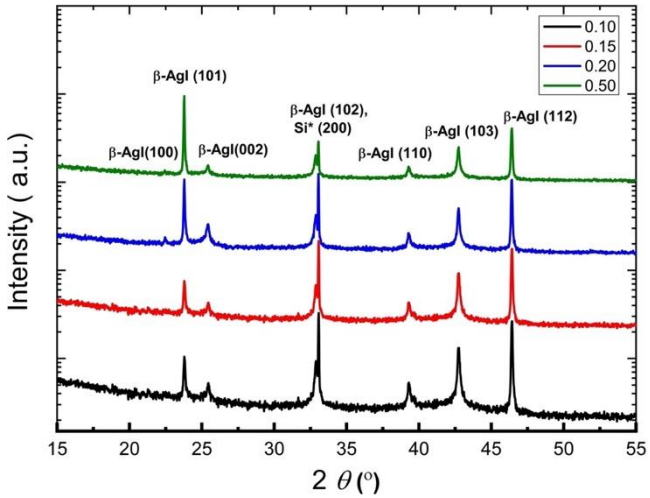

Figure D.3: Series of X -ray diffractograms of AgI films synthesized with different amounts of iodine.

Résumé

Les matériaux conducteurs transparents (MCT) suscitent un grand intérêt grâce à leurs excellentes propriétés optoélectroniques, qui s'adaptent à plusieurs applications de la vie quotidienne. Au cours des dernières années, les développements les plus spectaculaires concernent les dispositifs émetteurs de lumière et les cellules solaires utilisant ces matériaux combinant deux propriétés supposées antagonistes. Ainsi, de nombreuses études ont été consacrées soit à l'amélioration des performances des matériaux conducteurs transparents existants, soit à la découverte de nouvelles compositions.

La plupart des études sur le développement de la MCT ont été principalement axées sur les films minces d'oxydes métalliques, tels que le ZnO dopé à l'aluminium (AZO) et l'oxyde d'indium dopé à l'étain (ITO). La quasi-totalité des MCT employés industriellement actuellement sont des matériaux de type n, c'est-à-dire des semi-conducteurs pour lesquels le transport de charges est assuré par les électrons. En revanche, les MCT de type p (conduction par les trous) ne présentent pas de propriétés d'usage suffisamment élevées pour permettre leur application. De ce fait, la recherche sur les MCT avec des propriétés de type p est toujours en cours. Dans cette direction, l'iodure de cuivre (CuI) est l'un des candidats les plus prometteurs grâce à sa grande transparence et à sa conductivité intrinsèque de type p. Ceci permet l'utilisation du CuI dans différents domaines, tels que les applications photovoltaïques et optoélectroniques. Ce matériau présente un grand intérêt en tant qu'électrode transparente de type p dans les cellules solaires organiques et les thermogénérateurs flexibles transparents à micro-échelle [1,2].

Dans la famille des halogénures métalliques, l'iodure d'argent (AgI) présente des structures électroniques et de bande similaires à celles du CuI, mais avec une conductivité intrinsèque de

type n. Ceci encourage donc les approches de l'élaboration de diodes à hétérojonction p-n transparentes à partir de ces deux composés [3].

Sur la base des informations ci-dessus, un composé ternaire de (Ag,Cu)I mérite d'être exploré. Ainsi, Annadi et al. ont récemment rapporté les propriétés optiques et électroniques du système (Ag,Cu)I [4]. Ces auteurs ont montré que le type des porteurs de charge dans le composé ternaire peut être manipulé entre un type p et un type n en fonction du rapport atomique Ag/Cu. Néanmoins, la corrélation entre les résultats optiques, en particulier la photoluminescence (PL), et les résultats électriques n'a pas été établie clairement. Par conséquent, ce travail est dédié à l'étude approfondie de la microstructure des systèmes binaires et ternaires ci-dessus. De plus, nous nous concentrons sur le lien entre les réponses PL et électriques des films minces développés. Une corrélation claire entre le comportement électrique obtenu et la réponse de photoluminescence doit être établie. Le rôle des défauts ponctuels, les lacunes de Cu et les lacunes de I, dans les réponses électriques et PL sera discuté en détail. En outre, le passage du type de porteur de p à n sera interprété par le rôle de la chimie des défauts.

Ce manuscrit de thèse est organisé en quatre chapitres indépendants.

Le chapitre 1 est principalement consacré à une brève introduction sur les propriétés physiques et structurelles des halogénures de cuivre et d'argent et leurs applications. Leur structure cristalline, leur transition de phase, leur structure de bande, leurs propriétés optiques et électriques sont décrites. En outre, les méthodes de synthèse rapportées dans la littérature ont également été mises en évidence. La plupart des matériaux à base d'oxydes métalliques présentent une conductivité de type n efficace à température ambiante. C'est la raison pour laquelle la recherche et le développement de semi-conducteurs et de conducteurs transparents de type p sont intenses dans les secteurs universitaires et industriels. L'iodure de cuivre (CuI) est l'un des matériaux candidats

de type p les plus intéressants en raison de sa large gamme de conductivité, ce qui permet de l'utiliser dans des dispositifs optoélectroniques comme électrodes transparentes et couches semi-conductrices [5]. De plus, les films minces de CuI, avec une transparence optique élevée dans le domaine de la lumière visible, peuvent être obtenus en utilisant différents procédés de dépôt à basse température (entre la température ambiante et 75 °C) [1,6,7]. Ceci constitue un avantage supplémentaire du point de vue de l'élaboration. Ainsi, dans ce chapitre, nous donnons un aperçu des propriétés structurelles et physiques des halogénures de cuivre, en nous concentrant sur CuI, et nous les comparons aux semi-conducteurs à large bande interdite utilisés commercialement. Nous discutons de la structure électronique, des défauts ponctuels et du caractère du dopage dans les cristaux de CuI. De plus, nous présentons un résumé des développements récents des dispositifs à base de CuI avec des exemples de certaines applications. Enfin, nous faisons état des défis actuels et des perspectives potentielles. Ce chapitre donne également des informations sur la synthèse, la structure et les propriétés de l'iodure d'argent. Bien que ce matériau soit représenté comme un matériau de type n, il est utile de décrire ses propriétés. En effet, des hétérojonctions basées sur des bicouches CuI / AgI ont été décrites dans la littérature [3]. Enfin, la dernière section de ce chapitre est consacrée à l'élaboration et à la caractérisation de matériaux ternaires ((Ag,Cu)I). Bien qu'étudiés depuis plusieurs décennies, le ternaire (Ag,Cu)I sous forme de couches minces avait été très peu étudié avant le début de notre thèse.

Le chapitre 2 s'attache à décrire en détail les principales méthodes expérimentales utilisées pour caractériser les échantillons préparés. Les aspects techniques et fondamentaux de la pulvérisation magnétron et les techniques connexes de caractérisation des films minces sont présentés. Les grands principes de fonctionnement des microscopes électroniques à balayage et à transmission sont exposés. Les expériences d'effet Hall et de photoluminescence utilisées pour les

caractérisations électriques et optiques, respectivement, sont également discutées en détail. Une caractérisation holistique des films minces nécessite une compréhension détaillée de la composition, du degré de cristallisation, de l'épaisseur, de la morphologie, de l'adhésion et des propriétés physiques liées à leurs attributs mécaniques, magnétiques, optiques, électriques et autres [8,9]. Dans la présente thèse, l'iodure de cuivre et l'iodure de cuivre et d'argent ont été synthétisés par ioduration de respectivement des films minces de cuivre et des films de cuivre-argent préalablement déposés par pulvérisation magnétron. Ce chapitre décrit les méthodes utilisées pour synthétiser et caractériser les films d'iodure. La structure des films a été caractérisée par la diffraction des rayons X en configuration Bragg-Brentano (DRX). La morphologie et la microstructure des films a été étudiée par microscopie électronique à balayage (MEB) et microscopie électronique en transmission (MET). La composition des films a été mesurée à l'aide d'une microsonde de Castaing (EPMA) et de la spectroscopie de dispersion d'énergie des rayons X (EDS). Les propriétés optiques ont été caractérisées par spectrophotométrie UV-visible dans la gamme 250-800 nm. La photoluminescence (PL) a été utilisée pour évaluer le comportement optique du matériau étudié en fonction de la chimie des défauts. Les propriétés électriques ont été mesurées en utilisant l'effet Hall et la technique de la sonde à quatre pointes. La résistivité, la densité de porteurs et la mobilité ont été déduites des mesures de Hall à température ambiante et à basse température dans la géométrie de van der Pauw. Ce chapitre permet au lecteur de retrouver les conditions expérimentales d'élaboration et de caractérisation des films minces pour pouvoir, le cas échéant, répéter les travaux que nous avons menés.

Le chapitre 3 est consacré à la présentation et à la discussion des résultats obtenus sur des films minces de CuI. Ces films ont été préparés par ioduration de films minces de cuivre déposés au préalable par pulvérisation magnétron sur des substrats en verre et en silicium. L'effet du rapport

stœchiométrique entre Cu et I sur la phase cristalline et la structure du film a été étudié. Les détails de la microstructure locale sont étudiés par microscopie électronique à transmission à haute résolution (HR-TEM). En outre, les propriétés électriques et optiques des films minces préparés à différentes quantités d'iode sont discutées en détail. D'autres paramètres d'ioduration comme la durée du traitement ou la température de synthèse ont également été étudiés. Les principaux résultats obtenus en faisant varier ces paramètres sont rassemblés dans plusieurs annexes que le lecteur pourra trouver à la fin du manuscrit. La phase cristalline et la morphologie de surface des films d'iodure de cuivre ont été étudiées respectivement par diffraction des rayons X (DRX) et par microscopie électronique à balayage (MEB). Quelle que soit la quantité d'iode ajoutée, les films de CuI préparés cristallisent dans une structure de type blende (phase γ) et présentent une orientation préférentielle le long de la direction [111]. De plus, une étude détaillée de la microstructure par microscopie électronique en transmission à haute résolution (HR-TEM) a révélé la présence et les détails de défauts d'empilement (mâcles). Par rapport à la littérature, il est important de relever ici qu'une telle étude par microscopie électronique en transmission n'avait pas encore été réalisée. Elle a pu se dérouler dans le cadre de notre thèse par l'utilisation d'un porte-échantillon refroidi à l'azote liquide. Les propriétés électriques des films de CuI ont été caractérisées par des mesures à effet Hall et ont révélé un comportement de type p pour tous les films. Le comportement électrique a été discuté et attribué à la modification des défauts ponctuels intrinsèques. En outre, la bande interdite électronique et les propriétés de luminescence ont été étudiées par spectroscopie UV-visible et par photoluminescence. Les films de CuI ont montré une large bande interdite (environ 3,05 eV) avec une transmittance moyenne d'environ (66 %) dans la région visible. De plus, la PL a montré une émission bleue allant de 400 à 440 nm provenant de la recombinaison excitonique et des défauts ponctuels radiatifs. Enfin, un comparaison entre les

performances de nos films et celles des travaux précédemment publiés a été réalisée. Les résultats présentés dans ce chapitre ont été publiés dans la référence suivante : O. Madkhali et al., Blue emission and twin structure of p-type copper iodide thin films, Surfaces and Interfaces 27 (2021) 101500.

Le chapitre 4 se concentre sur les premiers résultats des films minces (Ag,Cu)I préparés par ioduration de couches Ag-Cu co-pulvérisées. La structure cristalline des films préparés a été étudiée par diffraction des rayons X (DRX). Les propriétés électriques des films d'(Ag,Cu)I ont été caractérisées par des mesures d'effet Hall et ont révélé un comportement de porteur de type p ou de type n en fonction de la composition chimique en argent. Une corrélation entre les résultats optiques et électriques a été établie et a mis en évidence l'origine du comportement électrique. La structure cristalline des films préparés a été étudiée par diffraction des rayons X. Dans l'intervalle de compositions chimiques étudiées (environ 50 at. % d'argent), les films cristallisent tous dans la structure cubique caractéristique de l'iodure de cuivre, démontrant ici la solubilisation de l'argent dans la maille cristallographique de CuI. La morphologie des films a été étudiée par microscopie électronique à balayage. Les propriétés électriques des films (Ag,Cu)I ont été caractérisées par des mesures d'effet Hall. Selon la teneur en argent, les films présentent un comportement de type p ou de Le comportement électrique a été discuté et attribué à la modification des défauts ponctuels intrinsèques. Les propriétés optiques ont été examinées par spectroscopie UV-visible et par photoluminescence. Il a été constaté que la cristallinité et la morphologie du film ont été modifiées en raison du changement de la concentration en Ag AgxCu1-xI ($0 \leq x \leq 0,52$). En outre, les résultats PL ont montré une tendance des caractéristiques spectrales du CuI à être modifiées vers celles de l'AgI avec l'augmentation de la teneur en argent. Une corrélation entre les résultats optiques et électriques a été établie et a mis en évidence l'origine du comportement électrique. Il est proposé

que la présence d'Ag dans les films minces (Ag,Cu)I favorise la formation de lacunes d'iode, qui agissent comme des défauts de type donneur, et finalement, avec l'augmentation de la teneur en Ag, le passage des porteurs de type p à type n se produit. L'interaction de ce défaut donneur avec le défaut accepteur intrinsèque, représenté par les lacunes de Cu, régit les propriétés fonctionnelles, en particulier optiques et électriques, du matériau. Ces résultats peuvent ouvrir la voie au développement de dispositifs contrôlés à base de (Ag,Cu)I.

Les principaux résultats de la thèse sont résumés avec la conclusion générale et des perspectives d'études futures sont donnés en fin de manuscrit

Références

[1] C. Yang, M. Kneiβ, M. Lorenz, M. Grundmann, Room-temperature synthesized copper iodide thin film as degenerate p-type transparent conductor with a boosted figure of merit, Proc. Natl. Acad. Sci. U. S. A. 113 (2016) 12929–12933. https://doi.org/10.1073/pnas.1613643113 .

[2] C. Yang, D. Souchay, M. Kneiß, M. Bogner, H.M. Wei, M. Lorenz, O. Oeckler, G. Benstetter, Y.Q. Fu, M. Grundmann, Transparent flexible thermoelectric material based on non-toxic earth-abundant p-type copper iodide thin film, Nat. Commun. 8 (2017). https://doi.org/10.1038/ncomms16076.

[3] J.-H. Cha, D.-Y. Jung, Air-Stable Transparent Silver Iodide–Copper Iodide Heterojunction Diode, ACS Appl. Mater. Interfaces. 9 (2017) 43807–43813. https://doi.org/10.1021/acsami.7b14378.

[4] A. Annadi, H. Gong, Success in both p-type and n-type of a novel transparent AgCuI alloy semiconductor system for homojunction devices, Appl. Mater. Today. 20 (2020) 100703. https://doi.org/10.1016/j.apmt.2020.100703.

[5] A. Liu, H. Zhu, M. Kim, J. Kim, Y. Noh, Engineering Copper Iodide (CuI) for Multifunctional p-Type Transparent Semiconductors and Conductors, Adv. Sci. (2021) 2100546. https://doi.org/10.1002/advs.202100546.

[6] N. Yamada, R. Ino, Y. Ninomiya, Truly Transparent p-Type γ-CuI Thin Films with High Hole Mobility, Chem. Mater. 28 (2016) 4971–4981. https://doi.org/10.1021/acs.chemmater.6b01358.

[7] P. Storm, M.S. Bar, G. Benndorf, S. Selle, C. Yang, H. von Wenckstern, M. Grundmann, M. Lorenz, High mobility, highly transparent, smooth, p-type CuI thin films grown by pulsed laser deposition, APL Mater. 8 (2020) 091115. https://doi.org/10.1063/5.0021781.

[8] H. Bubert, H. Jenett, eds., Surface and Thin Film Analysis: Principles, Instrumentation, Applications, 1st ed., Wiley, 2002. https://doi.org/10.1002/3527600167.

[9] J. Poortmans, V. Arkhipov, eds., Thin Film Solar Cells: Fabrication, Characterization and Applications, John Wiley & Sons, Ltd, Chichester, UK, 2006. https://doi.org/10.1002/0470091282.

Abstract

In this thesis, we study the formation of copper iodide (CuI) and silver copper iodide (Ag,Cu)I thin films from a two-step procedure: deposition of a metallic film by magnetron sputtering and iodination in iodine vapor. Numerous techniques have been used to determine the films properties such as: X-ray diffraction, transmission electron microscopy, Hall effect, UV-visible spectroscopy… For CuI films, we obtained transparent p-type semiconductors films crystallizing in the γ-phase with wide bandgap (Eg ≈ 3.05 eV). Copper iodide films grow with a strong preferred orientation along the [111] direction. SEM analysis of thin film morphology demonstrates that iodination conditions can affect crystal size. Transmission electron microscopy (TEM) and selected area electron diffraction (SAED) have revealed crystallographic twin domains in CuI crystals, revealing their geometry and orientation. The films are highly conductive, optically transparent and exhibit high value of figure of merit.

The properties of (Ag,Cu)I thin films have been studied using the same methods as a function of the silver content. (Ag,Cu)I films can be either p-type or n-type, depending on Ag concentration. Nevertheless, no structural change has been evidenced by XRD. The optical band gap can be monitor by the progressive addition of silver. The same is true for the electrical activation energy. In addition, the PL results showed a tendency of the PL spectral features of CuI to be changed to those of AgI with the increase of the silver content. A correlation between the optical and electrical results was established and evidenced the origin of the electrical behaviour. It is proposed that presence of Ag in (Ag,Cu)I thin films promotes the formation of the I-vacancies, which act as donor type defect, and eventually, with increasing the Ag content, crossover the carriers from p-type to n-type occurs.

Keywords: Copper iodide, Silver copper iodide, Semiconductor, Sputtering, Optoelectronic applications.

Résumé

Dans cette thèse, nous avons étudié la formation de couches minces d'iodure de cuivre (CuI) et d'iodure de cuivre argent (Ag,Cu)I à partir d'une procédure en deux étapes : dépôt d'un film métallique par pulvérisation magnétron et ioduration dans de la vapeur d'iode. De nombreuses techniques ont été utilisées pour déterminer les propriétés des films telles que : diffraction des rayons X, microscopie électronique à transmission, effet Hall, spectroscopie UV-visible… Pour les films CuI, nous avons obtenu des films semi-conducteurs transparents de type p cristallisant dans une structure type γ-CuI avec une large bande interdite (≈ 3,05 eV). Les films d'iodure de cuivre croissent avec une forte orientation préférentielle le long de la direction [111]. La microscopie électronique à transmission (MET) et la diffraction électronique à zone sélectionnée (SAED) ont révélé des mâcles dans les cristaux CuI, révélant leur géométrie et leur orientation. Les films sont hautement conducteurs, optiquement transparents et présentent une valeur élevée de facteur de mérite.

Les propriétés des couches minces (Ag,Cu)I ont été étudiées selon les mêmes méthodes en fonction de la teneur en argent. Ces films peuvent être de type p ou de type n, en fonction de la concentration en Ag. Néanmoins, aucun changement structural n'a été mis en évidence par XRD. La morphologie de la surface du film dépend également fortement de la teneur en argent. Le gap optique peut être contrôlé par l'ajout progressif d'argent. Il en est de même pour l'énergie d'activation des phénomènes de conduction électrique. La photoluminescence a montré l'évolution entre les films pauvres en argent et les riches. Une corrélation entre les résultats optiques et électriques a été établie et a mis en évidence l'origine du comportement électrique. Il est proposé que la présence d'Ag dans les films minces (Ag,Cu)I favorise la formation des lacunes d'iode, qui agissent comme un défaut de type donneur, et qui éventuellement, conduisent à la changement de la nature des porteurs.

Mots-clés : Iodure de cuivre, Iodure de cuivre argenté, Semiconducteur, Pulvérisation, Applications optoélectroniques.